Technical Letter Report on the Cracking of Irradiated Stainless Steels in Low-Corrosion-Potential Environments

Nuclear Engineering Division

About Argonne National Laboratory
Argonne is a U.S. Department of Energy laboratory managed by UChicago Argonne, LLC under contract DE-AC02-06CH11357. The Laboratory's main facility is outside Chicago, at 9700 South Cass Avenue, Argonne, Illinois 60439. For information about Argonne, see http://www.anl.gov.

Technical Letter Report on the Cracking of Irradiated Stainless Steels in Low-Corrosion-Potential Environments

Manuscript Completed: May 2013

Y. Chen, B. Alexandreanu, and K. Natesan

Argonne National Laboratory, Argonne, IL 60439

A. S. Rao, Project Manager, U.S. Nuclear Regulatory Commission

This page is intentionally left blank.

Abstract

Irradiation-assisted stress corrosion cracking (IASCC) is a major degradation mechanism for reactor internal components of austenitic stainless steels (SSs) in light water reactors. Crack growth rate (CGR) and fracture toughness J-R curve tests were performed on four irradiated SS specimens in high-purity water with low dissolved oxygen and in a simulated pressurized water reactor (PWR) environment. The samples had been previously irradiated from ~5 to 8 dpa in the BOR-60 reactor. The materials were cold-worked (CW) 316 and solution-annealed (SA) 304L SSs, which are commonly used in PWR core internals. Cyclic and constant-load CGRs were obtained from these samples to assess their cracking behaviors in low-corrosion-potential environments. A Ti-stabilized specimen, CW 316-Ti SS, was found to be highly vulnerable to IASCC, and its cracking susceptibility increased with neutron dose between ~5 and 8 dpa. The CW 316 and SA 304L SSs showed moderate cracking susceptibilities in the low-corrosion-potential environments up to ~7 dpa. Periodic partial unloading (PPU) had a significant impact on the crack growth behavior of all irradiated specimens, and the measured CGRs were more than one order of magnitude higher in the test periods with than without PPU. A "stair-step" crack growth behavior was also observed for all irradiated specimens during the test periods with PPU, suggesting a strong effect of dynamic loading on IASCC. The SA 304L SS showed the best fracture resistance, and the CW 316 SS was the most brittle among the tested specimens. The fracture toughness J values of the two CW 316-Ti SS specimens were nearly identical at ~5 and ~8 dpa.

This page is intentionally left blank.

Contents

This page is intentionally left blank.

Figures

Tables

This page is intentionally left blank.

Executive Summary

Crack growth rate (CGR) and fracture toughness J-R curve tests were performed on irradiated stainless steels in either high-purity water with low dissolved oxygen (DO) or a simulated pressurized water reactor (PWR) environment. The specimens were cold-worked (CW) Type 316 and solution-annealed (SA) Type 304L stainless steels (SSs) commonly used in PWR core internals. The samples were disk-shaped compact tension (DCT) specimens with a nominal thickness of 8 mm and were irradiated to ~5-8 dpa in the BOR-60 reactor. The two ~5-dpa specimens (CW 316 SS and CW 316-Ti SS) were tested in low-DO high-purity water, and the ~7-dpa (SA 304L SS) and ~8-dpa (CW 316-Ti) specimens were tested in a simulated PWR environment. The corrosion potentials of SSs in both environments are similar enough to ensure a comparable CGR response. All specimens were pre-cracked in the test environments at 320°C. Cyclic and constant-load CGRs were measured for these samples to evaluate their susceptibilities to irradiation-assisted stress corrosion cracking (IASCC) under PWR-relevant conditions. The constant-load CGR tests were conducted with and without periodic partial unloading (PPU) to assess the effect of dynamic loading on cracking. The temperature dependence of CGR was also evaluated in three of the four tests. After the CGR tests, fracture toughness J-R curve tests were carried out at 320°C on the same specimens in the test environments. All fracture surfaces of the tested samples were examined with a scanning electron microscope, and fracture morphologies were identified for the different stages of the tests.

In the cyclic CGR tests, environmentally enhanced cracking was readily induced in the irradiated specimens despite the low-corrosion-potential environments. The two ~5-dpa specimens exhibited much lower growth rates than the ~7- and 8-dpa specimens. For all specimens, transgranular (TG) cracking was the dominant fracture mode in the cyclic CGR test regions. Small crystalline facets and, sometimes, intergranular (IG) morphology were also seen in the SA 304L sample. The high cracking susceptibility revealed in the cyclic CGR tests is consistent with that observed in the subsequent constant-load CGR tests with stress corrosion cracking (SCC).

In the SCC CGR tests, PPU had a significant effect on the measured CGRs for all irradiated specimens. The CGR obtained with PPU can be more than one order of magnitude higher than that without PPU. Also, a "stair-step" crack growth behavior was often observed under load transients (e.g., PPU or rising stress intensity factor), suggesting a strong dynamic loading effect on IASCC in low-corrosion-potential environments. The stress intensity factor K dependence of CGR was also found to be higher with PPU. The high sensitivity to PPU suggests a combined effect of SCC and low-cycle fatigue on the cracking response of irradiated SSs.

Extensive IG cracking was observed for all specimens tested in this study. Among them, CW 316-Ti SS was the most susceptible heat, and the CW 316 SS showed a good resistance to IASCC. The different cracking susceptibility between the CW 316 and CW 316-Ti suggests a detrimental effect of Ti for IASCC in the low-corrosion-potential environments. At low stress intensity factors, the SCC CGR increased with dose between ~5 and 8 dpa for the CW 316-Ti SS. Above ~30 MPa m$^{1/2}$, the effect of dose became smaller. An increasing trend of CGR with dose up to 25 dpa was also seen with the other materials tested. While the SCC CGR of CW 316 SSs showed a monotonic increase with temperature, a peak CGR was observed for the SA 304L

SS around 290°C. This observation suggests two competing cracking mechanisms with opposite temperature dependences during crack growth.

Along with the previous J-R curve test results at lower doses, a decreasing trend of fracture toughness can be seen with increasing dose. Between ~5 and 8 dpa, the obtained J values were below 100 kJ/m^2. Among the four samples tested in this study, the SA 304L SS showed the best fracture resistance, and the CW 316 SS was the most brittle. The J values for the two CW 316-Ti SS specimens were nearly identical at ~5 and ~8 dpa. Additional tests at higher doses are required for adequately assessing neutron embrittlement of SSs in PWR-relevant conditions.

Acknowledgments

This page is intentionally left blank.

Acronyms and Abbreviations

BWR	Boiling Water Reactor
CF	Corrosion Fatigue
CGR	Crack Growth Rate
CIR	Cooperative IASCC Research
CW	Cold Worked
DCPD	Direct Current Potential Drop
DCT	Disk-shaped Compact Tension
DO	Dissolved Oxygen
ECP	Electrochemical Potential
HWC	Hydrogen Water Chemistry
IASCC	Irradiation-Assisted Stress Corrosion Cracking
IG	Intergranular
LVDT	Linear Voltage Displacement Transducer
LWR	Light Water Reactor
NWC	Normal Water Chemistry
PWR	Pressurized Water Reactor
PPU	Periodic Partial Unloading
RIAR	Research Institute of Atomic Reactors
SA	Solution Annealed
SCC	Stress Corrosion Cracking
SEM	Scanning Electron Microscopy
SS	Stainless Steel
TG	Transgranular

Units of Measure

cm	centimeter(s)
dpa	displacement(s) per atom
hr	hour(s)
kV	kilovolt(s)
MeV	million electron volts
min	minute(s)
ml	milliliter
mm	millimeter
MPa	megapascal(s)
ppb	parts per billion
ppm	parts per million
psig	pounds per square inch gauge
s	second(s)
μ	micron

1   INTRODUCTION

Irradiation-assisted stress corrosion cracking (IASCC) has been recognized as a major degradation mechanism for internal components of austenitic stainless steels (SSs) in light water reactors (LWRs).[1,2] While stress corrosion cracking (SCC) is a common issue for SSs exposed to high-temperature water, a harsh neutron irradiation environment can elevate the cracking susceptibility of SSs even further at the core region of a LWR. It is well understood that the occurrence of SCC requires three basic elements: susceptible material microstructure, aggressive environments, and tensile stress. Neutron bombardments can affect all of these elements and thus exert a negative impact on the cracking behavior of reactor internal materials. After a prolonged exposure to neutron irradiation, non-sensitized SSs become increasingly vulnerable to SCC in high-temperature aqueous environments. Service failures of fuel cladding, internal structures, and fasteners have been discovered in both boiling water reactors (BWRs) and pressurized water reactors (PWRs).[3-7] Since repair or replacement of structural components at the reactor core regions is extremely difficult and expensive, failures of major internal components could seriously impair the safe and economic operation of LWRs. As nuclear power plants age and accumulated neutron fluence increases in recent years, IASCC has become a progressively more important issue for license renewal and aging management worldwide.

Irradiation-induced microstructural and microchemical changes are believed to be the root cause of the elevated cracking susceptibility.[8-11] Under the bombardment of energetic neutrons, a large number of lattice atoms are unlocked from their original sites, generating vacancies and self-interstitials in crystalline materials. While most of the vacancies and interstitials quickly recombine after an initial collision phase, the remaining point defects evolve subsequently into metastable irradiation defects, giving rise to various irradiation effects, such as hardening, embrittlement, enhanced diffusion and segregation, void swelling, creep, etc. While the fundamental mechanism of IASCC remains unclear at present, several irradiation effects are thought to closely relate to the deteriorated cracking resistance of SSs. Chromium depletion at grain boundaries resulting from radiation-induced segregation is a possible mechanism to explain the increased susceptibility to intergranular SCC in SSs.[7,9,10] A highly localized plastic flow caused by small irradiation defects is also considered a critical factor of reduced cracking resistance after irradiation.[11,12] Without doubt, irradiation damage plays a key role in elevating the cracking susceptibility of non-sensitized SSs that would otherwise show excellent SCC performance in high-temperature water.

As a special form of SCC, IASCC is believed to possess a similar dependence on environmental variables as SCC. For unirradiated SSs, the SCC performance depends strongly on electrochemical corrosion potential (ECP). Crack growth rate (CGR) in a low dissolved oxygen (DO) environment is found to be significantly lower than that in a high-DO environment.[7] A low ECP environment, such as BWR hydrogen water chemistry (HWC) or PWR primary water chemistry, is beneficial for SCC resistance and has been demonstrated to be an effective way to mitigate the SCC degradation.[13,14] For irradiated SSs, a similar correlation between the CGR and ECP has also been observed.[15-17] While the cracking behavior of irradiated SSs in BWR normal water chemistry (NWC) has been investigated in several programs in recent years, a systematic analysis of the cracking of irradiated materials in the low corrosion potential regime is

1

still lacking. The CGR database of irradiated SSs is limited for BWR HWC or PWR environments at present. While in most cases HWC has a beneficial effect, several studies have found that the crack propagation behavior fails to respond to a decline in corrosion potential in some high-dose SS specimens.[18-20] These observations suggest that the mitigation of HWC may only be effective within a certain dose range. Even in cases where the mitigation effect of HWC is observed, the impact of neutron irradiation on the dependence of CGR on corrosion potential is not well understood. A better understanding of the interactions between environmental and irradiation variables is critically needed to characterize the crack growth behavior of irradiated SSs in low-corrosion-potential environments, such as a PWR primary environment.

In this study, four CGR tests were performed on irradiated disk-shaped compact tension (DCT) specimens in a low-DO high-purity water environment or in a simulated PWR primary water environment. The corrosion potentials of SSs in both environments are similar enough to ensure a comparable SCC crack growth response. Crack growth rates were measured under cyclic and constant-load conditions to evaluate their corrosion fatigue and SCC performance. After the CGR test, a fracture toughness J-R curve test was carried out on the same sample in the test environment to evaluate irradiation embrittlement. The test results were used to assess the corrosion fatigue and SCC performance of the irradiated SSs in low-corrosion-potential environments.

2   EXPERIMENTAL

2.1 Specimens and Irradiation

Four DCT specimens obtained from the Cooperative IASCC Research (CIR) program[21] were included in the current study. A schematic of the DCT sample is shown in Fig. 1. A side groove with a depth of about 5% of the sample thickness and a radius of 0.45 mm was machined on each side of all specimens after irradiation. One of the specimens is solution-annealed (SA) Type 304 L SS, which is commonly used for baffle plates in PWRs, and the other three samples are cold-worked (CW) Types 316 and 316-Ti SSs for baffle bolts. The chemical compositions of these materials are given in Table 1.
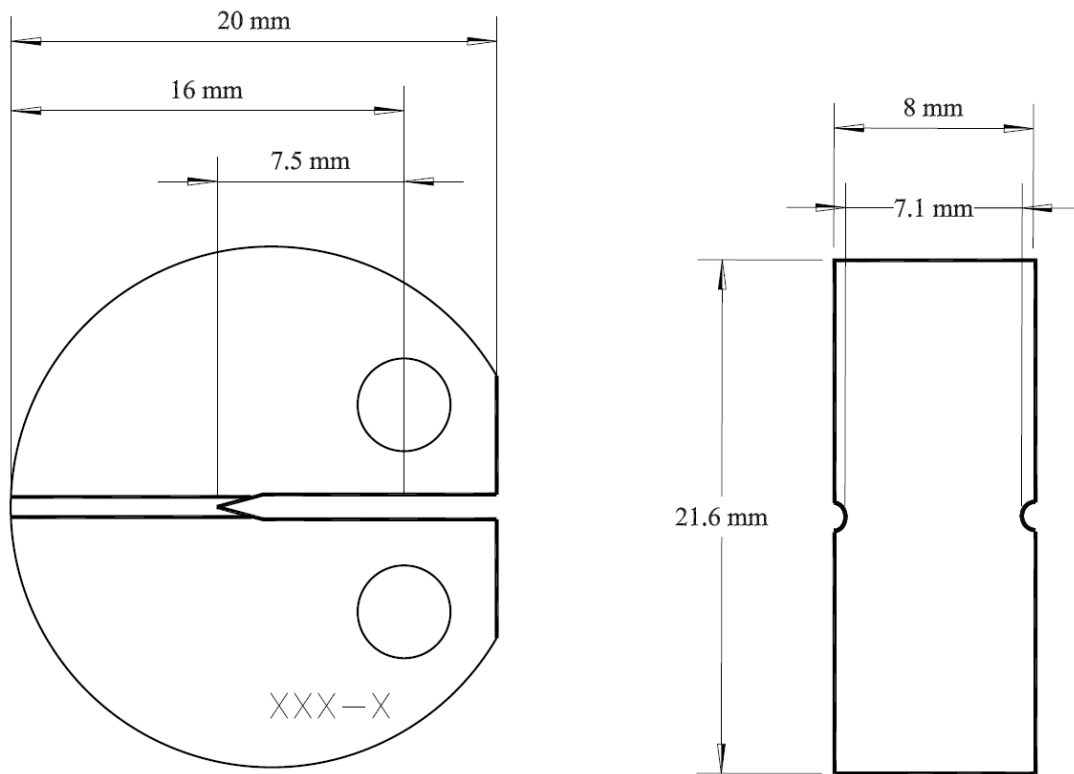
Figure 1. Schematic of disk-shaped compact tension specimen used in this study.

Table 1. Chemical compositions of the cast stainless steels examined in this study.[21]

Materials	Heat ID	Composition, wt. %													
		C	Mn	Si	P	S	Cr	Ni	Mo	N	Nb	Ti	O	Co	Cu
CW 316	BR	0.056	1.13	0.73	0.022	0.022	16.84	10.54	2.25	0.021	0.008	0.01	0.009	0.12	0.25
CW 316-Ti	CR	0.070	1.40	0.56	0.013	0.007	16.77	12.78	2.18	0.008	<0.01	0.38	0.004	0.10	0.06
SA 304L	SW	0.022	1.07	0.24	0.015	<0.002	18.42	10.45	-	0.025	-	-	-	-	-

The specimens were irradiated in the BOR-60 reactor, an experimental fast breeder reactor operated by the Research Institute of Atomic Reactors (RIAR) at Dimitrovgrad in Ulyanovsk Oblast, Russia. Two irradiation experiments, Boris-6 and -7, were carried out between 2001 and 2004 on these samples.[21] Neutron fluence was monitored by five dosimeters loaded into the central channel of the irradiation rig and in baskets with the specimens. Post-irradiation analyses of these dosimeter showed that the SA 304L SS and CW 316 SS specimens accumulated doses of 6.9 and 4.8 displacements per atom (dpa), respectively, whereas the two CW 316-Ti SS specimens were at 4.8 and 7.8 dpa. During irradiation, the irradiation temperature was controlled by the sodium coolant inlet and outlet, which were kept at 315°C and 325°C, respectively. Post-irradiation tensile tests were also carried out on the tensile specimens irradiated to the same doses.[21] These tests were performed at 330°C in an air atmosphere, and the results are shown in Table 2. Note that no tensile test was performed at 7.8 dpa for the CW 316-Ti SS (CR). The estimated values were interpolated from tensile testing results obtained from the same material irradiated to 4.8- and 10.7-dpa. The irradiated DCT specimens were discharged from the reactor at different times between 2003 and 2004, and were first cleaned of residual sodium and then transferred to Argonne National Laboratory via Studsvik.

Table 2. Yield and tensile strengths of the materials included in this study.[21]

Materials	Heat ID	Dose, dpa	Test Temp., °C	Yield Stress, MPa	Tensile Strength, MPa
CW 316	BR	0	330	487	609
		4.8	330	860	884
CW 316-Ti	CR	0	330	741	768
		4.8	330	948	962
		7.8	330	(988)[1]	(1007)[1]
SA 304L	SW	0	-	-	-
		6.9	330	623	631

[1] The estimated values were interpolated from tests conducted on the same material irradiated to 4.8- and 10.7-dpa.

2.2 Test Facilities

Two servo-hydraulic mechanical test systems located in the Irradiated Materials Laboratory (IML) at Argonne National Laboratory were used in this study. Each system is equipped with its own loading frame, autoclave, load cell, linear voltage displacement transducer (LVDT), Instron control console, and data acquisition system. Figure 2 is a schematic of the loading frame. The hydraulic actuator is located on top of the load frame, with other load train components suspended beneath it. The load cell is mounted on the top of the pull rod, and the sample is installed inside the load cage within the furnace. The sample is electronically insulated from the load cage with oxidized Zircaloy pins.

The tests were performed in either simulated PWR water or high-purity water with low DO (BWR HWC). These environments were provided by two water recirculation loops as shown in Fig. 3. Each loop consists of a storage tank, a high pressure pump, a regenerative heat

exchanger, an autoclave, an electrochemical potential (ECP) cell, a back-pressure regulator, two ion-exchange cartridges, and several heaters. The autoclaves are one-liter Type 316 stainless steel autoclaves and rated to 2900 psig for 350°C. During tests, water was circulated at a rate of 20-30 mL/min through the autoclaves. The temperature and pressure of the autoclaves were kept at ~320°C and ~1800 psig, respectively. For the PWR water environment, approximately 1000 ppm boron and 2 ppm lithium were added in the recirculation system, and pure hydrogen was used as cover gas. For BWR HWC, high-purity water was used with a cover gas of 4 % hydrogen balanced with nitrogen.
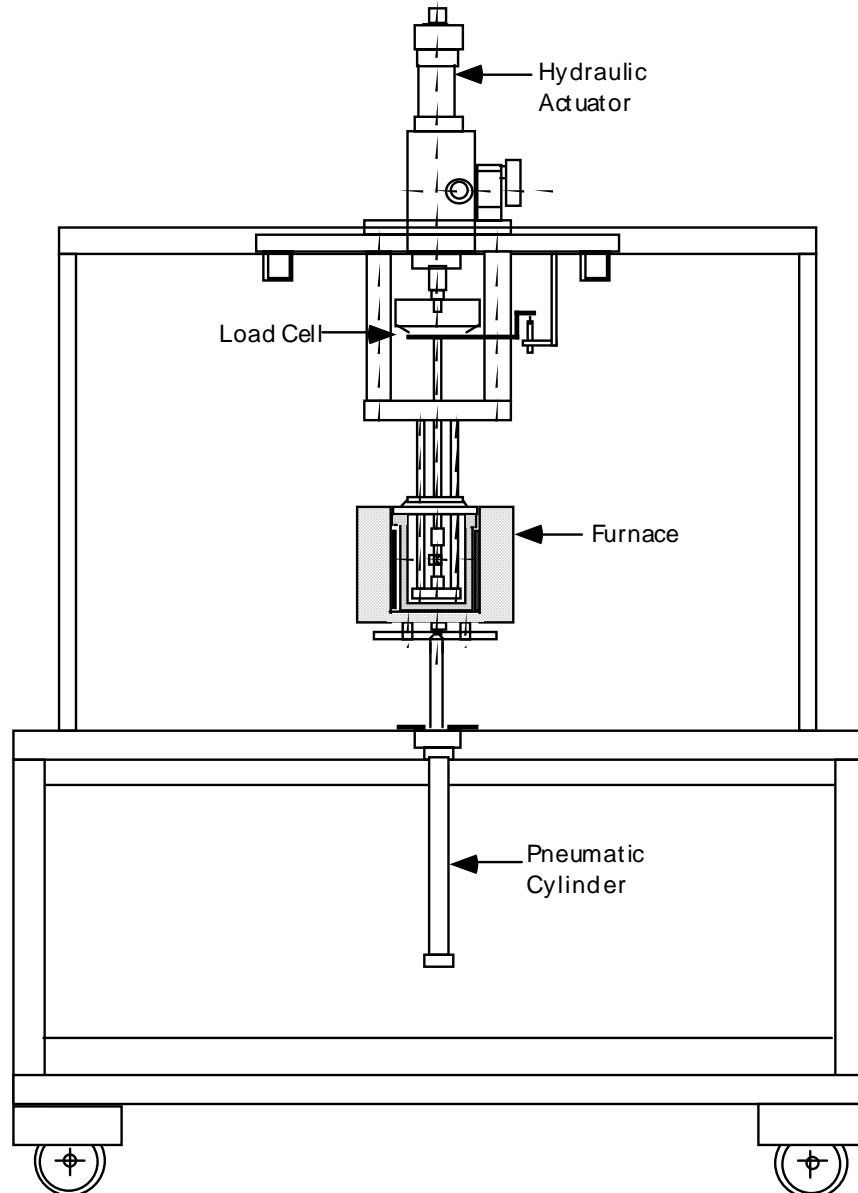
Figure 2. Mechanical test system for conducting CGR and J-R tests on radioactive specimens.
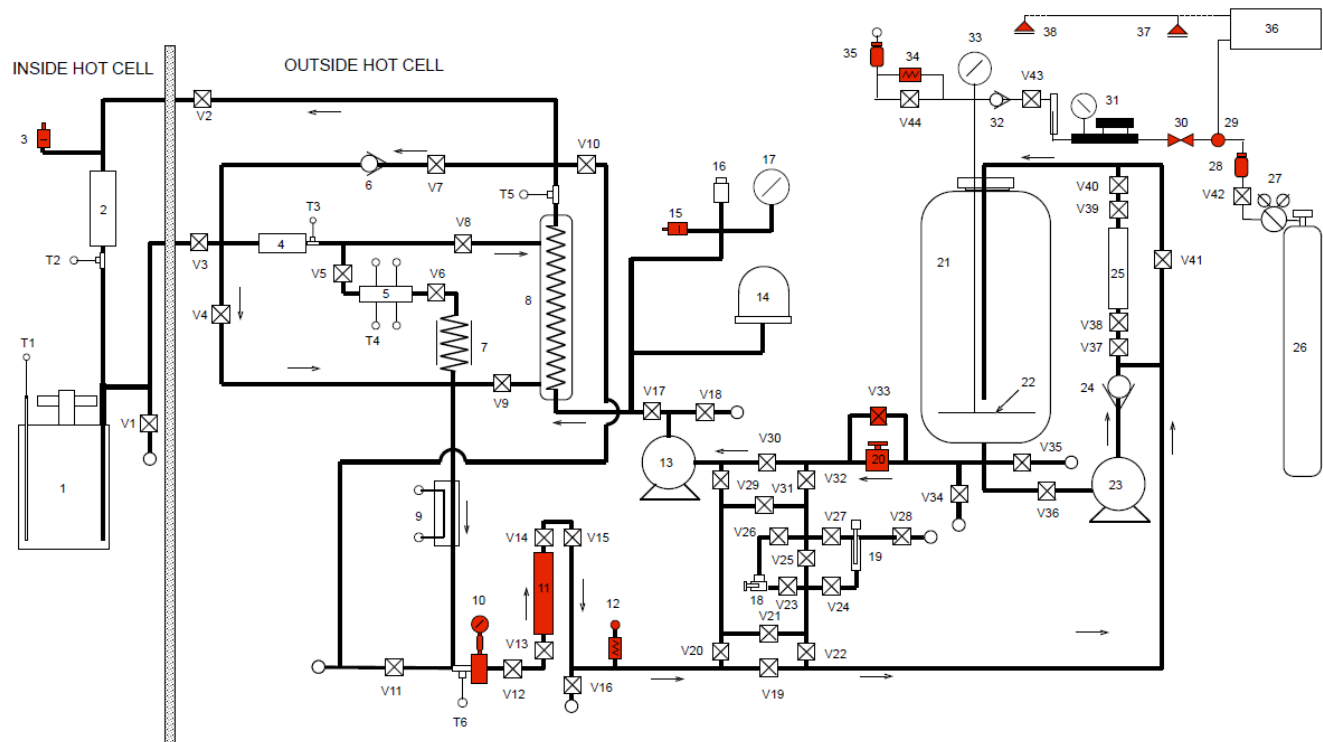
1. Autoclave	15. Rupture disk	29. Solenoid valve
2. Autoclave preheater	16. Pressure transducer	30. Excess flow valve
3. Rupture disk	17. High pressure gauge	31. Low-pressure regulator
4. ECP preheater	18. Conductivity sensor	32. Check valve
5. ECP cell	19. pH sensor	33. Vacuum & pressure gauge
6. Check valve	20. Solenoid valve	34. Pressure relief valve
7. Air Cooled Coil	21. Feedwater storage tank	35. Flash arrestor
8. Heat exchanger	22. Sparge tube	36. Hydrogen alarm control panel
9. Chilled block	23. Tank recirculation pump	37. Hydrogen leak sensors
10. Back-pressure regulator	24. Check valve	38. Hydrogen leak sensors
11. Ion exchange cartridge	25. Ion exchange cartridge	V = Valve
12. Pressure relief valve	26. Cover gas supply cylinder	T = Thermocouples
13. High-pressure pump	27. High-pressure regulator	
14. Accumulator	28. Flash arrestor	

Figure 3. Recirculation water loop for Cell 1 of the Irradiated Materials Laboratory. Items in red are safety significant components.

2.3 Test Methods

2.3.1 Crack growth rate test

In a crack growth rate (CGR) test, the crack is advanced with cyclic or constant loads while the propagation rate of the crack is monitored with a DCPD technique. The DCPD method is to measure the potential drop across the crack mouth and correlate the change in potential with the crack extensions by using a pre-calibrated correlation curve. Normally, a CGR test is started with cyclic loading to pre-crack the sample in a test environment. In this study, a load ratio (R) around 0.2-0.3, a frequency of 1-2 Hz, and a maximum stress intensity factor (K_{max}) between 10

and 16 MPa m$^{1/2}$ are used for pre-cracking. The objective of this step is to generate a sharp fatigue crack and to advance the crack tip beyond the area close to the machine notch.

The stress intensity factor (K) for a DCT specimen is calculated by: [22]

$$K = \frac{P}{(B \cdot B_N \cdot W)^{1/2}} \cdot \frac{(2 + \frac{a}{W})}{(1 - \frac{a}{W})^{3/2}} \cdot f(\frac{a}{W}) \tag{1}$$

where P is applied load; B is the specimen thickness; B_N is the net specimen thickness (or distance between the roots of the side grooves); a is crack length; and W is specimen width (measured from the load line to the back edge of the specimen). The geometry factor for a CT specimen is:

$$f(\frac{a}{W}) = 0.76 + 4.8\left(\frac{a}{W}\right) - 11.58\left(\frac{a}{W}\right)^2 + 11.43\left(\frac{a}{W}\right)^3 - 4.08\left(\frac{a}{W}\right)^4 \tag{2}$$

Once a fatigue crack is initiated, a series of cyclic test periods is carried out with gradually increasing rise times and load ratios. The measured CGRs in these test periods include the contributions from both mechanical fatigue and corrosion fatigue. With the change in loading conditions, the contribution of mechanical fatigue to the cyclic CGR is gradually reduced while the environmental effect is enhanced. The test is transitioned from cyclic CGR to constant-K SCC when significant environmental enhancement is obtained.

The SCC test is conducted under a constant-load mode at several stress intensity factors. Note that, as the crack advances during a SCC test, the applied load is reduced periodically to maintain an approximately constant K at the crack tip. While the stress intensity factor is kept at a "near-constant-K" condition during the SCC test, some test periods are also carried out with periodic partial unloading (PPU). With PPU, the specimen is unloaded briefly (normally 24 s) to a load ratio of 0.5-0.8 at a regular interval (1 to 4 hr). The objective of PPU is to straighten the crack front by fracturing the unbroken ligaments and to investigate the SCC response to the dynamic strain condition imposed by PPU. The relatively high load ratio and short unloading time ensure that the fatigue component of PPU is negligible in the overall CGR measured during the SCC test.

2.3.2 Fracture toughness J-R curve test

After a SCC CGR test is completed, a fracture toughness J-R curve test is conducted on the same sample and test environment. The test is performed with a constant stain rate of 0.43 µm/s, and the load and sample extension are recorded continuously outside the autoclave. The load-line displacement is determined by subtracting the extension of the load train, which has been measured prior to the test. During the test, the loading is interrupted periodically, and the specimen is held at a constant extension to measure crack length with the DCPD method. Before

each DCPD measurement, the sample stress is allowed to relax at a constant displacement for 30 s.

The J-integral was calculated from the load (P) vs. load-line displacement (v) curve according to ASTM Specification E 1820-08a.[22] The J is the sum of the elastic and plastic components,

$$J = J_{el} + J_{pl} \tag{3}$$

At a hold point, i, corresponding to a crack length, a_i, and v_i and P_i on the load vs. load-line displacement curve, the elastic component $J_{el(i)}$ is given by:

$$J_{el(i)} = \frac{(K_{(i)})^2 (1-\nu)^2}{E} \tag{4}$$

where ν is Poisson's ratio, and the stress intensity $K_{(i)}$ is calculated from Eqs. 1 and 2. The plastic component $J_{pl(i)}$ is given by:

$$J_{pl(i)} = \left[J_{pl(i-1)} + \left(\frac{\eta_{(i-1)}}{b_{(i-1)}} \right) \frac{A_{pl(i)} - A_{pl(i-1)}}{B_N} \right] \left[1 - \gamma_{(i-1)} \frac{a_{(i)} - a_{(i-1)}}{b_{(i-1)}} \right] \tag{5}$$

where $b_{(i-1)}$ is the remaining ligament at hold point $i-1$; $A_{pl(i)}$ is the area under the load vs. load-line displacement curve; and B_N is the net specimen thickness. Also, $\gamma_{(i)}$ and $\eta_{(i)}$ are factors that account for the crack growth effects on J during the test and are expressed as:

$$\eta_{(i-1)} = 2.0 + 0.522 \frac{b_{(i-1)}}{W} \tag{6}$$

$$\gamma_{(i-1)} = 1.0 + 0.76 \frac{b_{(i-1)}}{W} \tag{7}$$

The quantity $A_{pl(i)} - A_{pl(i-1)}$ is the increment of plastic area under the load vs. load-line displacement curve between lines of constant plastic displacement at hold points $i - 1$ and i. The plastic area under the load vs. load-line displacement record is given by

$$A_{pl(i)} = A_{pl(i-1)} + \frac{[P_i + P_{i-1}][v_{pl(i)} - v_{pl(i-1)}]}{2} \tag{8}$$

where the plastic components of the load-line displacement, $v_{pl(i)}$, is:

$$v_{pl(i)} = v_{(i)} - P_i C_{LL(i)} \tag{9}$$

In this equation, $v_{(i)}$ is the total load-line displacement, and $C_{LL(i)}$ is the compliance associated with a_i that can be determined as follows:

$$C_{LL(i)} = \frac{\left[1.62 + 17.80(a_i/W) - 4.88(a_i/W)^2 + 1.27(a_i/W)^3 \right]}{E' B_e [1 - (a_i/W)^2]} \tag{10}$$

where B_e is specimen effective thickness given by $B - (B - B_N)^2/B$ and $E'=E/(1 - \upsilon^2)$.

A J-R curve is constructed by fitting the calculated J values and corresponding crack lengths to a power law relationship. The J value at the intersection of the power law curve and the 0.2 mm offset blunting line, $J_{0.2}$, is reported. Note that a blunting line of four times the flow stress ($4\sigma_f$) is recommended by Mills[23] for materials with high strain hardening coefficients. Although the stain hardening coefficient is greatly reduced for irradiated SSs, [24,25] the ($4\sigma_f$) blunting line is still assumed in the present study to be more conservative in determining the $J_{0.2}$ values.

2.3.3 Fractographic examination

After each CGR/J-R test, the final crack front is marked with fatigue cycling in air at room temperature. The specimen is then broken, and the fracture surface is examined with a shielded scanning electron microscope (SEM). The CGR test and J-R test regions are identified, and their fracture morphologies are analyzed. The physical crack length is measured on the SEM images, and a 9/8 averaging technique is used to account for the uneven extensions at the crack front. With this technique, nine measurements are taken along the crack front across the width of the sample at equal intervals. The two near-surface measurements are averaged, and the resultant value is averaged with the remaining seven measurements. All crack extensions determined from the DCPD method are scaled proportionately to match the final crack length measured by SEM. All test results reported in the report have been corrected with SEM measurements.

This page is intentionally left blank.

3   RESULTS

3.1 Cold-Worked 316 SS at ~5 dpa

CGR and J-R curve tests

The CGR test on the CW 316 SS (specimen BR-01) irradiated at ~5 dpa was performed in high-purity water with low DO (<10 ppb). Prior to the test, the sample was soaked in the test environment at ~320°C for about 10 days to stabilize environmental conditions. Table 3 gives the applied loading variables and CGR results from this test. The crack-length history plots are shown in Fig. 4.

Fatigue precracking was started in the test environment with a triangular waveform at 2 Hz, a K_{max} of 10 MPa m$^{1/2}$, and a load ratio of 0.2. No significant crack extension was detected until the K_{max} was increased to ~18.4 MPa m$^{1/2}$. After about 240-μm crack extension, the K_{max} was reduced to ~11-13 MPa m$^{1/2}$. Then, the load ratio and rise time were gradually increased to induce environmentally assisted cracking. After repeated attempts, environmental enhancement started to appear in test period *o* with a K_{max} of ~12.5 MPa m$^{1/2}$ and a load ratio of 0.3. In the following test periods, slightly higher stress intensity factors and load ratios were employed to stabilize the environmental enhancement. After additional 250-μm crack extension, the test was transitioned to a constant-load SCC test.

The first constant-load test period (*1a* in Fig. 4g) was conducted with PPU every 2 hr at a stress intensity factor of 16.2 MPa m$^{1/2}$. The PPU consisted of a load cycle of 12 s down and 12 s up and a load ratio of 0.6. A CGR of 3.08 x 10^{-11} m/s was recorded over approximately 30-μm crack extension. After the PPU was removed in test period *1b*, the CGR was reduced by a factor of 5 to 6 under constant load at the same stress intensity level. The CGRs with and without PPU are significantly lower than those observed in BWR NWC for specimens irradiated from 0.75 to 3 dpa.[18, 26]

Next, the stress intensity factor was increased to ~20 MPa m$^{1/2}$, and constant-load CGRs were measured again with and without PPU between test periods *2a* and *2e*. As shown in Fig. 4h, the CGRs of the test periods with PPU (*2a*, *2c*, and *2e*) at a load ratio of 0.6 are much higher than those without PPU (*2b* and *2d*). While the CGRs without PPU are in the range of 10^{-11} m/s, the CGRs with PPU are a factor of 6 to 8 higher. The CGR with 4-hr hold time between PPU (*2e*) is slightly lower than those with 2-hr hold time (*2a* and *2c*), suggesting a hold time effect for the test periods with PPU.

The stress intensity factor was increased again in the following test periods, *3a-3e* (Fig. 4i), to ~26 MPa m$^{1/2}$. In test period *3a*, a CGR of 1.67 x 10^{-10} m/s was obtained with PPU and 4-hr hold time (at a load ratio of 0.6) over 35-μm crack extension. Once the PPU was removed, the measured CGR dropped by one order of magnitude in test period *3b*. The re-apply of PPU with 2-hr hold time resulted in an immediate increase in CGR in test period *3c*, and the measured CGR was about a factor of two higher than that of the 4-hr hold time, confirming the hold time

effect observed previously. The load ratio was increased to 0.7 in test periods *3d* and *3e* for hold times of 2 and 4 hr, respectively. The obtained CGRs were about a factor of three lower than those at 0.6 load ratio, suggesting a moderate effect of unloading magnitude on the CGRs with PPU.

Next, the constant-load CGRs were evaluated at ~33 MPa m$^{1/2}$ with and without PPU in test periods *4a-4d* (Fig. 4j). Again, the measured CGRs in those test periods with PPU were affected by hold times and load ratios. Furthermore, the crack extension increased sharply at each PPU, leading to a "stair-step" growth behavior on the crack length history plot. Without PPU, a CGR of 2.84 x 10^{-11} m/s was obtained over ~50-μm crack extension. The stress intensity factor was then increased further to ~39 MPa m$^{1/2}$ in test periods *5a-5c*. The "stair-step" crack growth became more evident at this stress level, as shown in Fig. 4k (*5a* and *5b*). While a substantial crack advance was registered right after each unloading cycle, the crack extension was minimal during hold times. With 2-hr hold time, an average CGR of 1.19 x 10^{-9} m/s was obtained. After the frequency of PPU was reduced to every 4 hr, the measured CGR decreased approximately a factor of two. This effect of unloading frequency is consistent with that observed in previous test periods, suggesting a dominant role of PPU in crack growth. Finally, the test was set to a constant load without PPU, and a CGR of 3.62 x 10^{-11} m/s was registered over a 23-μm crack extension.

Following the test at 320°C, the system temperature was lowered to ~288°C to evaluate the temperature dependence of crack growth behavior. Crack growth rates were measured at ~33 MPa m$^{1/2}$ with PPU in test period *6a* and *6b*, and then without PPU in test period *6c* (Fig. 4 l). While a similar stair-step growth was also observed at the low test temperature, the CGRs with PPU were slightly higher than those measured at 320°C with a similar stress intensity factor. Without PPU, however, the crack extension was short, and a CGR of 5 x 10^{-12} m/s was estimated for the test period.

Table 3. Crack growth rate test on ~5-dpa CW 316 SS (specimen BR-01) in a high-purity low-DO environment.

Test Period [1]	Test Time, h	Test Temp., °C	Load Ratio	Rise Time, s	Return Time, s	Hold Time, s	Kmax, MPa m$^{1/2}$	ΔK, MPa m$^{1/2}$	CGR in Env., m/s	CGR in Air, m/s	Crack Length, mm
Start	16.6										6.754
a	22.0	320	0.21	0.20	0.20	0.05	10.0	8.0	negligible	2.42E-08	6.755
b	38.7	320	0.20	0.20	0.20	0.05	11.9	9.5	3.22E-11	4.15E-08	6.757
c	45.2	320	0.20	0.21	0.21	0.04	13.0	10.4	negligible	5.53E-08	6.756
d	49.4	320	0.30	0.20	0.20	0.05	14.0	9.8	negligible	5.19E-08	6.758
e	64.2	319	0.31	0.81	0.81	0.19	13.9	9.6	1.13E-11	1.21E-08	6.757
f	69.3	320	0.30	0.21	0.21	0.04	15.1	10.5	negligible	6.42E-08	6.758
g	71.1	320	0.30	0.21	0.21	0.04	18.4	12.8	4.63E-08	1.21E-07	6.865
h	72	320	0.30	0.42	0.42	0.08	16.4	11.4	5.55E-08	4.19E-08	6.931
i	73.3	320	0.30	0.41	0.41	0.09	14.4	10.0	4.16E-08	2.83E-08	6.994
j	87.7	320	0.40	0.36	0.36	0.14	10.2	6.1	1.00E-11	6.83E-09	6.994
k	90.7	320	0.30	0.39	0.39	0.11	11.2	7.8	negligible	1.31E-08	6.995
l	92.6	320	0.30	0.40	0.40	0.10	13.4	9.3	2.05E-08	2.27E-08	7.048
m	95.6	320	0.30	0.39	0.39	0.11	11.3	7.9	6.31E-10	1.34E-08	7.052
n	97	320	0.30	0.39	0.39	0.11	12.3	8.6	1.33E-08	1.77E-08	7.076

Table 3. (Cont'd)

Test Period [1]	Test Time, h	Test Temp., °C	Load Ratio	Rise Time, s	Return Time, s	Hold Time, s	Kmax, MPa m$^{1/2}$	ΔK, MPa m$^{1/2}$	CGR in Env., m/s	CGR in Air, m/s	Crack Length, mm
o	99.7	320	0.30	0.79	0.79	0.21	12.4	8.7	1.48E-08	9.07E-09	7.134
p	104	320	0.41	2.26	0.75	0.74	12.4	7.3	4.81E-09	1.98E-09	7.174
q	120.3	320	0.51	7.16	0.72	2.84	12.4	6.1	8.82E-10	3.77E-10	7.209
r	143.7	320	0.55	20.9	3.49	9.06	12.4	5.5	7.29E-11	9.99E-11	7.213
s	160.1	320	0.50	21.6	3.60	8.38	12.4	6.2	1.13E-10	1.33E-10	7.216
t	207.4	320	0.40	22.7	3.78	7.34	12.4	7.5	3.75E-10	2.12E-10	7.255
U	232.3	320	0.45	44.4	8.89	15.6	12.5	6.9	1.44E-10	8.81E-11	7.266
V	260.5	320	0.50	44.2	8.84	15.8	13.5	6.8	3.04E-10	8.87E-11	7.287
W	280.3	320	0.50	45.0	9.00	15.0	14.6	7.3	6.44E-10	1.11E-10	7.318
X	309.2	320	0.50	90.0	9.00	30.0	14.6	7.4	2.83E-10	5.66E-11	7.339
Y	352.6	320	0.49	225.2	9.01	74.8	14.7	7.4	1.89E-10	2.31E-11	7.360
Z	386	321	0.59	360.5	8.65	139.5	15.8	6.4	1.07E-10	9.63E-12	7.372
aa	433	321	0.59	723.3	8.68	276.7	15.9	6.5	8.90E-11	5.00E-12	7.381
ab	479.9	321	0.59	728.2	8.74	271.8	16.4	6.6	8.44E-11	5.44E-12	7.393
1a	711.7	321	0.60	12	12	7200	16.2	6.5	3.08E-11	5.06E-13	7.422
1b	905.3	321	1.00	-	-	-	16.3	-	5.43E-12	-	7.426
2a	977.9	321	0.60	12	12	7200	20.0	8.0	7.95E-11	1.02E-12	7.455
2b	1074	320	1.00	-	-	-	20.0	-	1.03E-11	-	7.458
2c	1148.5	320	0.60	12	12	7200	20.1	8.1	7.15E-11	1.04E-12	7.479
2d	1313.7	320	1.00	-	-	-	20.1	-	1.41E-11	-	7.486
2e	1531	319	0.60	12	12	14400	20.3	8.1	6.02E-11	5.28E-13	7.531
3a	1561	319	0.60	12	12	14400	25.6	10.2	1.67E-10	1.14E-12	7.567
3b	1697	320	1.00	-	-	-	25.7	-	1.75E-11	-	7.575
3c	1722	320	0.60	12	12	7200	25.8	10.3	3.19E-10	2.34E-12	7.604
3d	1769.5	320	0.70	12	12	7200	25.7	7.7	1.16E-10	9.76E-13	7.625
3e	1865	319	0.70	12	12	14400	25.9	7.8	5.36E-11	4.97E-13	7.646
4a	1890	318	0.60	12	12	7200	32.5	13.0	6.48E-10	5.03E-12	7.719
4b	1914	318	0.60	12	12	14400	32.6	13.0	3.22E-10	2.53E-12	7.747
4c	1945.5	319	0.70	12	12	14400	32.7	9.8	1.77E-10	1.07E-12	7.767
4d	2393.6	317	1.00	-	-	-	32.8	-	2.84E-11	-	7.819
5a	2401.7	317	0.60	12	12	7200	38.7	15.5	1.19E-09	8.90E-12	7.900
5b	2425.8	318	0.60	12	12	14400	38.5	15.4	5.37E-10	4.38E-12	7.952
5c	2600	319	1.00	-	-	-	38.7	-	3.62E-11	-	7.975
6a	2642.3	287	0.60	12	12	7200	33.3	13.3	9.53E-10	5.06E-12	8.063
6b	2660.7	287	0.60	12	12	14400	33.4	13.4	4.49E-10	2.57E-12	8.093
6c	2854.5	289	1.00	-	-	-	33.3	-	4.97E-12	-	8.095

[1] Cyclic test periods are named in alphabetical order, and constant-load test periods are named in numerical order.
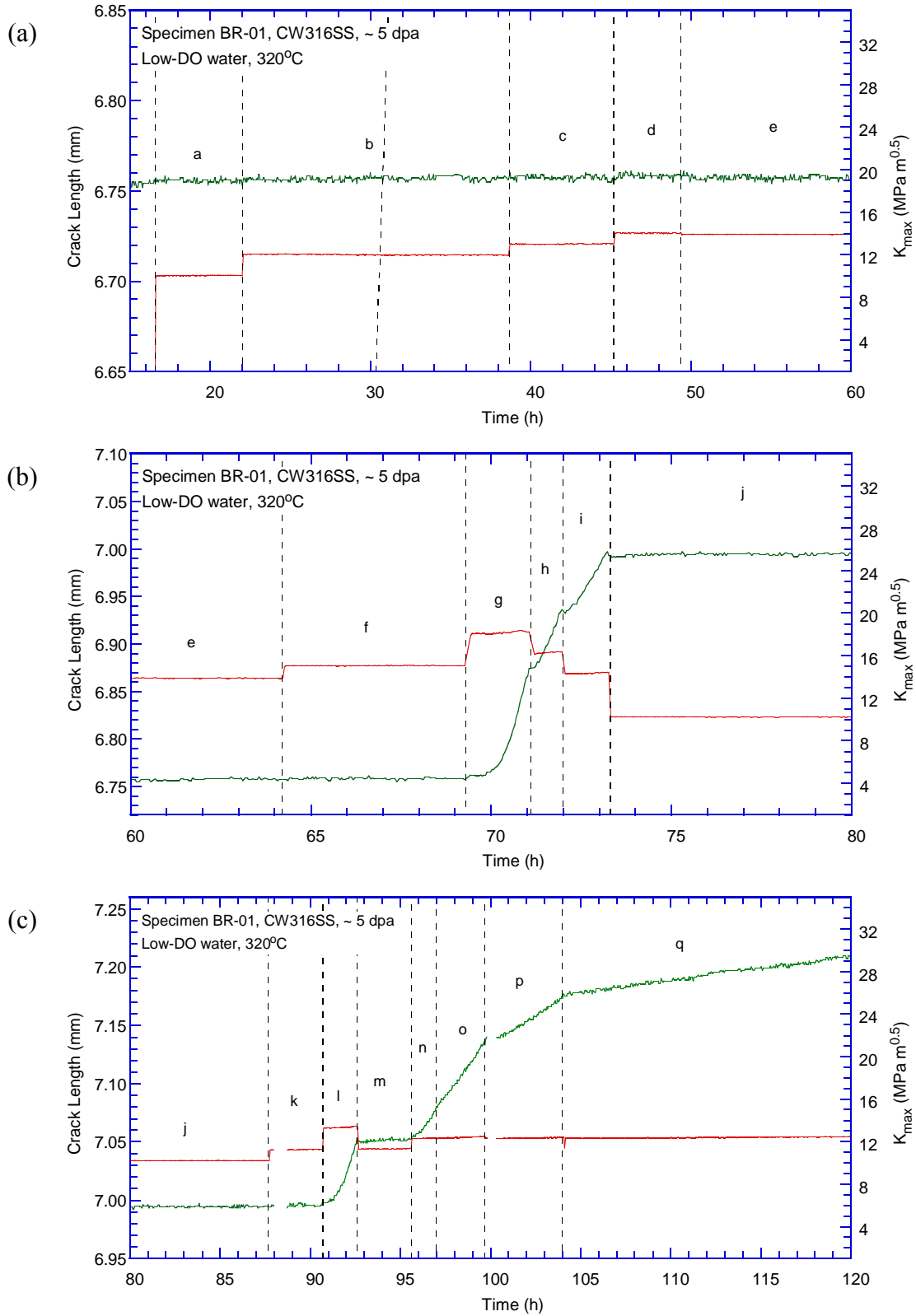
Figure 4. Crack-length-vs.-time plot for specimen BR-01 (~5-dpa CW 316 SS) tested in low-DO high-purity water: test periods (a) a-e, (b) e-j, (c) j-q, (d) r-t, (e) u-y, (f) x-1, (g) 1a-1b, (h) 2a-2e, (i) 3a-3e, (j) 4a-4d, (k) 5a-5c, and (l) 6a-6c.

Figure 4. (Cont'd)

(g)

Specimen BR-01, CW316SS, ~ 5 dpa
Low-DO water, 320°C

1a
PPU, 2 hr

1b
Constant-load

(h)

Specimen BR-01, CW316SS, ~ 5 dpa
Low-DO water, 320°C

2a
PPU, 2 hr

2b
Constant -load

2c
PPU, 2hr

2d
Constant -load

2e
PPU, 4 hr

(i)

Specimen BR-01, CW316SS, ~ 5 dpa
Low-DO water, 320°C

3a
PPU, 4 hr

3b
Constant -load

3c
PPU, 2hr,
R=0.6

3d
PPU, 2 hr,
R=0.7

3e
PPU, 4 hr,
R=0.7
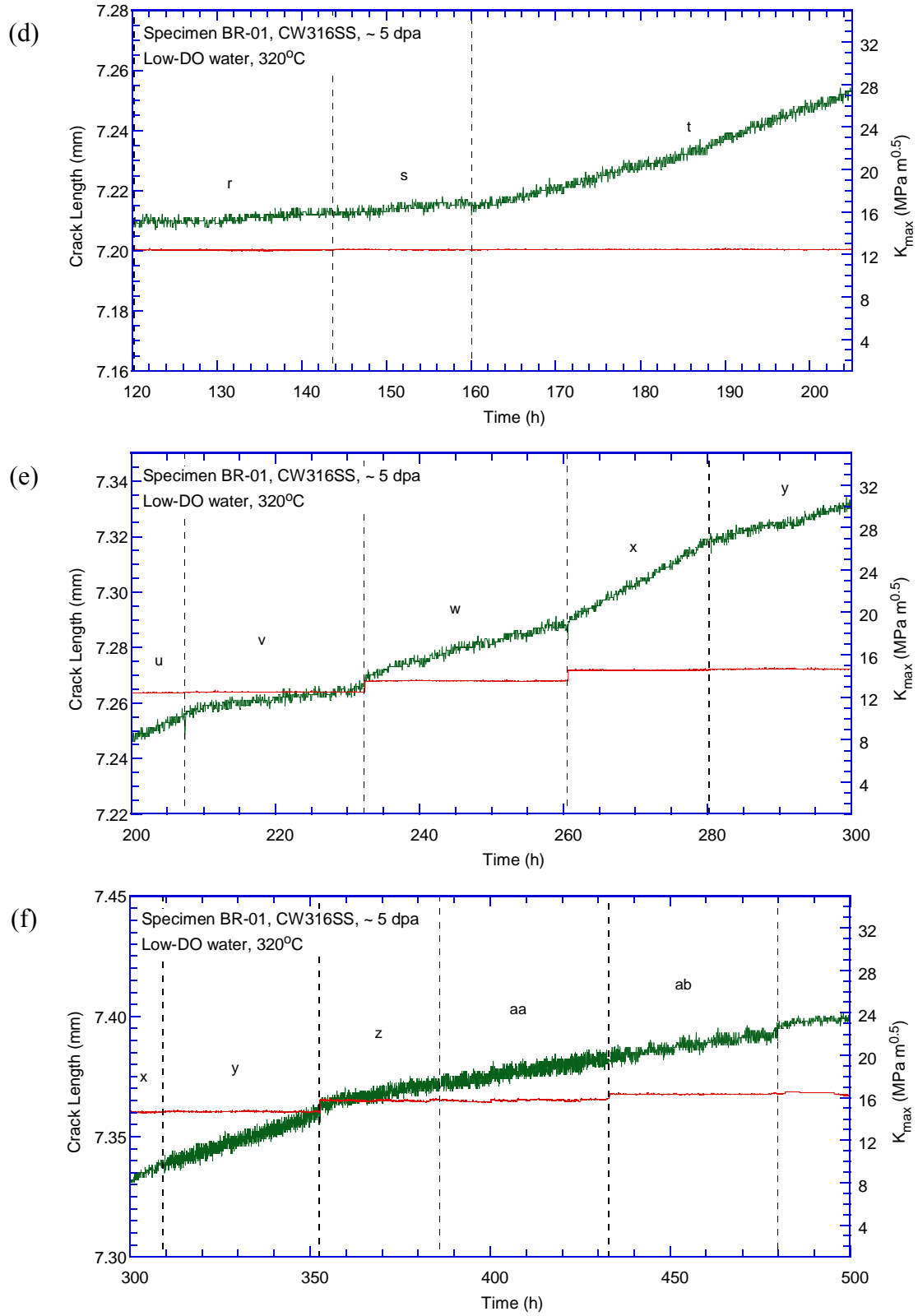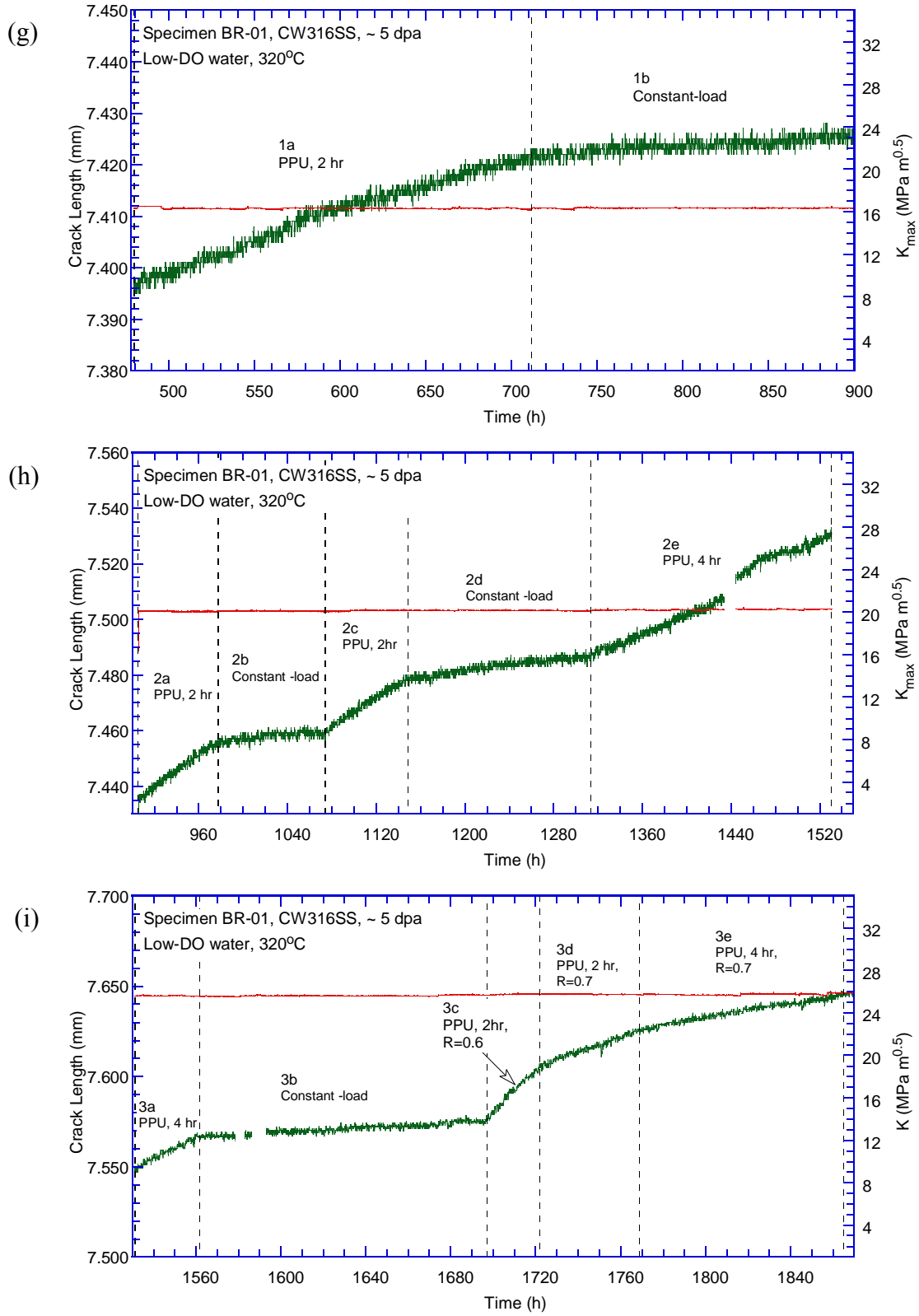
Figure 4. (Cont'd)
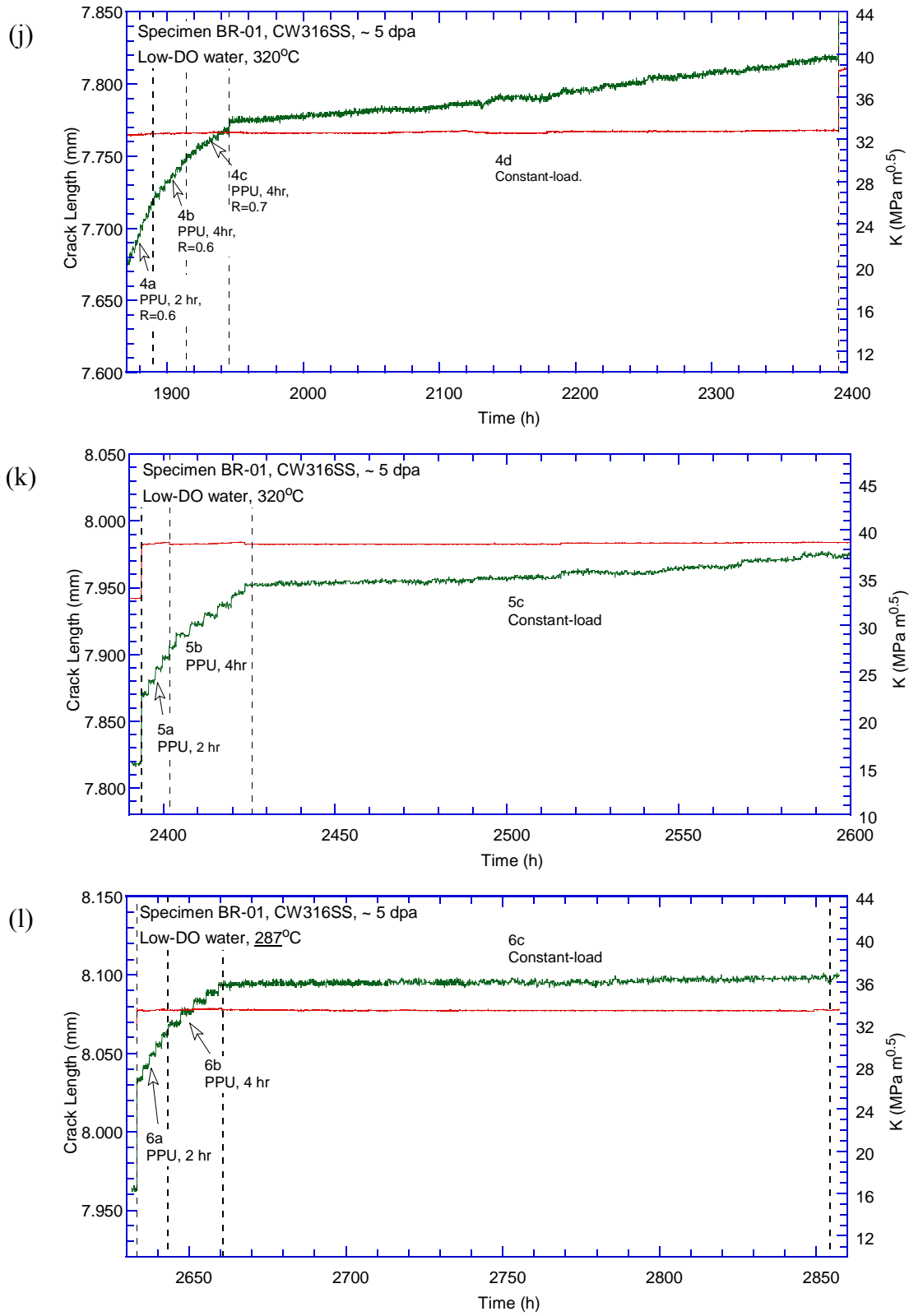
Figure 4. (Cont'd)

Cyclic CGRs obtained from specimen BR-01 are plotted as a function of fatigue CGRs in air as shown in Fig. 5. Most of the data points are, as expected, above the diagonal line, indicating an environmental enhancement in fatigue crack growth. The degree of the enhancement becomes more pronounced at the low growth rate region with increasing load ratio and rise time. Along with the cyclic CGRs, a corrosion fatigue (CF) curve initially developed by Shack and Kassner [27] for a high-purity water environment with 0.2 ppm DO is also included in the figure for reference. Most of the data points in Fig. 5 are bounded by this CF curve, suggesting a good resistance to corrosion fatigue of the CW 316 SS at ~5 dpa.
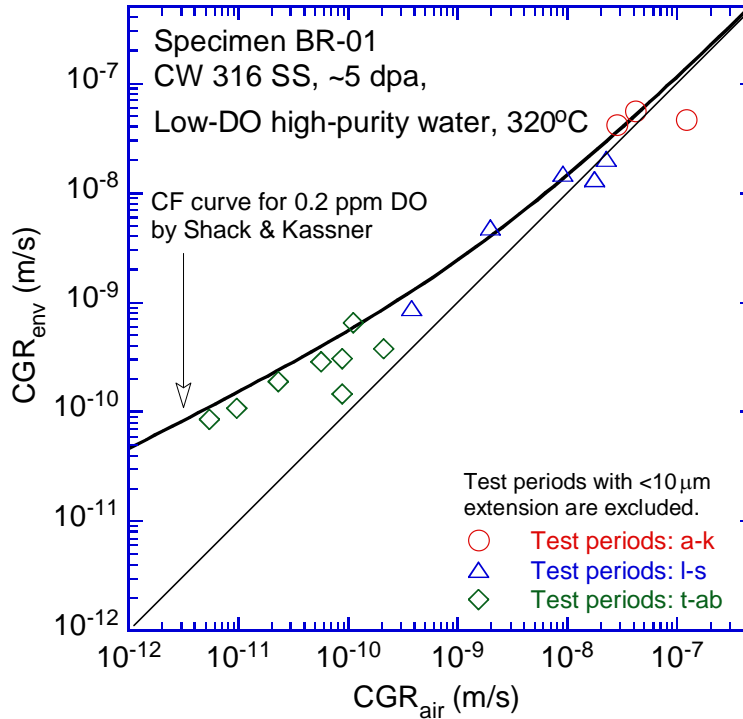
Figure 5. Cyclic CGRs of specimen BR-01.

All SCC CGRs obtained from the constant-load test are plotted as a function of stress intensity factor in Fig. 6. The open symbols are for the test periods with PPU, and the closed symbols are for the test periods without PPU. The NUREG-0313 curve [28] is included in the figure for reference. Without PPU, the SCC CGRs are about one order of magnitude lower than the NUREG-0313 curve, suggesting a good SCC resistance. This result is consistent with the good CF performance observed in the cyclic test. With PPU, however, the measured CGRs are significantly higher, and some of data points are close to and above the NUREG-0313 curve at high stress intensity factors. The effect of unloading frequency can also be seen with 2- and 4-hr hold time in Fig. 6. The effect of test temperature is inconclusive between 287 and 320°C for this sample. While the CGR with PPU decreases slightly with increasing temperature, the CGR without PPU increases more significantly with increasing test temperature. However, due to the extremely low growth rate, the CGR without PPU at 287°C was obtained with less than 2 μm crack extension, and may thus not be as accurate.
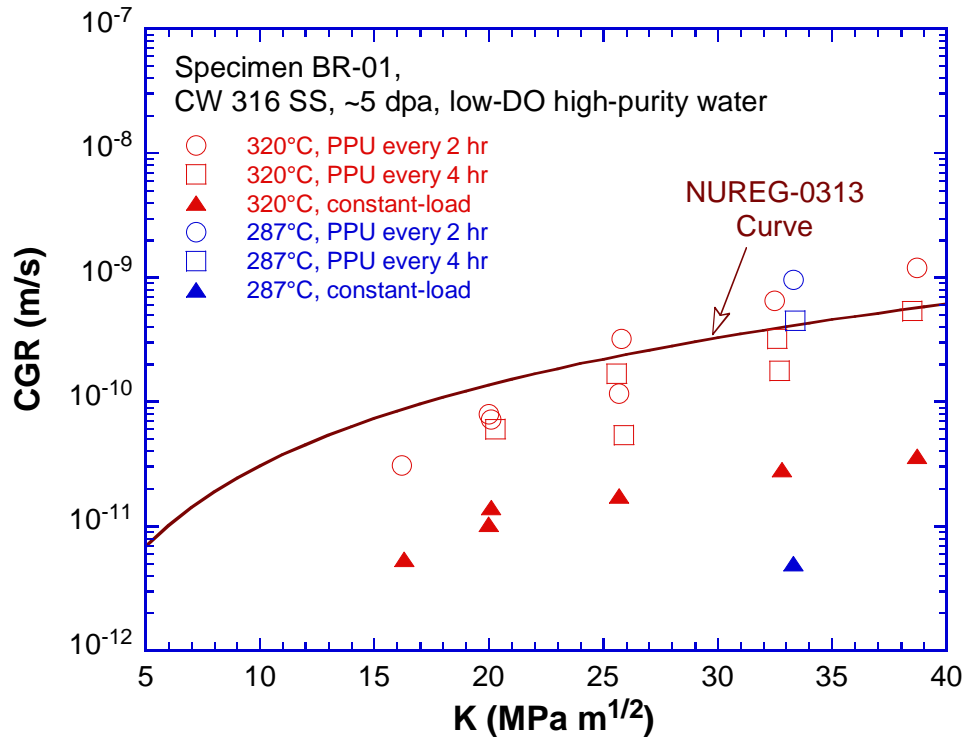
Figure 6. SCC CGRs of specimen BR-01 with PPU (open symbols) and without PPU (closed symbols).

After the CGR test, a few fatigue loading cycles were applied on the sample to mark the final crack front. A fracture toughness J-R curve test was performed on the same sample in the test environment. Shortly after the J-R test was started, the sample fractured unexpectedly in a brittle fashion. This early failure suggested severe irradiation embrittlement, and the estimated fracture toughness was about 46 MPa m$^{1/2}$ for this 5-dpa CW 316 SS specimen.

Fractographic examination

Following the CGR and J-R curve test, an SEM examination was performed on the fracture surface. Figure 7 shows the entire crack front of the specimen. The sample appears to be heavily deformed in the direction of crack propagation. The elongated deformation microstructure along the rolling direction was clearly visible in the J-R curve test region. In the CGR test region, the measured crack size was about 39% greater than that estimated by the DCPD measurement. Thus, the crack extension was scaled proportionally to match the final crack size measured on the fracture surface. Note that all test results presented in this report have been corrected with SEM measurements.

Figure 8 is an enlarged view of the fracture surface along the sample central line. Transgranular cracking is the main fracture mode observed during the cyclic CGR test. As the crack advances deeper, IG cracking starts to develop and gradually becomes the dominant fracture morphology (Fig. 9). A mixed-mode of IG and small isolated ductile areas and secondary cracking can also be seen in the constant-load CGR test region. Finally, the J-R curve test region shows a mix of

dimples and banded fracture along the rolling direction (Fig. 10). Small stringer-shaped inclusions along the deformation bands can also be seen on the fracture surface. This banded microstructure resulting from cold-work and stringer inclusions may play a key role in the brittle fracture that occurred in this sample during the J-R curve test.
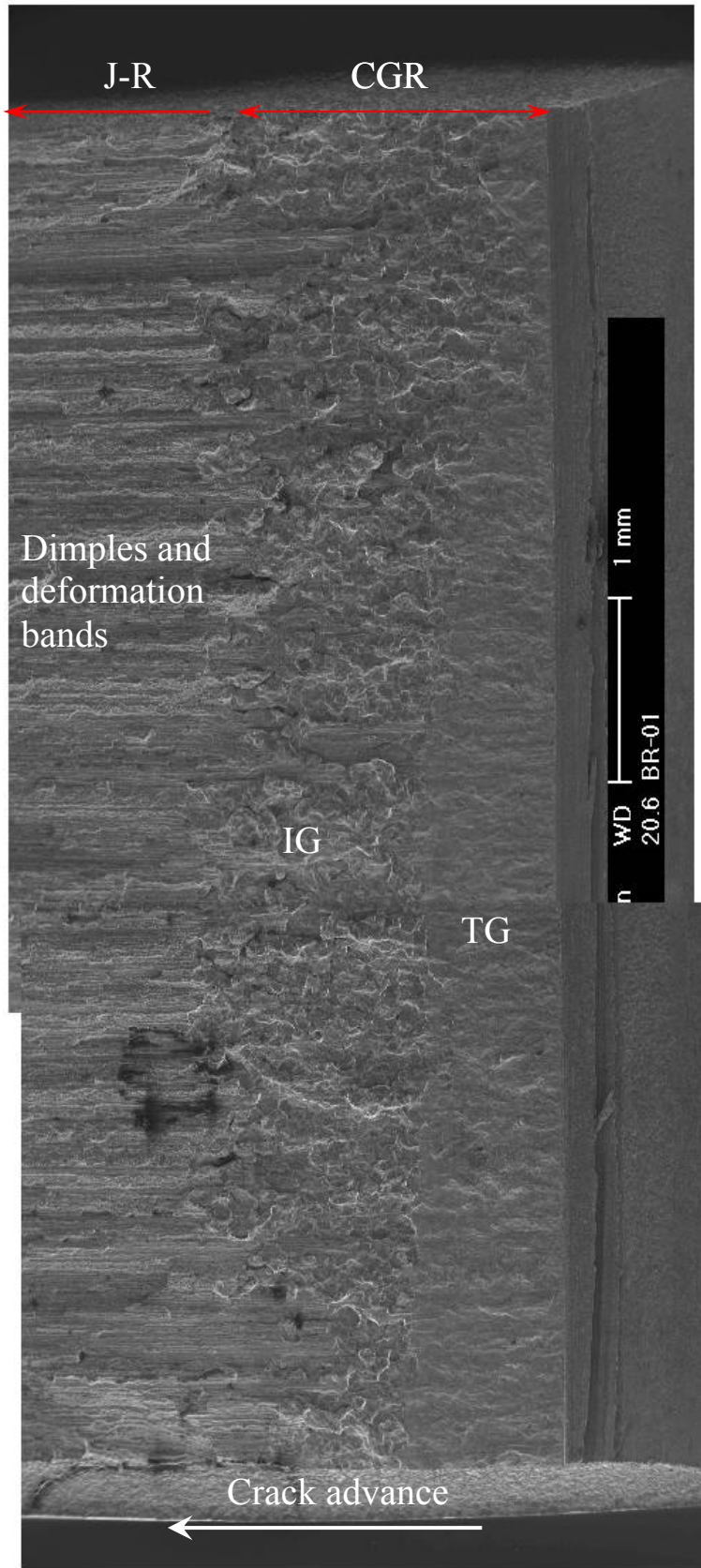
Figure 7. Fracture surface of specimen BR-01 tested in low-DO high-purity water.

Figure 8. Fracture surface of specimen BR-01 along the sample central line.

Figure 9. Intergranular cracking during the constant-load CGR test of specimen BR-01.

Figure 10. Dimples and banded fracture with stringer inclusions (red arrows) during the J-R curve test of specimen BR-01.

3.2 Cold-Worked 316-Ti SS

3.2.1 Cold-worked 316-Ti SS at ~5 dpa

CGR and J-R curve tests
The Ti-stabilized CW 316 SS irradiated at ~5-dpa (specimen CR-01) was also tested in high-purity water with low DO (<10 ppb). Prior to the test, the sample was soaked in the test environm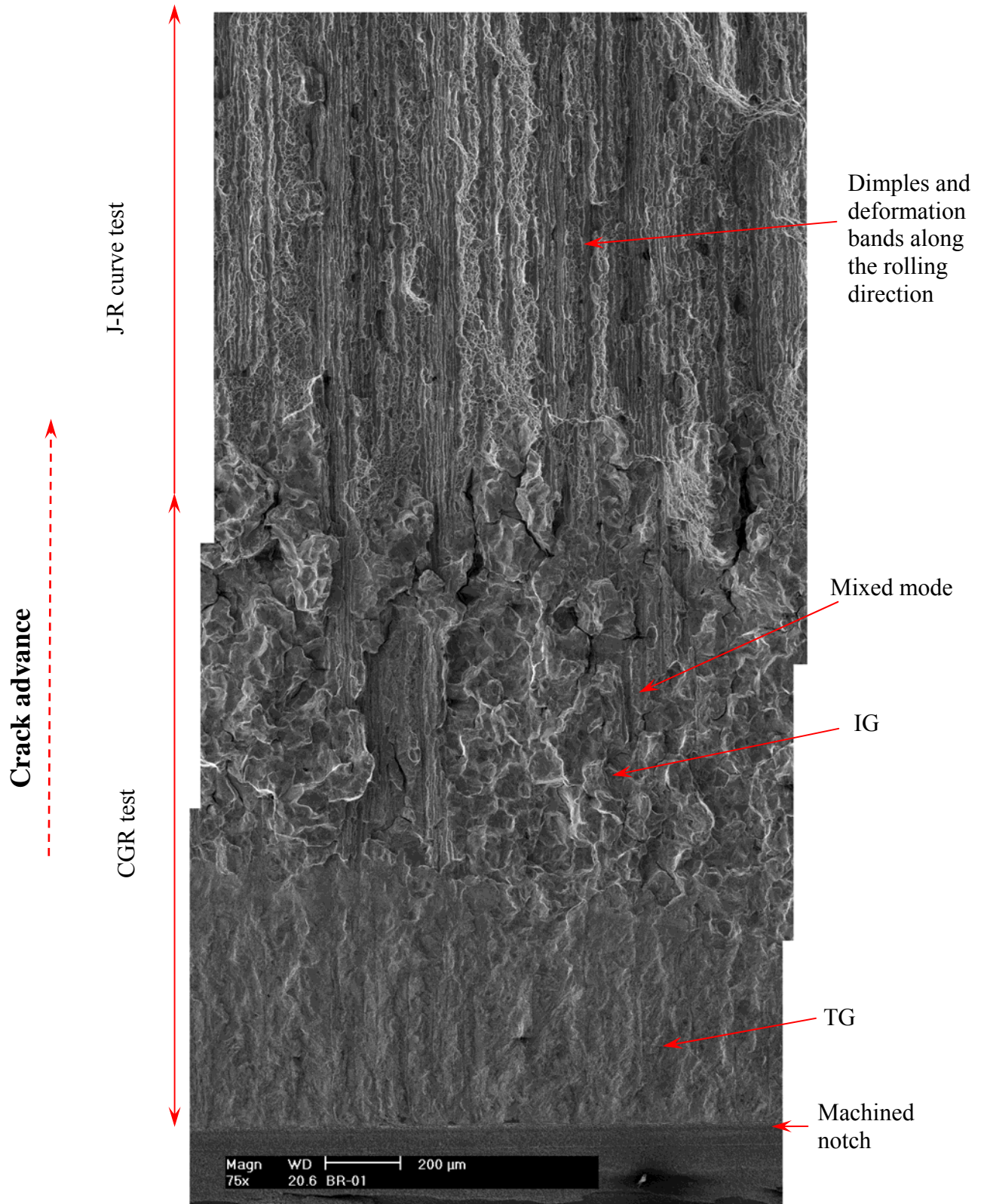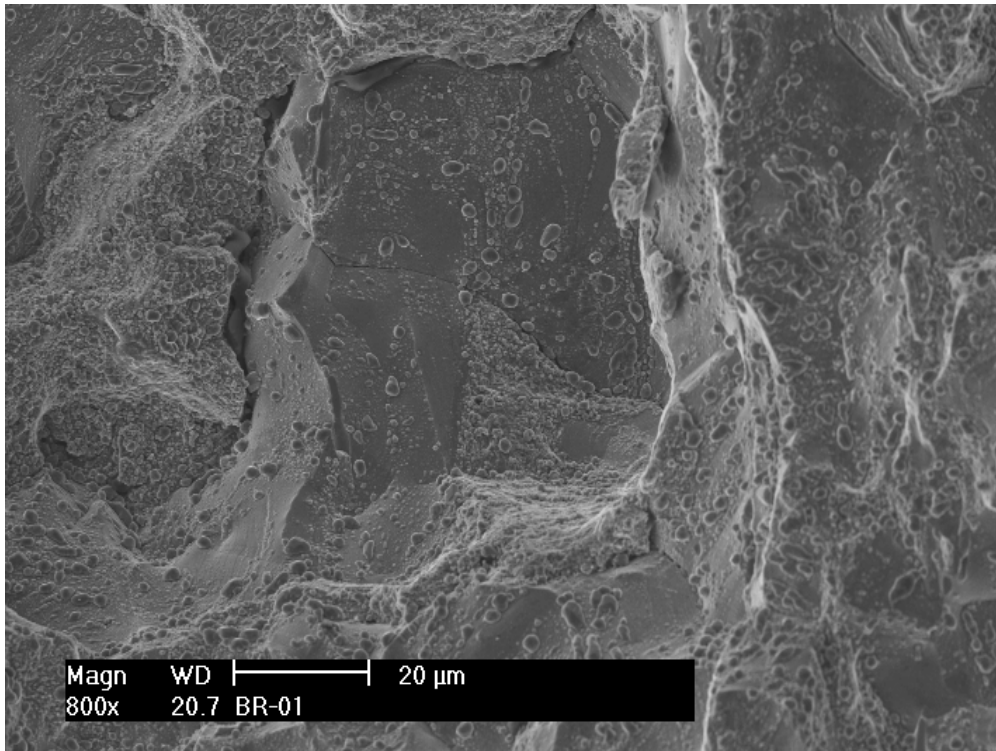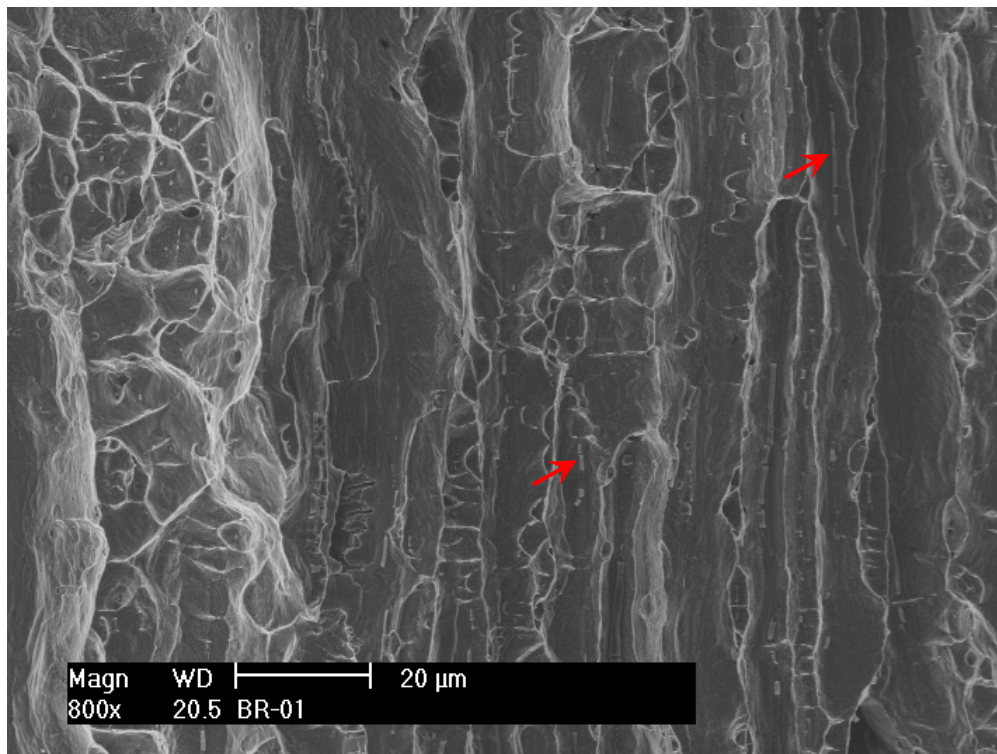ent at ~320°C for about 10 days to stabilize environmental conditions. Table 4 gives the test conditions and CGR results. The crack-length history plots of this test are shown in Fig. 11.

The cyclic CGR test was started with a triangle waveform at 1 Hz, a K_{max} of 15 MPa $m^{1/2}$, and a load ratio of 0.2. After a stable crack growth was established, the maximum stress intensity factor was lowered to approximately 13 MPa $m^{1/2}$. With gradually increased rise times and load ratios, environmentally enhanced cracking was readily observed at this low stress intensity (in Fig. 11a-b, test periods *d-k*). After ~330 hr and ~400-μm crack extension, the measured CGR in the test environment was nearly one order of magnitude higher than that in air. While the test was gradually transitioned to a SCC test, the autoclave heater was unexpectedly tripped, leading to a significant temperature drop. The sample had to be unloaded while the autoclave temperature was recovered. A small leak at the seal of the pull rod was attributed to the temperature fluctuation. After the autoclave temperature was re-stabilized, the test was resumed in test period *m*. Despite a similar loading condition, the crack seemed to stall after the restart, and the previously obtained environmental enhancement vanished. Little crack extension was measured in test periods *n* to *p*. To re-initiate cracking, the load ratio was lowered to about 0.5 in the following test periods (*q*, *r*, and *s*). The obtained CGRs were very close to the values measured before. However, the crack stalled again in test period *t* with the increase of rise time. The crack did not response very well to the reduced rise times in the following test periods. Another temperature drop was detected in test period *z*, and the pre-cracking had to be restarted again after the temperature was stabilized.

Starting from test period *aa*, the crack was re-initiated at ~14 MPa $m^{1/2}$ with a load ratio of 0.4-0.5. After nearly ~400-μm crack extension, environmental enhancement was eventually stabilized in test periods *an* and *ao* (Fig. 11h). The test was then set to a constant load at ~14.5 MPa $m^{1/2}$ with PPU (R=0.5) of every 2 hr. A CGR of 9.5 x 10^{-11} m/s was measured over a 34-μm crack extension in test period *1a*. Then, the hold time was increased further to 4 hr in the next test period, *1b*, and a similar CGR (~9.5 x 10^{-11} m/s) was obtained. In test period *1c*, the PPU was removed, and a CGR of 9.0x10^{-11} m/s was recorded over a 65-μm crack extension. It appears that the PPU has no effect on the SCC CGRs at this stress level.

Next, the stress intensity was increased to ~19.3 MPa $m^{1/2}$. The test was first performed under a constant load without PPU. An average CGR of 1.5 x 10^{-10} m/s was measured over ~100-μm crack extension. To investigate the effect of dynamic loading condition, PPU (R=0.5) was introduced in test period *2b* with 4-hr hold time. As shown in Fig. 11j, a significant jump in crack length (~20 μm) was recorded for each unloading, while very low crack growth rates can be seen between two subsequent PPU. This stair-step crack growth behavior was identical to

what we observed previously in the ~5-dpa CW 316 SS tested in the same high-purity low-DO environment. It is clear that PPU has a significant impact on crack growth behavior above a certain stress threshold (in this case, 14.5-19.5 MPa m$^{1/2}$) in a low-corrosion-potential environment. To further evaluate the effect of PPU, the unloading ratio was increased to 0.7 in the next two test periods, *2c* and *2d*, with 4- and 2-hr hold times, respectively. While the same stair-step growth behavior was still observed, a much smaller step height (<10 μm) was found with the increased load ratio. In test period *2e*, the hold time between PPU was increased back to 4 hr. Soon after the test period started, the fuse of the autoclave heater failed unexpectedly. The system had to be cooled briefly for repair. After the autoclave temperature was re-stabilized, the test was resumed, and the test condition for test period *2e* was repeated.

The SCC CGR was then evaluated at a higher stress intensity factor, about 25 MPa m$^{1/2}$ (see Fig. 11k). Again, the CGRs with and without PPU were measured. A similar stair-step cracking behavior was also observed at this stress intensity level. The CGRs measured in the test periods with PPU were dominated by the frequency and magnitude of unloading. In the test period without PPU (period *3c*) the crack growth was not very stable, and an average CGR of 2.7 x 10^{-10} m/s was recorded over ~130-μm crack extension for the entire test period.

When the stress intensity factor was raised to ~31 MPa m$^{1/2}$ in test period *4*, an unstable crack extension about ~60 μm was recorded (as shown in Fig. 11l). The first test stage (*4a*) was conducted with PPU at R=0.7 every 2 hr, and the stair-step growth behavior was evident. Each PPU yielded a 25-30 μm crack extension. Once the PPU was removed in test stage *4b*, a steady CGR of 3.0 x 10^{-9} m/s was recorded over a ~200-μm crack extension. This growth rate is similar to that observed between PPU in test stage *4a*. The SCC CGR measurements were repeated at the same stress intensity level with and without PPU in test stages *4c* and *4d*, respectively. A significant crack extension (~40-50 μm) was again observed during PPU (in test stage *4c*), and a similar growth rate (~2.2 x 10^{-9} m/s) was obtained under the constant-load condition without PPU (*4d*). These high growth rates suggest that the CR heat is highly susceptible to IASCC at this stress intensity factor.

For test period *5*, the stress intensity factor was lowered to ~19.6 MPa m$^{1/2}$, a stress level corresponding to that in test period *2*. The crack was stalled, and a much lower CGR was recorded with approximately 10-μm crack extension. It appeared that the high loading stress in the previous test period (test period *4*, ~32.5MPa m$^{1/2}$) had a significant effect on the cracking behavior. To re-activate the cracking, the load was raised back to a stress intensity factor similar to that used in test period *4*. After about 40 hr, the rapid crack growth was re-established, and a CGR of ~2.0 x 10^{-9} m/s was obtained in the later part of test period *6*. To verify this effect of loading history on cracking behavior, the stress intensity factor was reduced again in test period *7*. Again, the crack was arrested following a test period at a higher stress level.

Before the CGR test was concluded for this sample, two additional constant-load test periods, *8* and *9*, were carried out. A CGR of 4.0 x 10^{-9} m/s was obtained at ~30.9 MPa m$^{1/2}$ in test period *8*. This value was slightly higher than those obtained in previous test periods at a similar stress

level. At 37.7 MPa m$^{1/2}$, a CGR of 5.3 x 10^{-9} m/s was recorded over ~300-µm crack extension in test period *9*.

Table 4. Crack growth rate test on ~5-dpa CW 316-Ti SS (specimen CR-01) in a high-purity low-DO environment.

Test Period [1]	Test Time, h	Test Temp., °C	Load Ratio	Rise Time, s	Return Time, s	Hold Time, s	Kmax, MPa m$^{1/2}$	ΔK, MPa m$^{1/2}$	CGR in Env., m/s	CGR in Air m/s	Crack Length, mm
Start	2.9										6.935
a	4.09	320	0.21	0.46	0.46	0.04	15.1	12.0	2.71E-08	3.98E-08	6.990
b	5.88	320	0.20	0.46	0.46	0.04	14.2	11.4	2.39E-08	3.33E-08	7.057
c	9.31	320	0.20	0.45	0.45	0.05	13.3	10.6	1.36E-08	2.69E-08	7.123
d	11.59	320	0.30	1.79	1.79	0.21	13.3	9.3	6.75E-09	4.92E-09	7.146
e	21.8	320	0.41	4.38	1.75	0.62	13.3	7.8	3.24E-09	1.29E-09	7.222
f	33.1	320	0.51	8.53	1.71	1.47	13.1	6.4	1.30E-09	3.86E-10	7.259
g	55.8	319	0.50	25.7	4.28	4.34	13.2	6.6	4.59E-10	1.36E-10	7.287
h	79.4	319	0.55	25.3	10.1	4.72	13.3	6.0	5.95E-10	1.06E-10	7.317
i	104	319	0.60	49.6	9.92	10.42	13.3	5.3	4.30E-10	3.89E-11	7.340
j	166.2	319	0.64	121.2	9.70	28.8	13.4	4.8	1.54E-10	1.12E-11	7.369
k	334.3	319	0.69	234.1	9.37	65.8	13.1	4.0	2.30E-11	3.48E-12	7.379
l	338	319	0.59	248.5	9.94	51.5	13.3	5.5	1.74E-10	8.26E-12	7.384
Heater tripped, unload to recover AC temperature											
m	365 - 636	319	0.59	248.5	9.94	51.5	13.4	5.5	4.63E-11	8.51E-12	7.432
n	843	319	0.59	828.1	9.94	171.9	13.3	5.5	negligible	2.54E-12	7.431
o	864	319	0.59	414.2	9.94	85.8	13.4	5.5	negligible	5.12E-12	7.430
p	888.3	319	0.54	421.7	10.12	78.3	13.4	6.2	5.16E-11	6.92E-12	7.433
q	910	319	0.50	128.2	10.26	21.8	13.4	6.8	3.34E-10	2.99E-11	7.454
r	957	319	0.54	252.7	10.11	47.3	13.5	6.2	1.29E-10	1.16E-11	7.472
s	1105	319	0.54	421.5	10.12	78.5	13.5	6.2	9.47E-11	7.20E-12	7.513
t	1223	319	0.48	857.4	10.29	142.6	13.6	7.0	7.11E-12	4.91E-12	7.518
u [2]	1350	319	0.50	256.4	10.26	43.6	13.7	6.8	2.21E-11	1.55E-11	7.521
v	1367	320	0.49	171.3	10.28	28.6	13.7	7.0	negligible	2.44E-11	7.519
w	1389	319	0.54	141.4	8.48	58.6	13.5	6.2	1.83E-11	2.09E-11	7.522
x	1438	320	0.50	36.2	8.70	13.8	13.4	6.8	5.77E-11	1.05E-10	7.530
y	1510	319	0.53	7.16	1.43	2.84	13.7	6.5	9.76E-11	4.81E-10	7.549
z	1514.7	321	0.30	1.58	1.58	0.42	13.9	9.7	3.72E-09	6.43E-09	7.569
Temperature unstable between 1514.8 hr and 1542 hr											
aa	1542 - 1557.4	319	0.40	3.81	3.81	1.19	13.9	8.3	1.00E-09	1.79E-09	7.588
ab	1582	319	0.41	11.37	3.79	3.63	13.9	8.2	5.26E-10	5.76E-10	7.609
ac	1606	319	0.51	21.74	3.62	8.26	13.9	6.9	3.30E-11	1.86E-10	7.608
ad	1641	320	0.41	22.78	3.80	7.22	13.9	8.2	3.96E-11	2.94E-10	7.609
ae [3]	1702	319	0.36	23.21	3.87	6.79	13.9	9.0	5.31E-10	3.63E-10	7.646
af	1776	320	0.40	22.79	3.80	7.21	13.9	8.3	6.15E-11	3.03E-10	7.661
ag	1799	319	0.35	3.71	3.71	1.29	14.1	9.2	2.43E-09	2.41E-09	7.747
ah	1811	319	0.36	9.18	3.69	3.26	14.1	9.0	2.37E-09	9.35E-10	7.801
ai	1824	319	0.41	8.66	3.61	3.34	14.2	8.4	2.25E-09	8.27E-10	7.861
aj	1834.6	319	0.45	21.15	3.52	8.85	14.2	7.8	1.23E-09	2.75E-10	7.887
ak	1846.6	320	0.45	42.41	8.48	17.59	14.3	7.9	9.61E-10	1.43E-10	7.911
al	1859	319	0.44	106.2	8.49	43.83	14.3	8.0	6.14E-10	5.85E-11	7.930
am	1884	319	0.44	212.5	8.50	87.53	14.3	8.0	4.23E-10	2.98E-11	7.957
an	1902	319	0.49	206.5	8.26	93.46	14.4	7.3	5.06E-10	2.40E-11	7.979
ao	1950	319	0.49	690.0	8.28	310.0	14.4	7.4	2.12E-10	7.45E-12	8.005
1a	2039	319	0.50	12	12	7200	14.5	7.2	9.51E-11	6.61E-13	8.039

Table 4. (Cont'd)

Test Period [1]	Test Time, h	Test Temp., °C	Load Ratio	Rise Time, s	Return Time, s	Hold Time, s	Kmax, MPa m$^{1/2}$	ΔK, MPa m$^{1/2}$	CGR in Env., m/s	CGR in Air m/s	Crack Length, mm
1b	2136	319	0.50	12	12	14400	14.6	7.3	9.47E-11	3.40E-13	8.072
1c	2350	319	1	-	-	-	14.7	-	9.00E-11	-	8.137
2a	2517	320	1	-	-	-	19.3	-	1.50E-10	-	8.241
2b	2542	320	0.50	12	12	14400	19.5	9.8	1.37E-09	8.97E-13	8.367
2c	2566	320	0.70	12	12	14400	19.6	5.9	5.64E-10	2.00E-13	8.428
2d	2580	320	0.70	12	12	7200	19.7	5.9	7.84E-10	4.09E-13	8.475
2e [4]	2585	321	0.70	12	12	14400	19.8	5.9	4.33E-10	2.05E-13	8.479
2f	2685.4	320	0.70	12	12	14400	19.9	6.0	3.50E-10	2.10E-13	8.576
3a	2694	320	0.70	12	12	7200	24.9	7.5	1.49E-09	8.76E-13	8.646
3b	2711.6	320	0.70	12	12	14400	25.0	7.5	6.51E-10	4.45E-13	8.685
3c	2855.7	320	1	-	-	-	25.3	0.1	2.70E-10	-	8.819
4a	2861.8	320	0.70	12	12	7200	30.6	9.2	4.93E-09	1.73E-12	8.989
4b	2879.5	320	1	-	-	-	31.6	-	2.98E-09	-	9.189
4c	2883.7	320	0.70	12	12	7200	32.4	9.7	7.27E-09	2.09E-12	9.347
4d	2887.8	320	1	-	-	-	32.5	-	2.21E-09	-	9.403
5	2952.8	320	1	-	-	-	19.6	-	8.68E-12	-	9.413
6 [5]	2993.7	320	1	-	-	-	28.9	-	1.97E-09	-	9.502
7	3023.4	320	1	-	-	-	19.8	-	1.36E-11	-	9.511
8	3032.1	320	1	-	-	-	30.9	-	3.98E-09	-	9.686
9 [f]	3055.1	320	1	-	-	-	37.7	-	5.32E-09	-	9.985
10	3071.7	320	1	-	-	-	23.8	-	5.17E-11	-	9.997

[1] Cyclic test periods are named in alphabetical order, and constant-load test periods are named in numerical order.

[2] The CGR was calculated between 1223 hr and 1268 hr. Friction force may have been changed after 1268 hr.

[3] The CGR was calculated between 1672 hr and 1702 hr.

[4] The AC heater failed after 5 hr. The test condition was repeated in the next test period, 2f.

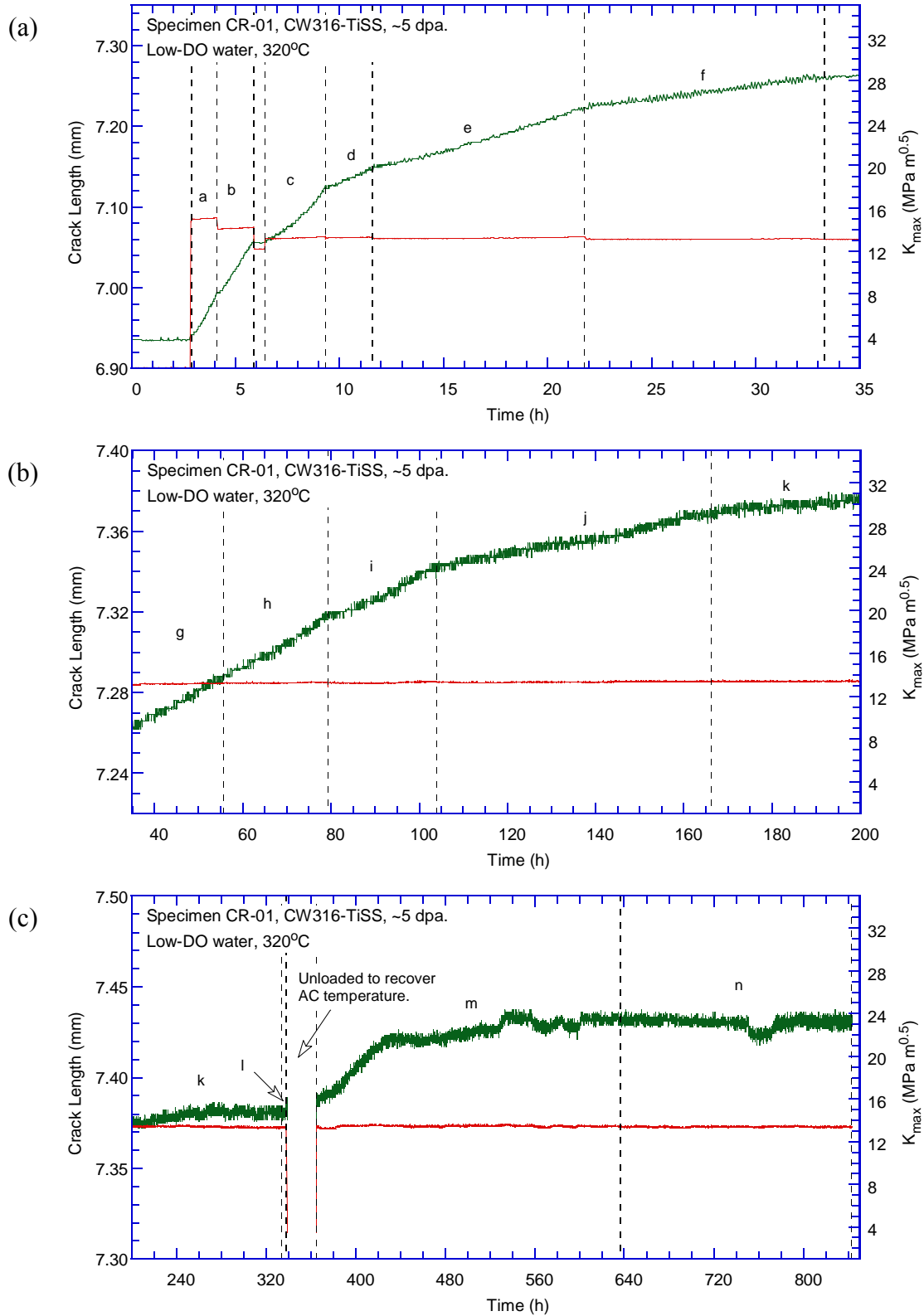[5] The CGR was calculated for the later part of the test period.

Figure 11. Crack-length-vs.-time plot for specimen CR-01 (~5-dpa CW 316-Ti SS) tested in low-DO high-purity water: test periods (a) a-f, (b) g-k, (c) k-n, (d) o-s, (e) t-y, (f) z-ac, (g) ad-ag, (h) ah-ao, (i) 1a-1c, (j) 2a-2f, (k) 3a-3c, (l) 4a-4c, (m) 5-8, and (n) 9-10.

Figure 11. (Cont'd)

(g)

Specimen CR-01, CW316-TiSS, ~5 dpa.
Low-DO water, 320°C

5.31E-10 m/s

ad   ae   af   ag

(h)

Specimen CR-01, CW316-TiSS, ~5 dpa.
Low-DO water, 320°C

ah   ai   aj   ak   al   am   an   ao

(i)

Specimen CR-01, CW316-TiSS, ~5 dpa.
Low-DO water, 320°C

1-a,
PPU, 2 hr

1-b
PPU, 4 hr

1-c,
constant-load

Figure 11. (Cont'd)

(j) Specimen CR-01, CW316-TiSS, ~5 dpa. Low-DO water, 320°C

(k) Specimen CR-01, CW316-TiSS, ~5 dpa. Low-DO water, 320°C
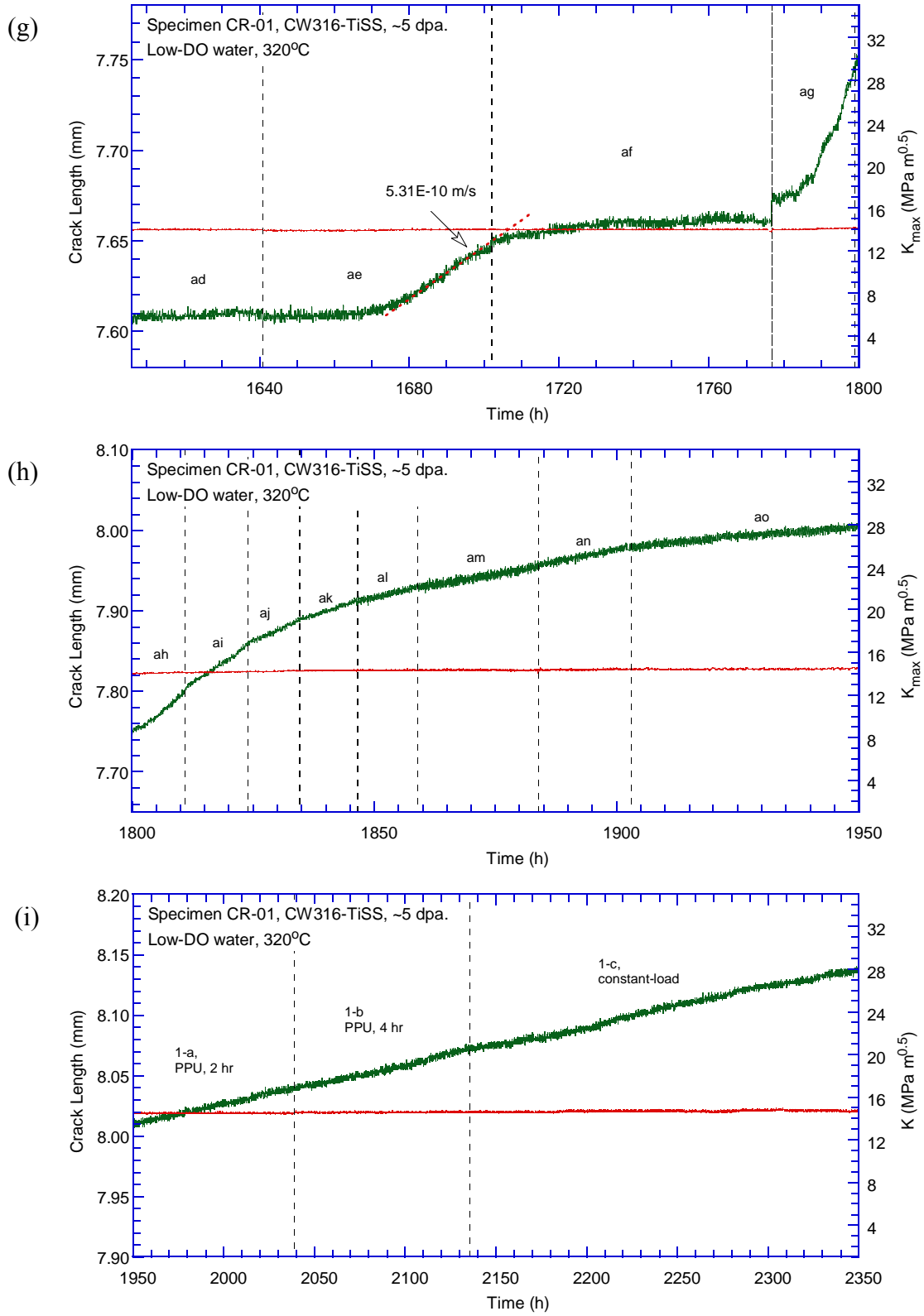
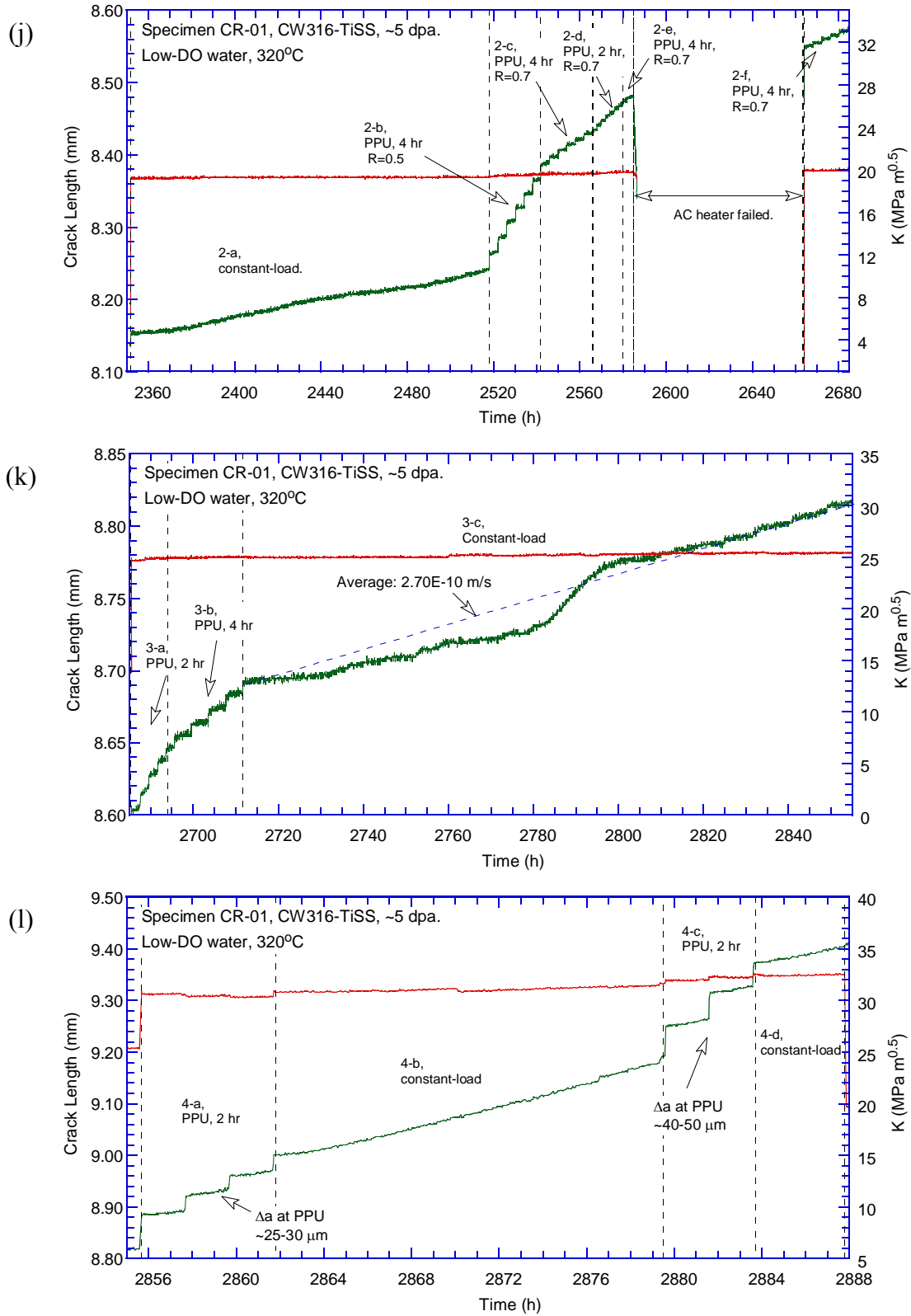(l) Specimen CR-01, CW316-TiSS, ~5 dpa. Low-DO water, 320°C
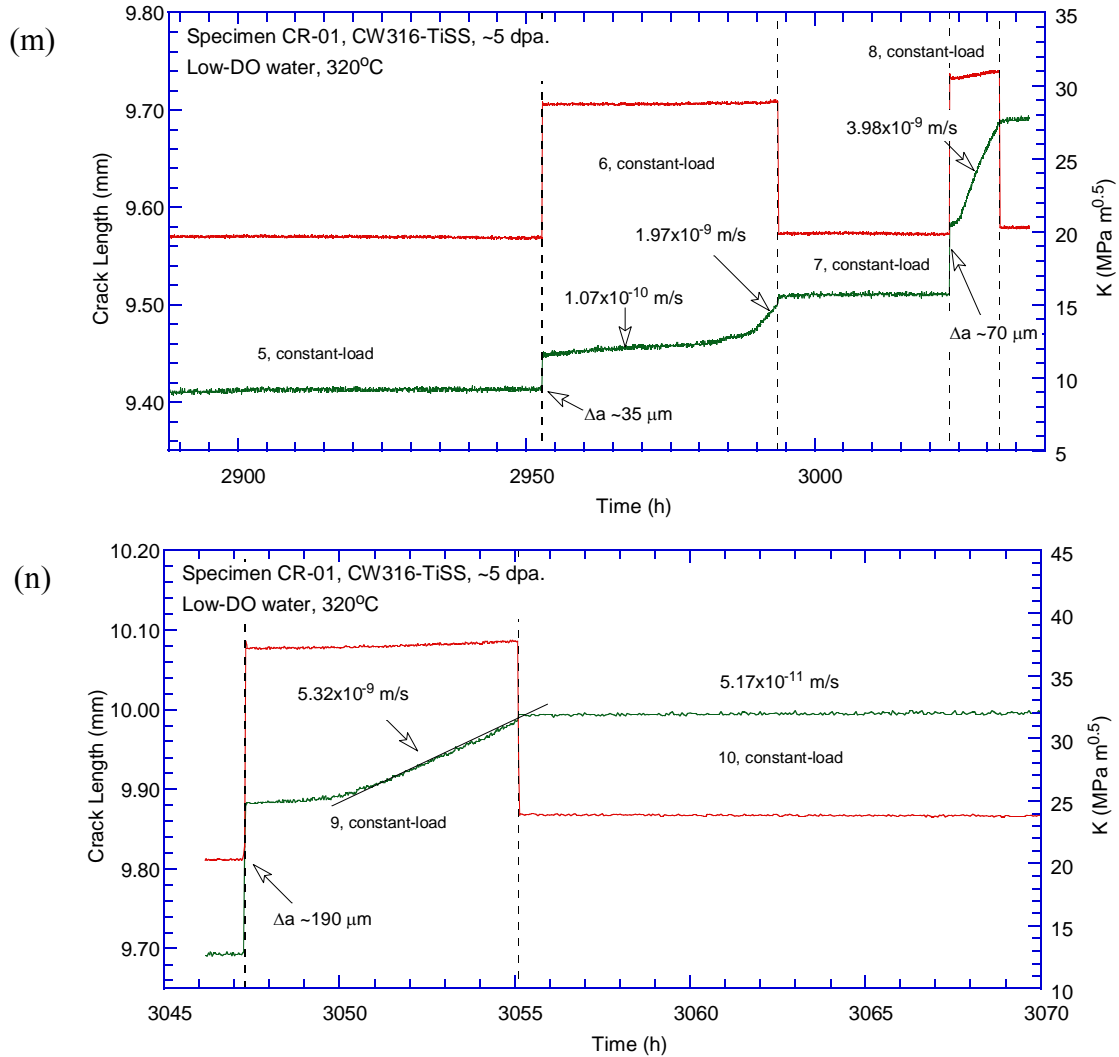
Figure 11. (Cont'd)

Figure 11. (Cont'd)

The cyclic CGRs obtained from specimen CR-01 are plotted in Fig. 12 as a function of fatigue CGRs in air. The CF curve developed by Shack and Kassner[27] for unirradiated SSs in high-purity water with 0.2 ppm DO is also included in the figure as a reference. While a large data scatter can be seen for this sample, the data trend indicates environmental enhancement. Many cyclic CGR data points are above the reference CF curve, suggesting a high cracking susceptibility of this sample.

The SCC CGRs obtained in this test are plotted in Fig. 13 as a function of stress intensity factor. All data points are above the NUREG-0313 curve regardless loading condition. The effect of PPU on the measured SCC CGRs can be seen at all stress levels except the lowest one ($\sim$15 MPa m$^{1/2}$). The SCC CGRs measured without PPU are significantly higher than the NUREG-0313 curve above $\sim$25 MPa m$^{1/2}$. The elevated SCC susceptibility of this sample is consistent with the observation of the cyclic CGR test, where corrosion fatigue resistance is also low. Compared with the CW 316 SS (Fig. 6) at the same dose, the CW 316-Ti SS seems to be highly susceptible to IASCC in a low-corrosion-potential environment.
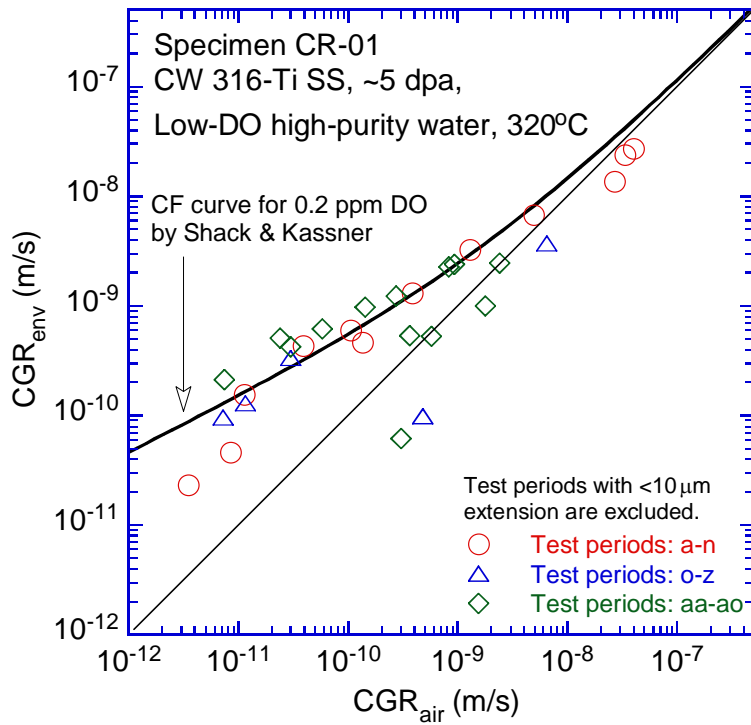
32

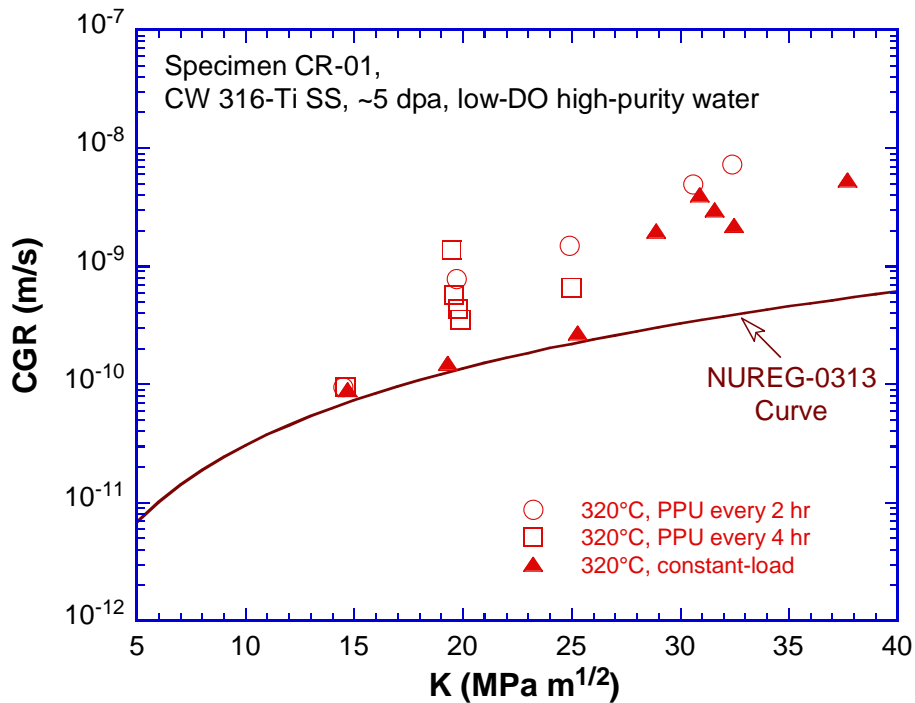Figure 12. Cyclic CGRs of specimen CR-01.

Figure 13. Constant-load CGRs of specimen CR-01.

Following the CGR test, a fracture toughness J-R curve test was performed on the sample in the test environment. Figure 14 shows the obtained J-R curve. A power-law fitting of the data gives

33

the relationship $J=41\Delta a^{0.31}$. The estimated J value is about 25 kJ/m^2 at the 0.2-mm offset line. The J-R curve data cannot be validated in accordance with the ASTM standard E1820 since the crack front did not pass the straightness requirements. The crack propagation was skewed toward one side of the specimen, and thus the variation in the crack extension exceeded 5% of the sample thickness. Also, there are less than the required five data points within the qualified region that is used for curve fitting.
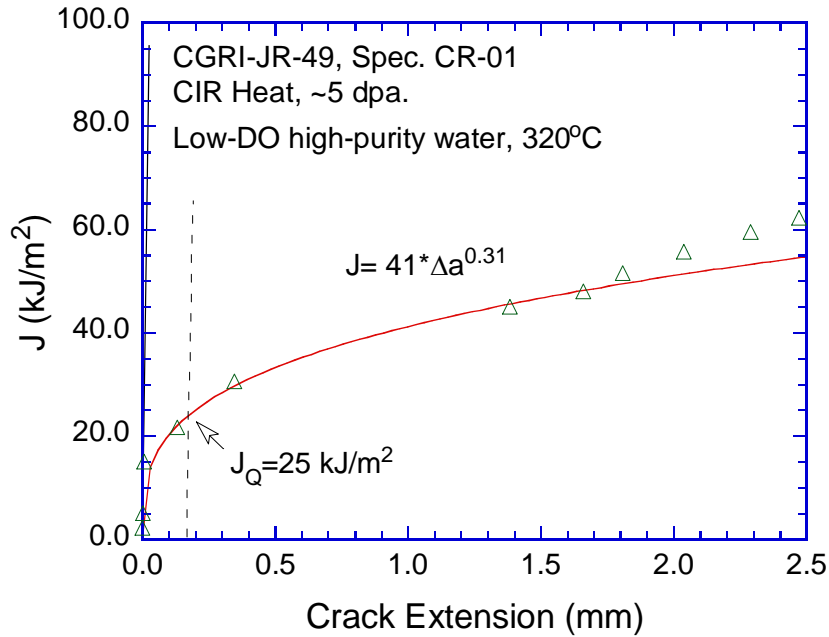

Figure 14. The J-R curve of specimen CR-01, CW 316-Ti SS at ~5 dpa.

Fractographic examination

After the J-R curve test, the specimen was fatigued in air at room temperature to break the remaining ligament. The specimen was then examined by SEM to characterize the fracture surface. Figure 15 shows the entire crack front in the specimen. The initial fracture morphology next to the machined notch was predominant TG cracking and the fracture surface appeared flat. Intergranular fracture quickly developed in this test, and the IG morphology covered the entire fracture surface of the SCC CGR region. Ductile dimples were the main fracture morphology evident in the J-R curve test. Elongated dimples and heavily deformed banded fracture were recognized on the J-R curve test region. The crack front was fairly straight for the SCC test, indicating a well-controlled loading condition. The final crack front of the J-R curve test, however, was skewed toward one side of the specimen (Fig. 15). This nonuniform crack extension of the J-R curve test affected the validation of the test result.

The transitions from TG to IG fracture and from IG to dimple fracture can be better viewed in Fig. 16 along the central line of the sample. In addition to IG cracking, very few mixed-mode cracking areas can be seen on the fracture surface at the end of CGR test. Figure 17 show the

details of the two areas noted *a* and *b* in Fig. 16. While IG cracking was extensive throughout the entire SCC CGR test, more secondary cracks (Fig. 17b) developed in the later part of the CGR test, where stress intensity factors were higher. Following the CGR test, the elongated dimples and banded fracture morphology were clearly evident in the J-R curve test, as shown in Fig. 18. Along with dimples, a few inclusions or secondary particles can also be seen on the fracture surface. Also, the final crack length was measured on the SEM image, and all crack extensions reported above have been corrected with the SEM measurements.
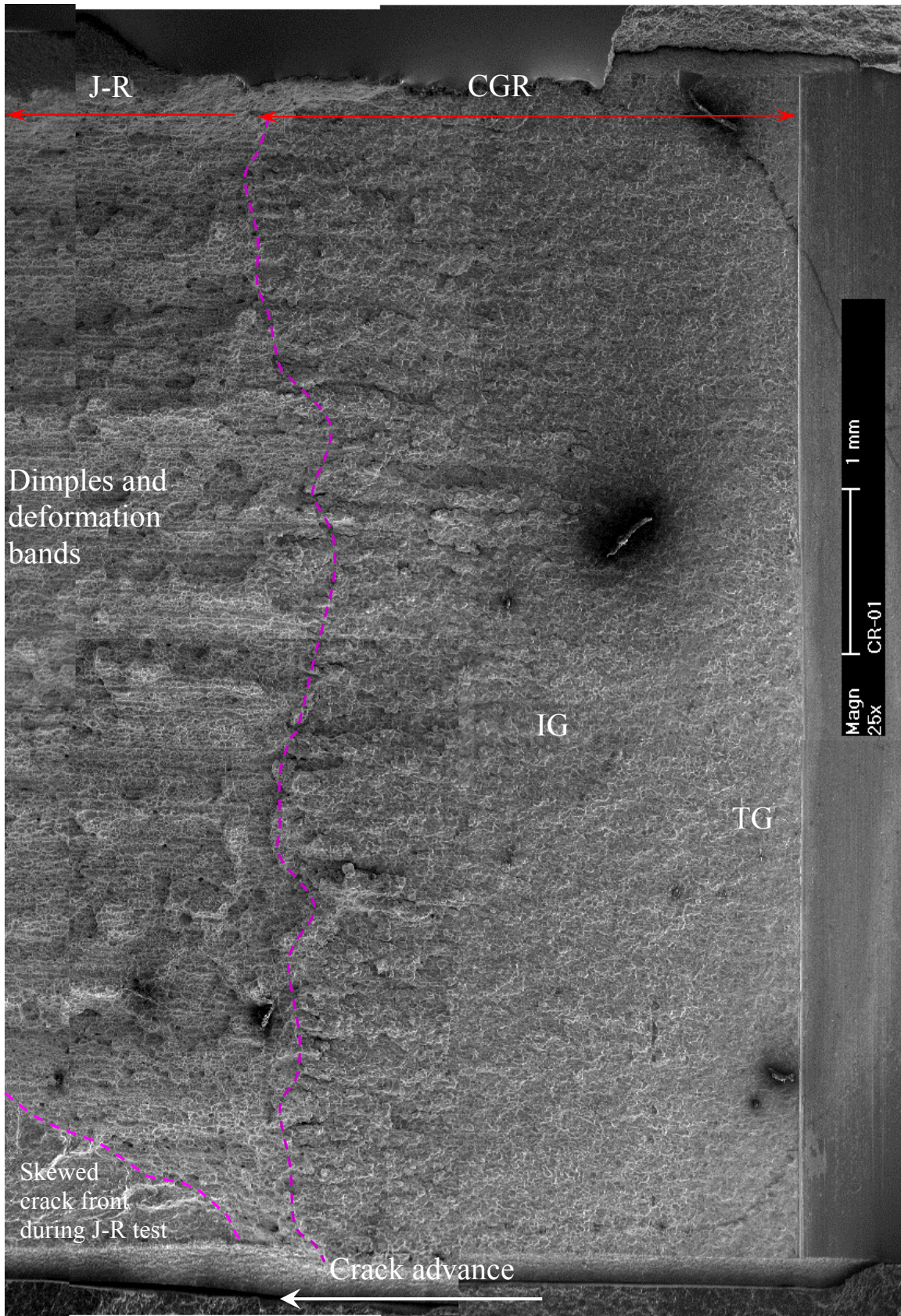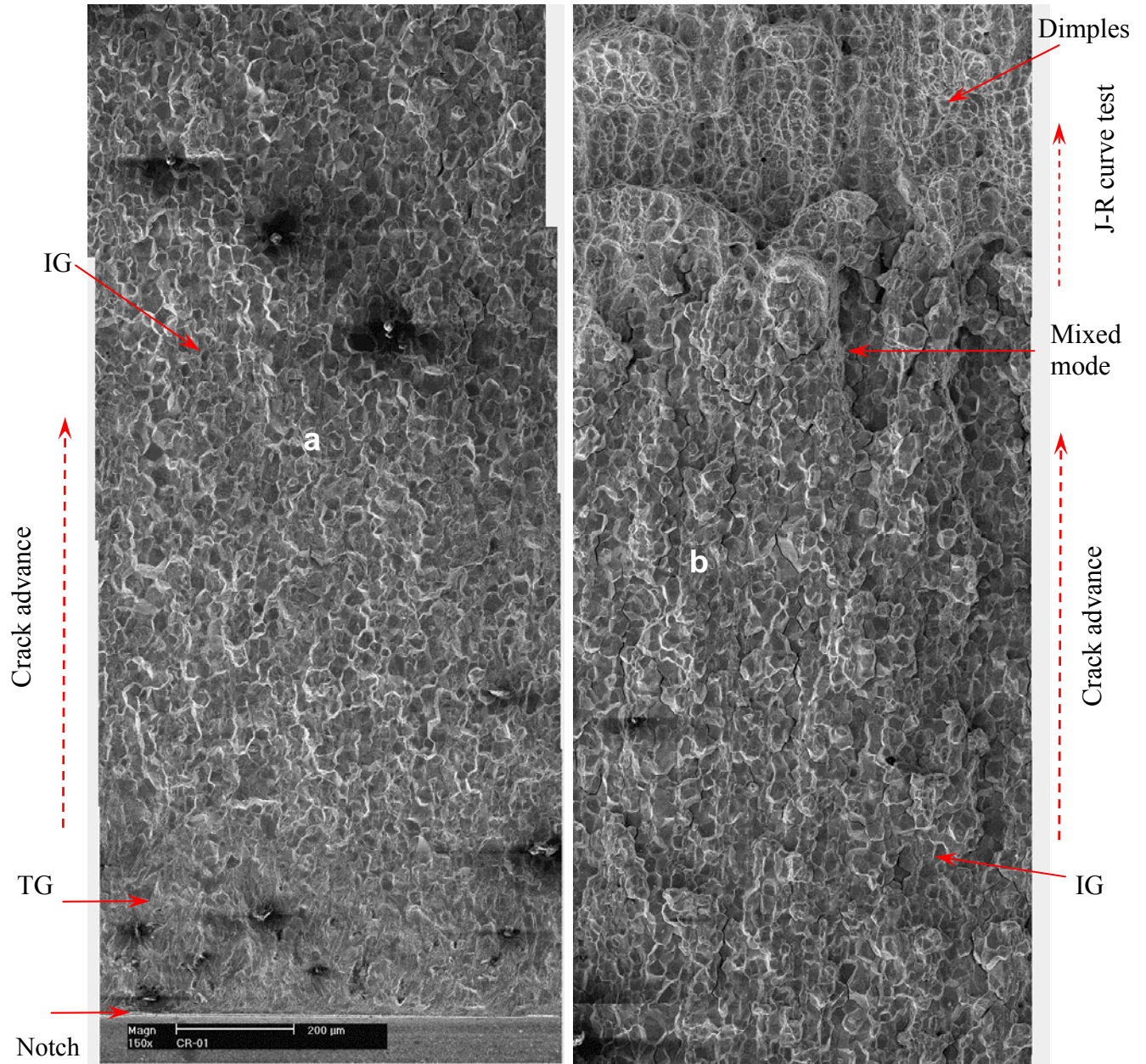
Figure 15. Fracture surface of specimen CR-01 tested in low-DO high-purity water.

(a) Central line, 1/2   (b) Central line, 2/2

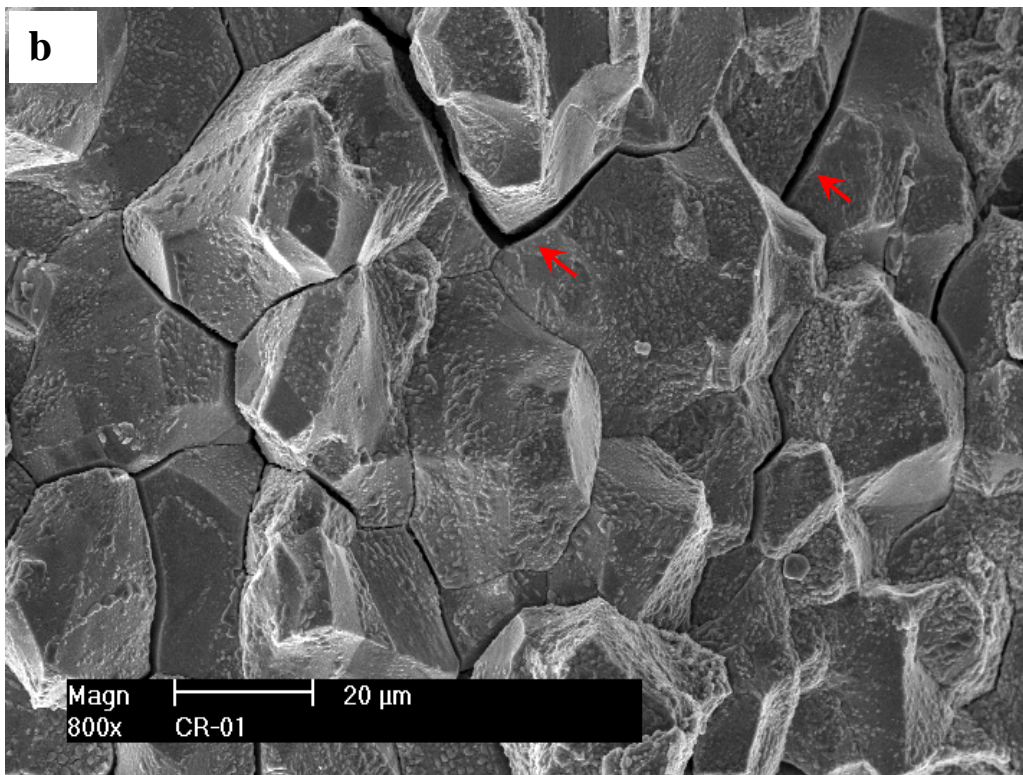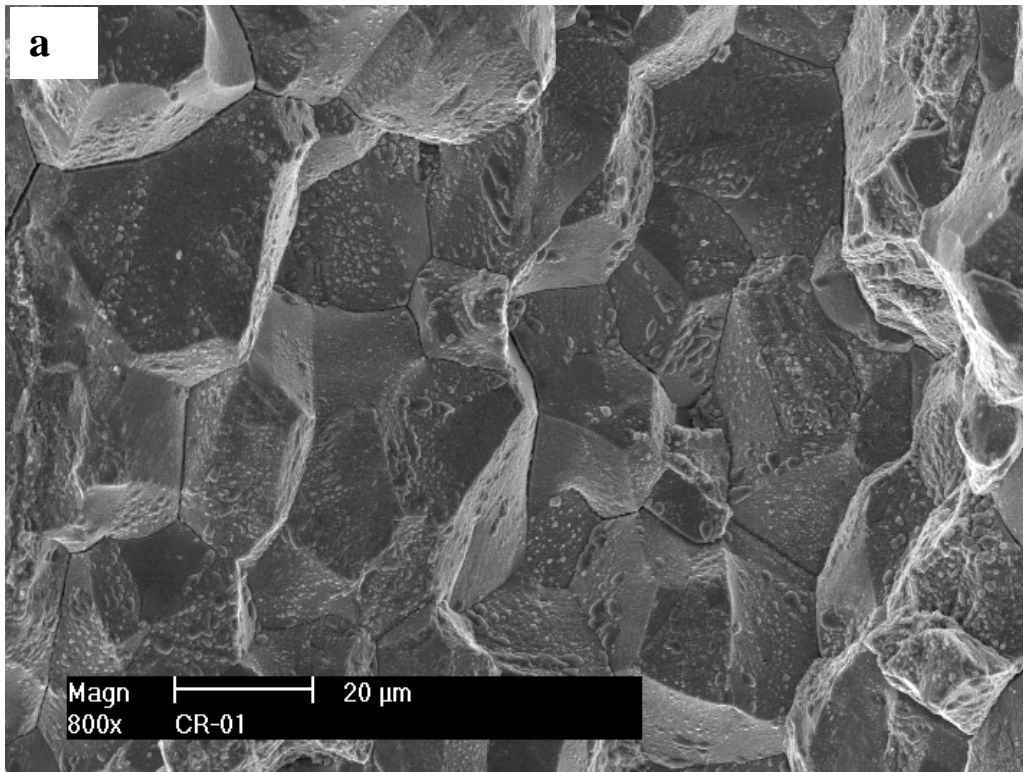Figure 16. Fracture surface of specimen CR-01 along the sample central line.

Figure 17. Intergranular cracking and secondary cracks (red arrows) during the constant-load CGR test of specimen CR-01 (*a* and *b* correspond to the areas noted in Fig. 16).
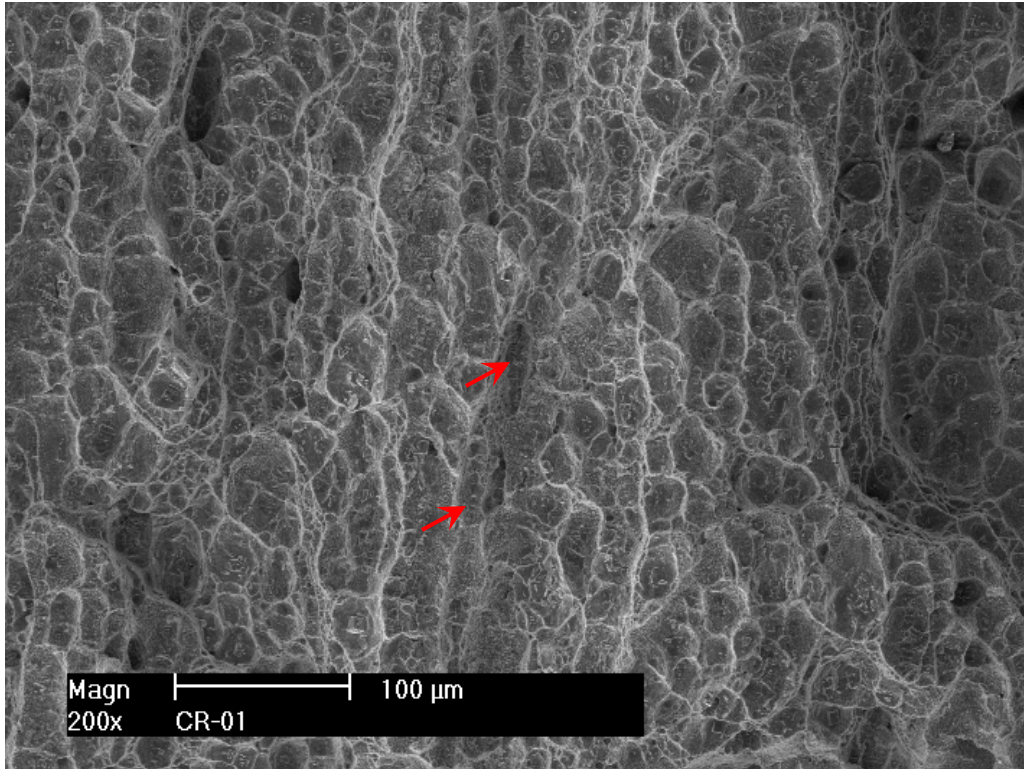
Figure 18. Elongated dimples (red arrows) and banded fracture during the J-R curve test of specimen CR-01.

3.2.2 Cold-worked 316-Ti SS at ~8 dpa

CGR and J-R curve tests

The second Ti-stabilized CW 316 SS specimen (CR-04) was irradiated to ~8 dpa and tested in a simulated PWR water environment. Prior to the test, the sample was soaked in the test environment at ~320°C for 8 days to stabilize environmental variables. The test conditions and CGR results for this specimen are summarized Table 5. The crack-length history plots of this test are shown in Fig. 19.

The cyclic loading of the test was started at a relatively low K_{max} of ~12 MPa m$^{1/2}$ with a triangular waveform of R=0.2 and 2 Hz (test period *a*). The resulting CGR was significantly lower than the fatigue growth rate in air, suggesting an inadequate load level for pre-cracking. After a short test to check the machine compliance, the K_{max} was increased to ~14 MPa m$^{1/2}$ and ~15 MPa m$^{1/2}$ in test periods *b* and *c*, respectively. A CGR close to the fatigue rate was obtained in the later part of test period *c*.

Following the crack initiation, the load ratio was increased gradually to 0.45, while the K_{max} was lowered to ~12 MPa m$^{1/2}$ from test periods *d* to *g*. The cyclic frequency was also increased gradually during these test periods. The measured CGRs were all above the fatigue line and

decreased slowly with increasing load ratio. After lowering the K_{max} to ~11 MPa m$^{1/2}$ in test period *h*, the CGR was far below the fatigue line, indicating a limit of K_{max} for stable cracking. The K_{max} was thus increased back to ~12 MPa m$^{1/2}$ in the next test period (*i*) to re-establish the previous cracking rate. In the following test periods (*j-o*), the K_{max} was maintained at ~12 MPa m$^{1/2}$, and the load ratio was increased slightly to 0.5. Meanwhile, the rise time was increased gradually to 300 s. Environmentally enhanced cracking was evident in test periods *n* and *o*. With further increases in the rise time from 300 to 1000 s, the environmental CGR was nearly unchanged from test periods *o* to *q*, indicating an established environmental effect on cyclic crack growth.

The test was set to a constant load in test period *1a* at ~12.3 MPa m$^{1/2}$ (Fig. 19d). A CGR of 1.6 x 10^{-10} m/s was recorded over 45-µm crack extension. To investigate the effect of unloading, PPU was applied with R=0.5 in the following test periods, *1b* and *1c*, with 1- and 2-hr hold times, respectively. While no "stair step" crack growth is apparent from the crack length vs. time curve, the measured CGRs with PPU were significantly higher than those without PPU. The CGR in test period *1b* (1-hr hold time) is about a factor of two higher than that of test period *1c* (2-hr hold time). It is clear that PPU has a significant effect on the measured CGR for this sample. Also, the effect of PPU seems to be proportional to the frequency of unloading.

In the next test period (*2a*), the load was increased to ~17 MPa m$^{1/2}$. A growth rate of 1.1 x 10^{-9} m/s was measured over ~77-µm crack extension under a constant-load condition (approximately constant K by load shedding). To evaluate the effect of dynamic loading, PPU with R=0.5 was applied every 1 hour in the next test period, *2b*. A sudden increase in crack length, about ~15-20 µm, was observed at every unloading-reloading cycle (see Fig. 19e), while the growth rate was relatively low during the one-hour hold time. With this stair-step cracking behavior, the magnitude of unstable crack extension and the frequency of PPU would dominate the average CGR measured in the test period. The influence of unloading ratio and hold time was evaluated at this stress intensity factor in test periods *2c* and *2d*. With R=0.8, the effect of PPU was much weaker, and the measured CGRs were 1.5 x 10^{-9} m/s and 1.4 x 10^{-9} m/s for test periods *2c* (1-hr hold) and *2d* (2-hr hold), respectively.

After the load was briefly held at a low stress intensity level, the influence of unloading-reloading rates on the stair-step cracking behavior was evaluated in test period *2f*. With the same magnitude of unloading (R=0.5), three unloading-reloading times, 12, 120, and 1000 s, were tested. While the rate of unloading-reloading varied by three orders of magnitude, the sudden jumps in crack length were all similar (20-30 µm) in the sub-test periods (Fig. 19f). The test was then continued at a constant load of ~17.9 MPa m$^{1/2}$ (test period *2g*). A CGR of 1.2 x 10^{-9} m/s was obtained over 64-µm crack extension. This growth rate was consistent with that measured in test period *2a*. After this confirmation of loading condition, the effect of load ratio on the stair-step crack growth behavior was further investigated at R=0.7 and R=0.9 in test period *2h*. The stair-step growth was more evident with the lower load ratio. A longer holding time (4 hr) was also tested in the next test period (*2i*) with R=0.8. Comparing the test periods *2c*, *2d* and *2i*, the unstable crack extension (the height of stair step, and too small to be seen in test period *2c* and *2d* in Fig. 19e) seemed to increase with hold time at the same load ratio. Following the test period *2i*, the sample was prepared for CGR tests at lower temperatures. The load was lowered

and held at a constant K, about ~5 MPa m$^{1/2}$, to prepare for CGR tests at different temperatures. Even at such a low stress intensity factor, an initial fast CGR was observed but gradually decreased with time (see the inset in Fig. 19f). An average growth rate of 4.8 x 10^{-11} m/s was registered over 28-μm crack extension in this test period.

The CGR test at ~290°C was started with a constant load at 18.8 MPa m$^{1/2}$ (test period *3a*). The measured CGR was ~8.0 x 10^{-10} m/s with 130-μm crack extension. Then, PPU (R=0.8) was introduced with 1-hr hold time (test period *3b*). Again, a stair-step growth behavior was observed with an average step height of 8 μm. During this test period, the actuator of the test system was unexpectedly tripped due to escalating temperature at the hydraulic pump. The actuator crosshead was held at a constant position. After an initial slow decline, the load on the sample was maintained at ~17.3 MPa m$^{1/2}$ over the following 20 hr. During this time, the crack continued to grow at a rate of 6.0 x 10^{-10} m/s in test period *3c* for ~43 μm. Upon the recovery of the hydraulic pump, the actuator was switched on, and a crack extension of 250 μm was recorded in the DCPD measurement. The load on the sample was decreased to <5 MPa m$^{1/2}$ to prepare for a CGR measurement at ~270°C. When the load was increased back to ~20 MPa m$^{1/2}$, another sudden jump in crack length (>220 μm) was recorded on the DCPD measurement. Following the re-load, the stress intensity factor was held at a constant with and without PPU in test periods *4b* to *4d*. It appeared that the crack growth had been stalled, and much lower CGRs were recorded. A decision was made to re-activate the crack growth with cyclic loading.

In the following test periods, the sample was loaded in cyclic mode at K$_{max}$ of 20.7 MPa m$^{1/2}$ and load ratio of 0.5-0.6. The rise time was increased from 300 s to 1000 s between test periods *r* and *v*. Environmentally enhanced cracking was observed initially, but disappeared quickly with the increase of rise time. The test was set to a constant load after ~80-μm crack extension. No crack extension was observed for over 40 hr, suggesting a stalled SCC crack. The crack tip appears to have been over-strained by the re-start of the hydraulic pump. A decision was made to continue the CGR test at a higher stress intensity factor.

Between test periods *w* and *aa*, K$_{max}$ was increased to ~25-28 MPa m$^{1/2}$ with load ratios of 0.3-0.5. An elevated CGR was recorded for the first 6-7 hr and then started to decline. Although the measured CGRs were higher than the fatigue growth rates in air, the environmental enhancement was significantly lower than that previously observed. The precracking was restarted at a higher K$_{max}$. Between test periods *ab* and *aj* (Fig. 19i), environmental enhanced cracking was re-established successfully at ~33 MPa m$^{1/2}$. After about 360-μm crack extension, the load ratio and rise time were then gradually increased to induce an environmental effect. The test was set to a constant load at 33.5 MPa m$^{1/2}$ without PPU (test period *6a*). A CGR of 4.6x10^{-10} m/s was obtained over ~40-μm crack extension at ~270°C. Next, PPU was applied every 2 hr and 1 hr for test periods *6b* and *6c*, respectively. While no stair-step growth behavior was observed in the crack-length history plot (Fig. 19j), the measured CGRs with PPU (*6b* and *6c*) were slightly higher than that without PPU (*6a*).

Next, the autoclave temperature was increased to prepare for repeating the CGR test at ~290°C. After 20 hr, the autoclave temperature was stabilized, and the CGR test was resumed at

~35 MPa m$^{1/2}$. First, the PPU was applied every 1 hr and 2 hr in test periods *7a* and *7b*, respectively. The measured CGRs were very similar (~1.3 x 10^{-10} m/s) in these test periods over a total of 120-μm crack extension. After the PPU was removed in test period *7c*, a slightly lower CGR, 1.2 x 10^{-10} m/s, was obtained over 72-μm crack extension.

The load was then lowered to prepare for increasing the autoclave temperature again to ~320°C. After the temperature stabilized, the CGR test was first conducted with PPU at ~36 MPa m$^{1/2}$ (test period *8a*). Stair-step growth was observed, and the average step height was about 12 μm. When the PPU was removed, a CGR of 4.9 x 10^{-10} m/s was measured in test period *8b* over ~240-μm crack extension. Note that the applied stress intensity factor increased slightly in this test period due to the rapid crack growth (Fig. 19l).

The last CGR test period was carried out at a stress intensity factor of ~46 MPa m$^{1/2}$. This was above the maximum stress intensity factor for a plane-strain constraint of the sample (~44 MPa m$^{1/2}$). Upon the re-loading of the sample, the jump in crack length was about 95 μm. The initial CGR was fairly low but gradually increased after several hours. A CGR of 1.0 x 10^{-8} m/s was finally stabilized over 380-μm crack extension. Again, due to the rapid crack growth, the stress intensity factor increased slowly during this test period.

Table 5. Crack growth rate test on ~8-dpa CW 316-Ti SS (specimen CR-04) in PWR water.

Test Period [1]	Test Time, h	Test Temp., °C	R Load Ratio	Rise Time, s	Return Time, s	Hold Time, s	Kmax, MPa m$^{1/2}$	ΔK, MPa m$^{1/2}$	CGR in Env., m/s	CGR in Air m/s	Crack Length, mm
Start	0.92										6.936
a	2.78	320	0.21	0.22	0.22	0.03	12.0	9.5	5.75E-09	3.80E-08	6.955
b	5.04	320	0.20	0.23	0.23	0.02	14.2	11.3	3.68E-08	6.66E-08	7.048
c	6.5	320	0.20	0.23	0.23	0.02	15.6	12.5	1.01E-07	9.02E-08	7.253
d	7.5	320	0.30	0.22	0.22	0.03	14.7	10.3	9.82E-08	5.53E-08	7.410
e	9.2	320	0.35	0.44	0.44	0.06	13.8	9.0	4.85E-08	1.89E-08	7.534
f	12.4	320	0.40	0.43	0.43	0.07	13.0	7.8	3.68E-08	1.30E-08	7.712
g [2]	23.2	319	0.45	2.09	2.09	0.41	12.0	6.6	7.57E-09	1.62E-09	7.820
h	27.8	319	0.52	2.00	2.00	0.50	10.8	5.2	3.90E-10	8.22E-10	7.823
i	34.5	319	0.45	4.17	4.17	0.83	12.0	6.6	3.99E-09	8.12E-10	7.863
j	48.9	319	0.50	8.21	4.11	1.79	12.1	6.1	1.69E-09	3.24E-10	7.911
k	62.4	319	0.50	16.41	4.10	3.59	12.1	6.1	7.99E-10	1.62E-10	7.939
l	79.3	319	0.50	24.60	9.84	5.40	12.1	6.1	6.55E-10	1.09E-10	7.960
m	105.4	319	0.50	49.17	9.83	10.83	12.1	6.1	2.59E-10	5.46E-11	7.978
n	168.3	318	0.50	98.31	9.83	21.69	12.1	6.1	1.57E-10	2.76E-11	8.005
o	217	319	0.50	245.7	9.83	54.34	12.2	6.1	1.77E-10	1.11E-11	8.029
p	250.2	319	0.50	491.1	9.82	108.9	12.3	6.1	2.18E-10	5.62E-12	8.050
q	273.5	319	0.50	818.3	9.82	181.7	12.3	6.1	2.16E-10	3.39E-12	8.066
1a	342.4	319	1.00	-	-	-	12.3	-	1.64E-10	-	8.111
1b	351.6	319	0.50	12	12	3600	12.4	6.2	7.45E-10	7.88E-13	8.138
1c	369.9	319	0.50	12	12	7200	12.4	6.2	3.93E-10	3.99E-13	8.164
2a	385.7	319	1.00	-	-	-	17.1	-	1.07E-09	-	8.241
2b	391.2	319	0.50	12	12	3600	17.3	8.6	5.37E-09	2.38E-12	8.359
2c	398.5	319	0.80	12	12	3600	17.4	3.5	1.54E-09	1.89E-13	8.404
2d	410.6	319	0.80	12	12	7200	17.6	3.5	1.44E-09	9.73E-14	8.469
2e [3]	411.7	319	1.00	-	-	-	7.3	-	1.32E-09	-	8.482

Table 5. (Cont'd)

Test Period [1]	Test Time, h	Test Temp., °C	R Load Ratio	Rise Time, s	Return Time, s	Hold Time, s	Kmax, MPa m$^{1/2}$	ΔK, MPa m$^{1/2}$	CGR in Env., m/s	CGR in Air, m/s	Crack Length, mm
2f-1	413.8	319	0.50	12	12	3600	17.6	8.8	5.60E-09	2.53E-12	8.530
2f-2	415.9	319	0.50	120	120	3600	17.7	8.9	6.21E-09	2.51E-12	8.591
2f-3	419	318	0.50	1000	1000	3600	17.8	8.9	5.82E-09	2.08E-12	8.653
2g	433.8	319	1.00	-	-	-	17.9	-	1.18E-09	-	8.717
2h-1	438.4	319	0.70	12	12	3600	18.2	5.5	4.73E-09	6.18E-13	8.805
2h-2	447.7	318	0.90	12	12	3600	18.2	1.8	1.12E-09	6.51E-14	8.852
2i	459.2	318	0.80	12	12	14400	18.4	3.7	1.95E-09	5.64E-14	8.934
2j [3]	482.9	318	1.00	-	-	-	5.0	-	4.81E-11	-	8.962
3a	529.7	289	1.00	-	-	-	18.8	-	7.97E-10	-	9.094
3b	534.8	289	0.80	12	12	3600	19.0	3.8	3.90E-09	2.37E-13	9.173
3c [4]	556.8	289	1.00	-	-	-	17.3	-	5.99E-10	-	9.216
Cooling											
4a [3]	578	270	1.00	-	-	-	5.1	-	2.14E-10	-	9.478
4b	602.6	271	1.00	-	-	-	20.6	-	7.65E-11	-	9.877
4c	610.8	271	0.80	12	12	3600	20.7	4.1	3.90E-10	3.02E-13	9.899
4d	674.1	271	1.00	-	-	-	20.6	-	8.73E-12	-	9.901
r	677.4	271	0.60	239.9	9.60	60.1	20.7	8.3	2.62E-09	3.11E-11	9.926
s [2]	699	271	0.60	479.6	9.59	120.4	20.7	8.4	3.53E-10	1.59E-11	9.957
t	745.9	271	0.60	798.6	9.58	201.4	20.7	8.3	6.36E-11	9.45E-12	9.965
u	770.7	271	0.50	415.9	9.98	84.1	20.8	10.4	1.39E-10	3.47E-11	9.976
v	799.7	271	0.50	832.5	9.99	167.5	20.9	10.5	4.47E-11	1.77E-11	9.979
5	841.5	271	1.00	-	-	-	20.9	-	negligible	-	9.982
w	851.2	271	0.41	262.1	10.48	37.91	25.1	14.7	8.10E-10	1.57E-10	10.007
x	865.6	271	0.41	524.0	10.48	75.95	25.1	14.7	1.52E-10	7.85E-11	10.012
Load tripped											
y [2]	890.7	271	0.50	215.4	10.34	34.63	26.7	13.4	3.01E-10	1.52E-10	10.047
z	892 - 894.7	271	0.35	4.48	4.48	0.52	26.9	17.5	4.06E-09	1.53E-08	10.075
aa	898.9	271	0.30	1.81	1.81	0.19	28.4	19.9	2.64E-09	5.44E-08	10.096
ab	913-916.6	271	0.30	0.91	0.91	0.09	30.7	21.5	5.61E-09	1.40E-07	10.132
ac [2]	920	268	0.40	1.80	1.80	0.20	32.1	19.3	2.42E-08	5.45E-08	10.211
ad	921.8	268	0.45	4.46	4.46	0.54	32.2	17.8	2.01E-08	1.79E-08	10.267
ae	923.2	268	0.50	13.24	4.41	1.76	32.3	16.2	1.01E-08	4.67E-09	10.300
af	926.5	268	0.55	26.13	4.35	3.87	32.7	14.8	6.19E-09	1.83E-09	10.357
ag	937.7	268	0.60	102.8	10.28	17.23	33.0	13.3	1.97E-09	3.42E-10	10.419
ah	945.3	268	0.65	209.6	10.06	40.36	32.9	11.7	9.15E-10	1.13E-10	10.440
ai	964.5	268	0.65	419.2	10.06	80.82	33.1	11.8	5.83E-10	5.80E-11	10.473
aj	990.9	268	0.70	816.1	9.79	183.9	33.2	10.1	2.57E-10	1.89E-11	10.493
6a [2]	1019.3	268	1.00	-	-	-	33.5	-	4.62E-10	-	10.534
6b	1033.5	268	0.70	12	12	7200	33.7	10.1	6.11E-10	2.13E-12	10.567
6c	1042.7	268	0.70	12	12	3600	33.9	10.2	7.71E-10	4.33E-12	10.594
7a	1066.6	286	0.70	12	12	3600	34.3	10.3	1.26E-09	4.67E-12	10.644
7b	1081.4	287	0.70	12	12	7200	34.8	10.4	1.29E-09	2.47E-12	10.711
7c	1097.5	287	1.00	-	-	-	35.1	-	1.17E-09	-	10.783
8a	1119.2	319	0.70	12	12	3600	36.1	10.8	6.16E-09	6.01E-12	10.947
8b	1132.8	319	1.00	-	-	-	37.7	-	4.88E-09	-	11.184
9 [2]	1143.2	319	1.00	-	-	-	46.3	-	1.03E-08	-	11.563
Complete											

[1] Cyclic test periods are named in alphabetical order, and constant-load test periods are named in numerical order.

[2] The CGR at the end of the test period is reported.

[3] Lower the load to minimize crack growth prior to changing test conditions.

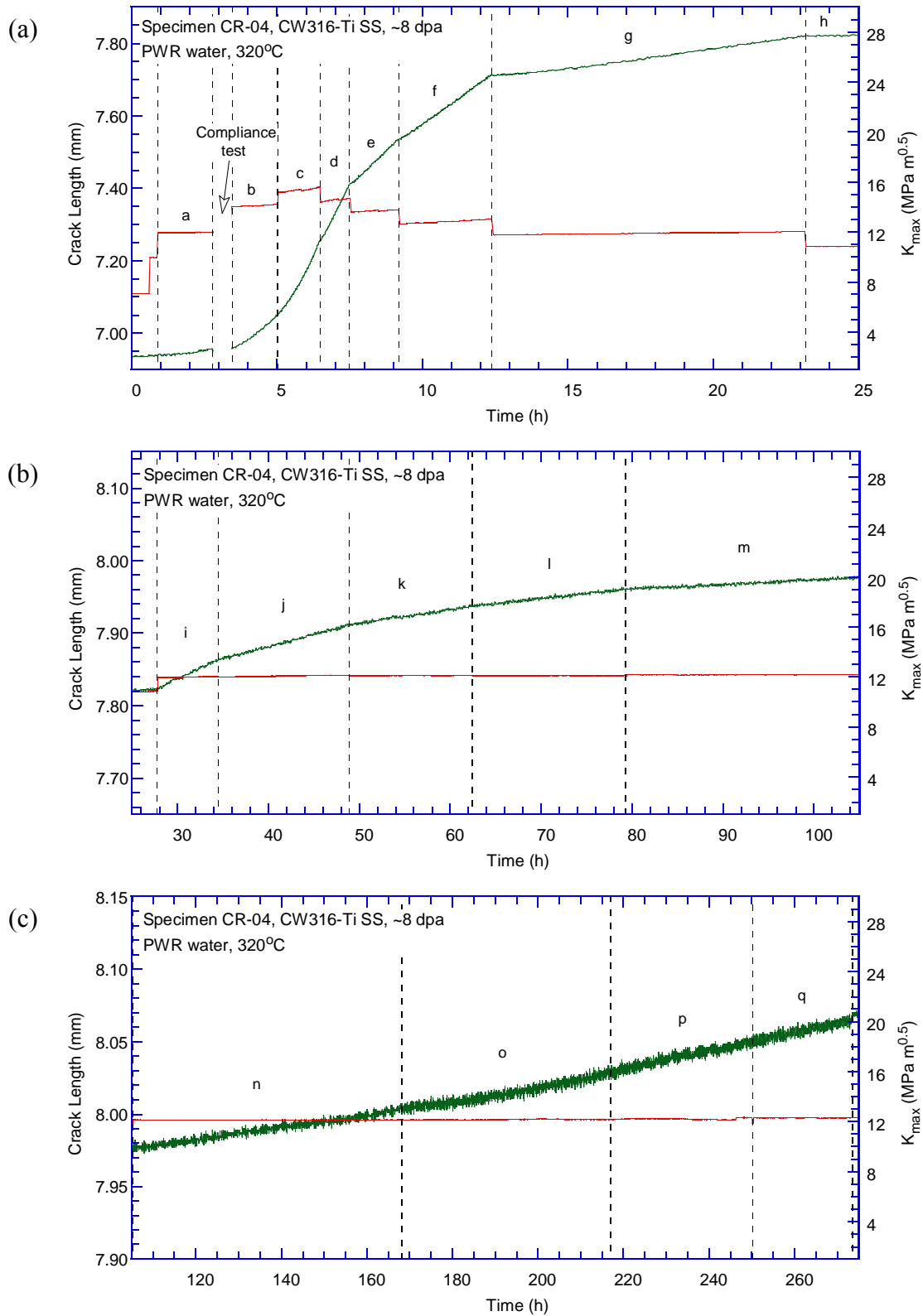[4] Actuator off; load was approximately constant.

Figure 19. Crack-length-vs.-time plot for specimen CR-04 (~8-dpa CW 316-Ti SS) tested in PWR environment: test periods (a) a-h, (b) i-m, (c) n-q, (d) 1a-1c, (e) 2a-2d, (f) 2e-2j, (g) 3a-3c, (h) 4a-4d, (i) r-5, (j) aa-aj, (k) 6a-6c, (l) 7a-7c, and (m) 8a-9.
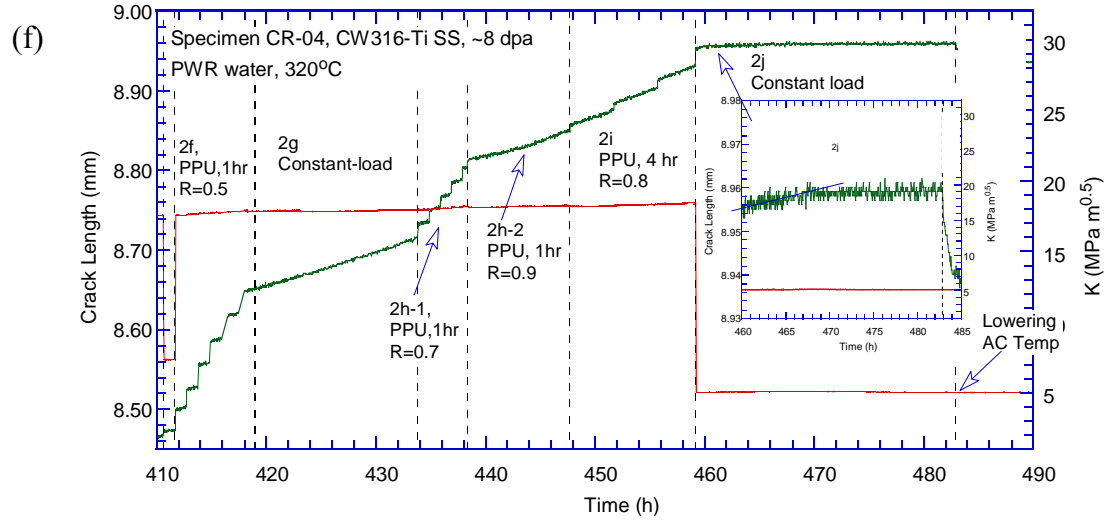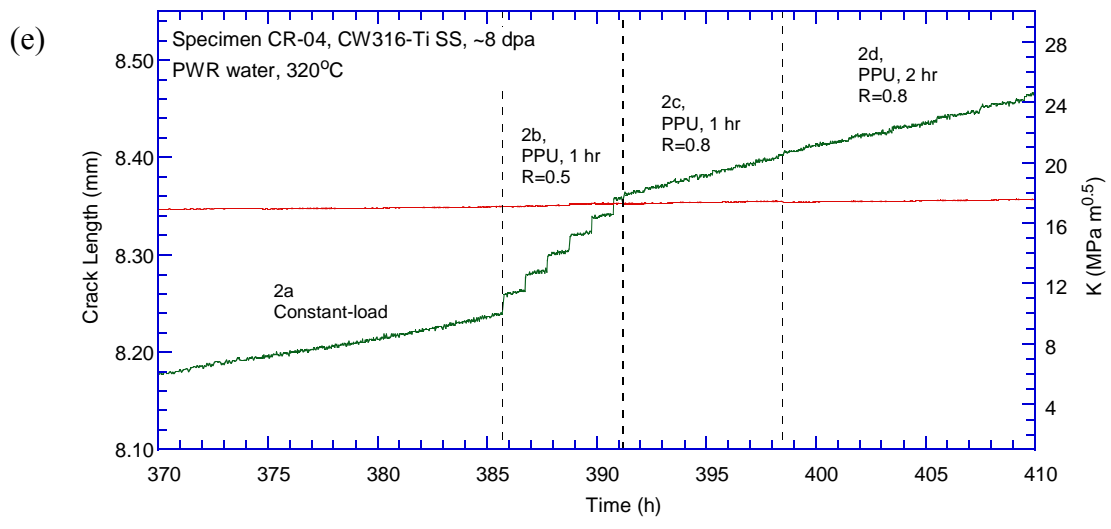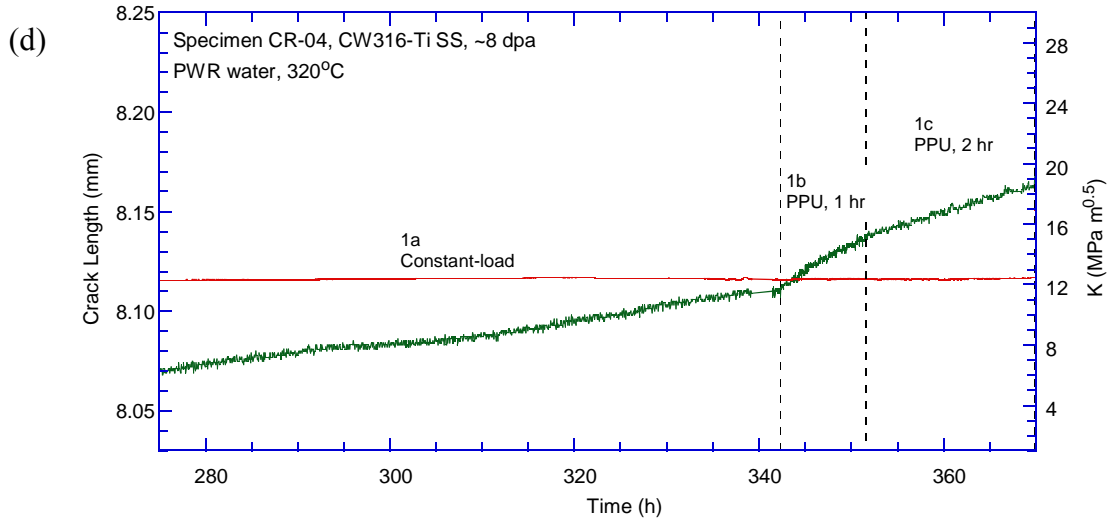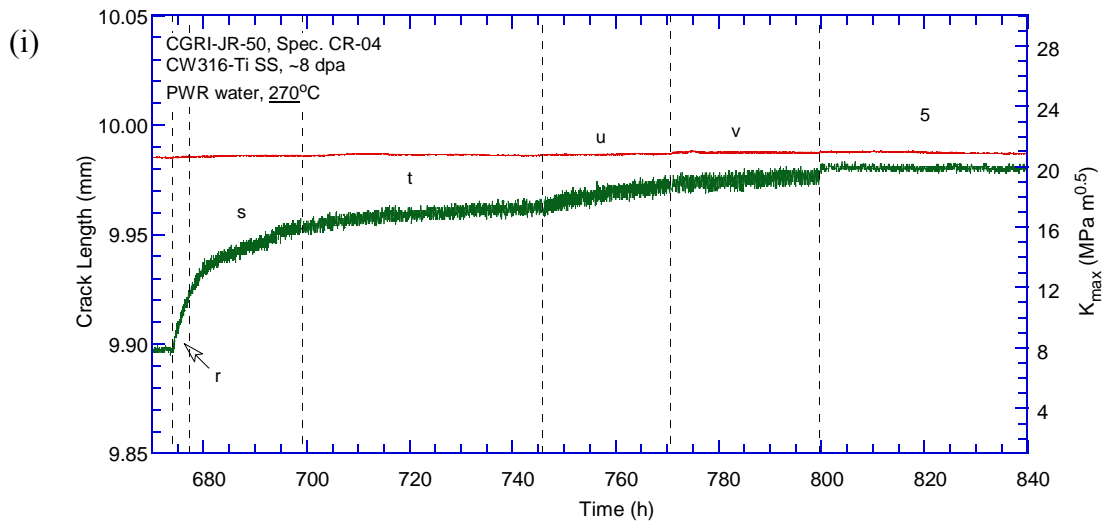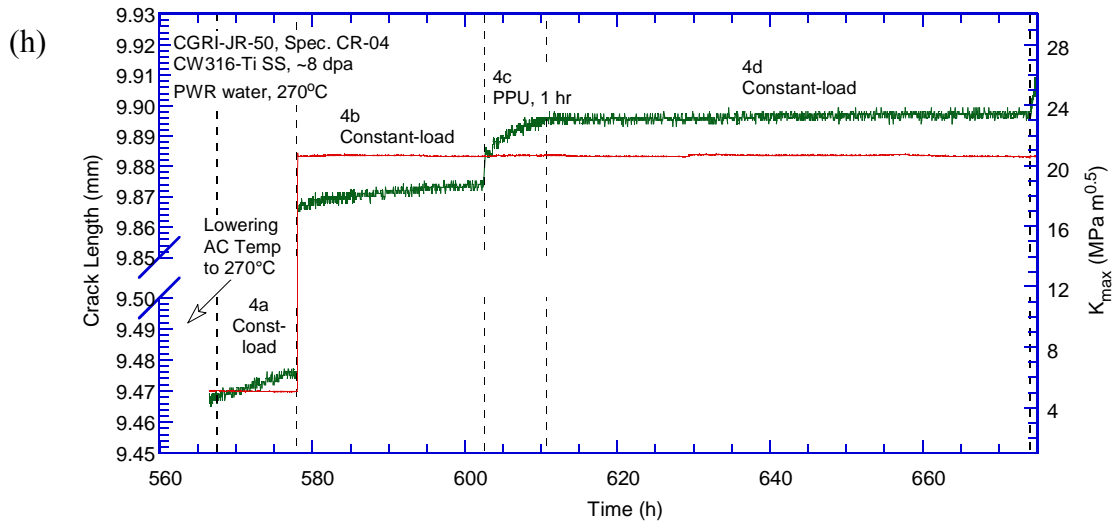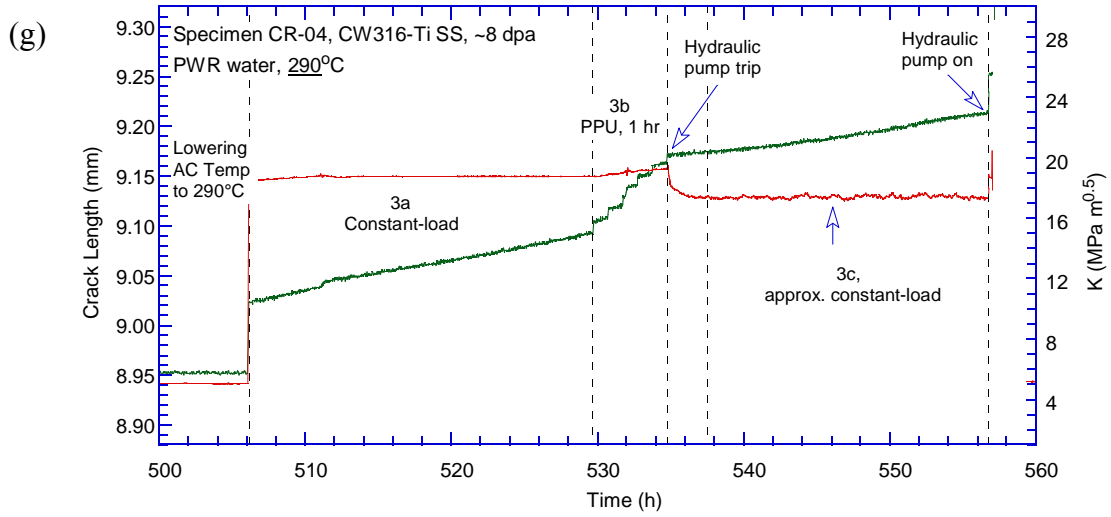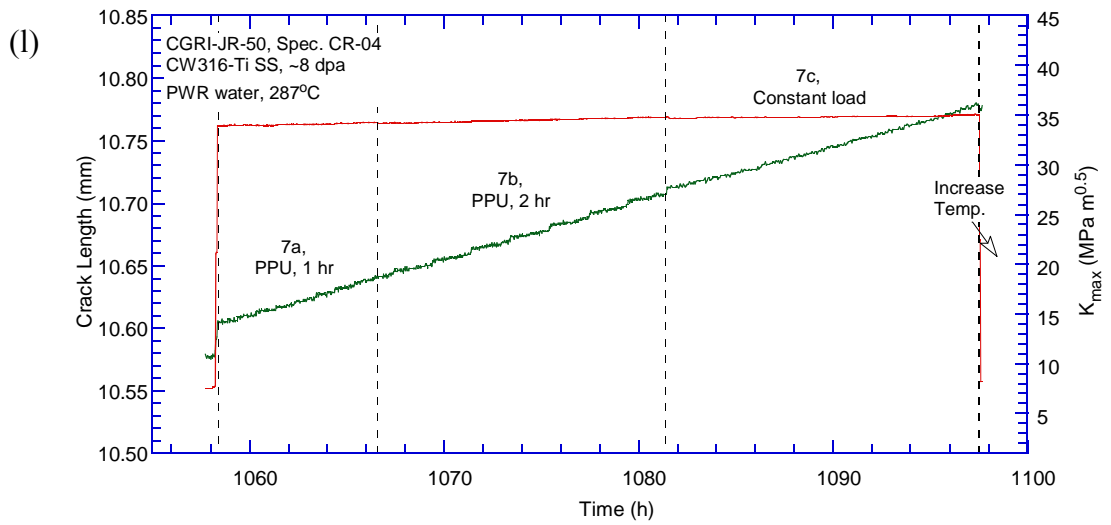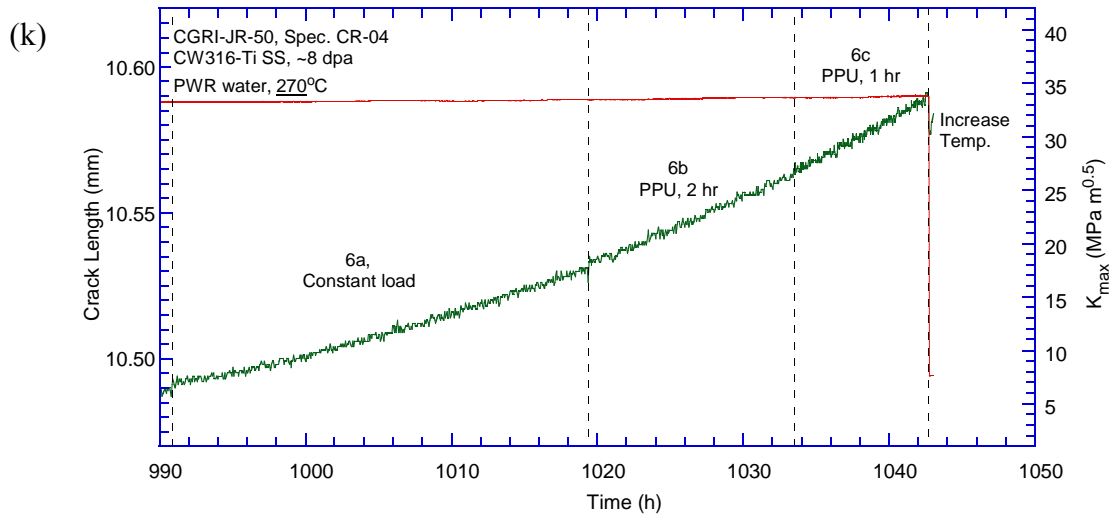
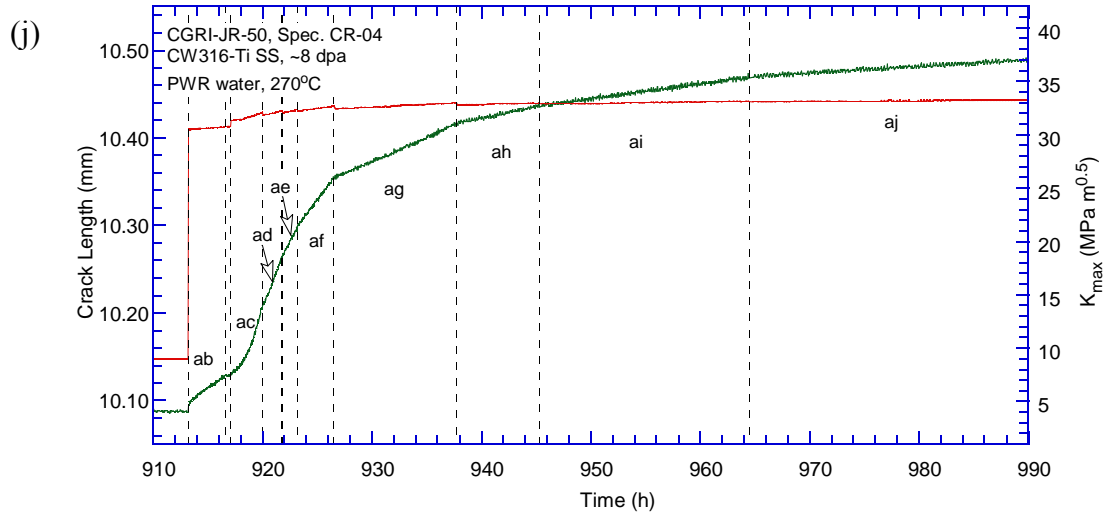Figure 19. (Cont'd.)

Figure 19. (Cont'd.)
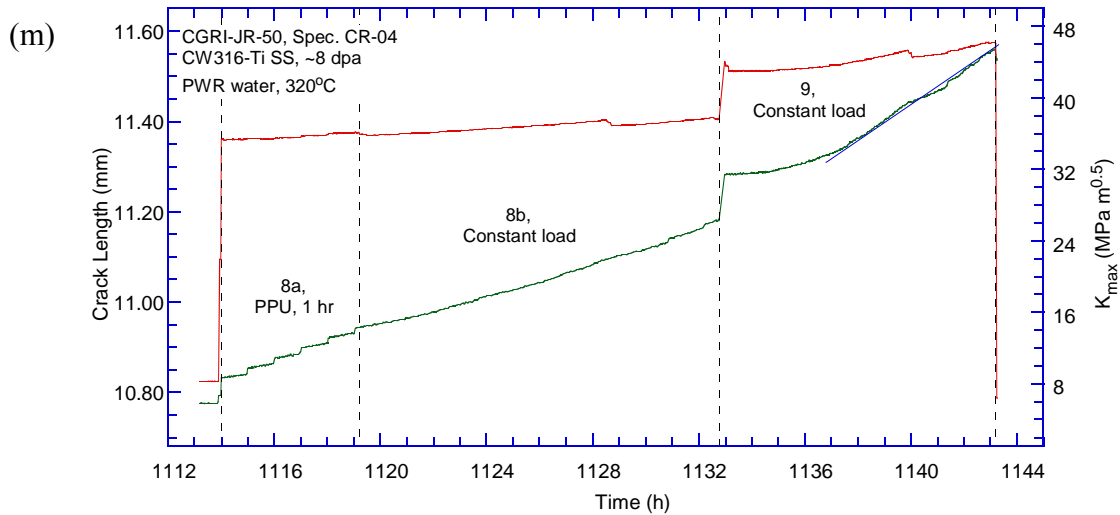
Figure 19. (Cont'd.)

(m)

Figure 19. (Cont'd)

All cyclic CGRs obtained from specimen CR-04 are plotted in Fig. 20 as a function of fatigue CGRs in air. The CF curve developed by Shack and Kassner[27] for unirradiated SSs in low-DO high-purity water (0.2 ppm DO) is also included in the figure as a reference. Environmental enhancement is evident in this irradiated sample, and the cyclic cracking behavior is similar at 270 and 320°C. Most of the cyclic CGRs measured on this sample are above the reference CF curve, suggesting an elevated cracking susceptibility. Compared with the same material irradiated to ~5 dpa (Fig. 12), the environmental effect in this sample seems stronger, implying a deteriorating CF behavior with increasing dose.

The SCC CGRs measured at ~320°C are plotted in Fig. 21 as a function of stress intensity factor. All data points are above the NUREG-0313 curve regardless of loading condition. The effect of PPU on the measured SCC CGRs is evident at several stress intensity factors. The elevated SCC susceptibility of this sample is consistent with that observed at ~5 dpa for the same material tested in low-DO high-purity water. Clearly, this material (CW 316-Ti) is highly susceptible to SCC after irradiation in low-corrosion-potential environments.

The temperature dependence of SCC CGRs for this material is shown in Fig. 22. Between 270 and 320°C, the constant-load CGRs without PPU display Arrhenius type behavior, which yields an activation energy of 110 kJ/mol.
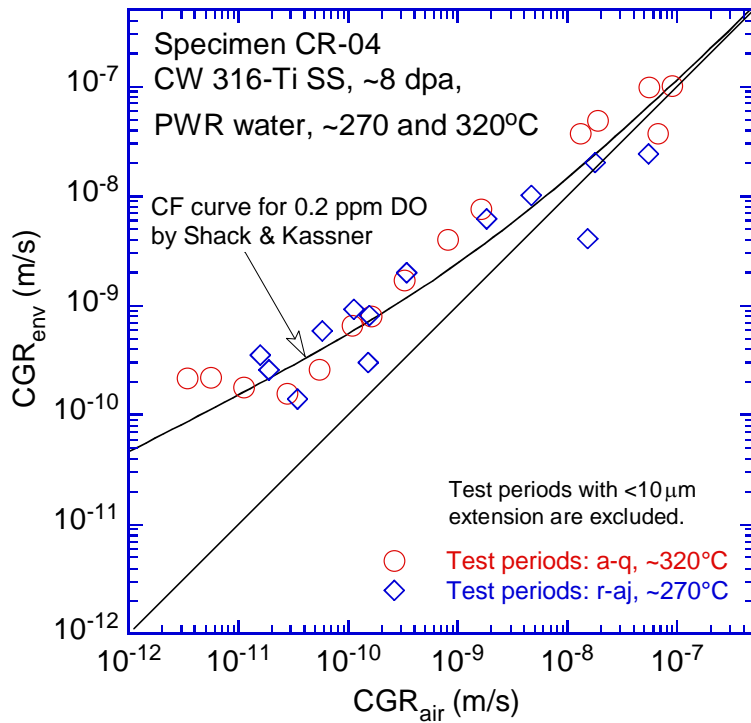
48

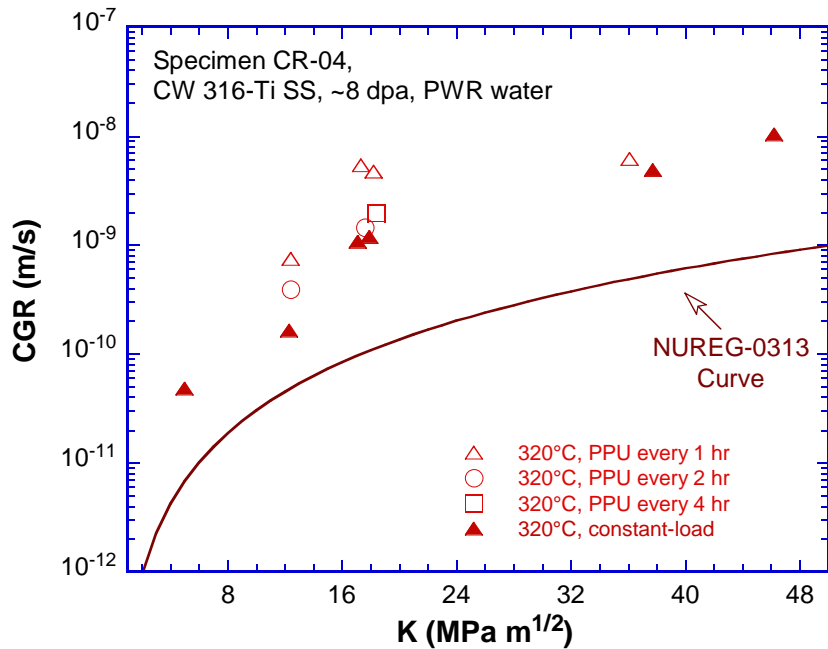Figure 20. Cyclic CGRs of specimen CR-04, a CW 316-Ti SS irradiated to ~8 dpa and tested in PWR water.

Figure 21. Constant-load CGRs of specimen CR-04 at ~320°C.

Following the CGR test, a J-R test was performed on the specimen in PWR water at 320°C. The sample was loaded at a constant extension rate of 0.43 μm/s while the load and load-line

49

displacement were recorded. A significant load drop was observed during the test, indicating severe irradiation embrittlement. The obtained J-R curve is shown in Fig. 23. A power-law curve fitting of the data gives the relationship $J=30.5\Delta a^{0.11}$. The estimated J value at the 0.2-mm offset line is about 26 kJ/m^2. Since there are less than five qualified data points within the measurement limits can be used for curve fitting, this J-R curve test cannot be validated for J_{IC} according to ASTM E1820.
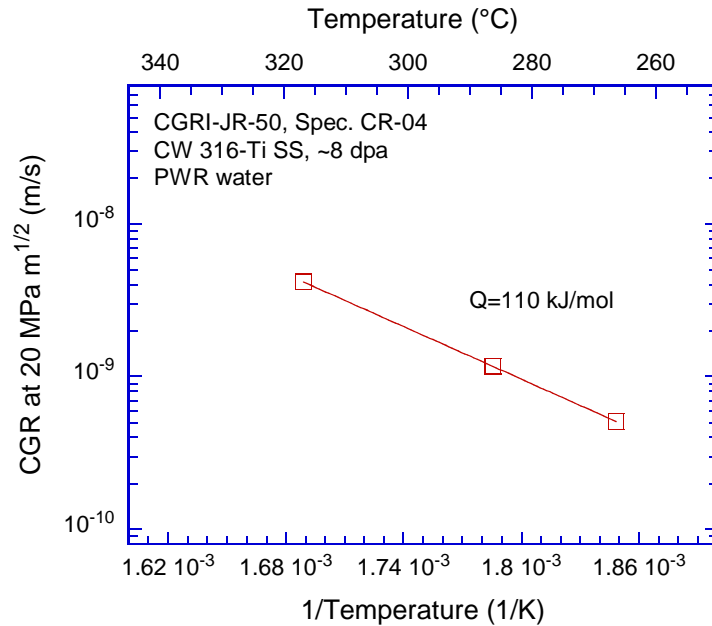

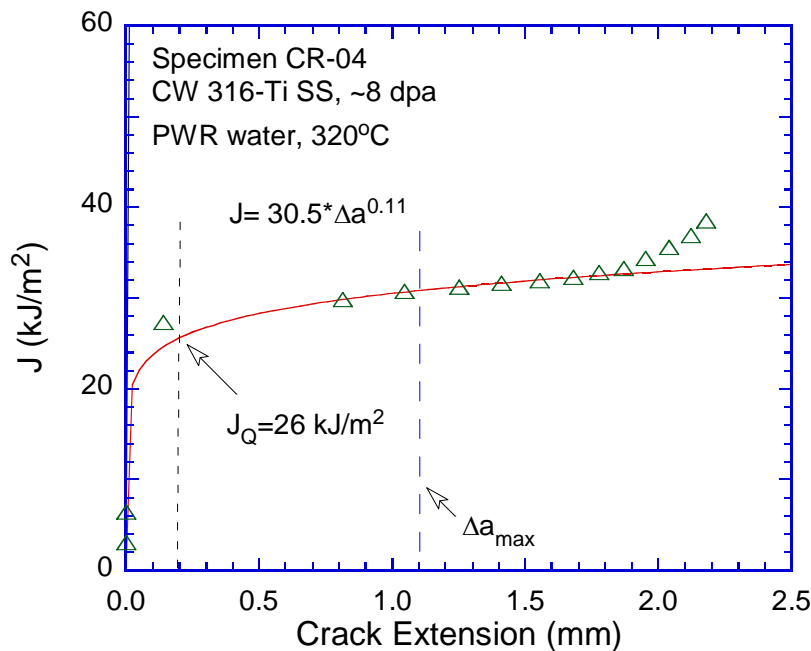Figure 22. Temperature dependence of specimen CR-04.

Figure 23. The J-R curve test with specimen CR-04 in PWR water at 320°C.

Fractographic examination

After the specimen was broken in air at room temperature, it was examined by SEM. Figure 24 shows the entire CGR test region and the initial portion of the J-R test. The crack front is fairly straight for the CGR test, indicating a well-controlled loading condition during the test. Five distinct areas can be identified on the fracture surface at this magnification. An initial flat TG area can be seen next to the machined notch. Then, an area of IG cracking covers the fracture surface before the trip of the actuator. The second flat area with TG morphology on the fracture surface is attributed to the cyclic-loading test periods to re-activate the crack. Next, the IG morphology with increasing secondary cracking dominates the remaining fracture surface of the CGR test. Finally, the fracture mode changes to ductile dimples in the J-R curve test region. The final crack length is measured on the SEM image, and all crack extensions reported above have been corrected with the SEM measurements. Since there are two cyclic test regions (test periods *a-q* and test periods *r-aj*) with an IG area in between, an independent verification of the linear correction of DCPD measurement is possible in this test. While the crack extension at the start of the second cyclic CGR region is measured about 2.9 mm on the SEM image, the corrected DCPD measurement shows a crack extension of 2.965 mm at the beginning of the test period *r*. The error resulting from the linear correction is less than 3% at this crack extension.

The different stages of the test are also shown in Fig. 25 along the central line of the sample. In the J-R test region, elongated deformation bands can also be seen along with the dimples. Details of the marked areas a - d in Fig. 25 are shown in Fig. 26. Transgranular cracking with cleavage-like morphology is evident during the cyclic-loading test periods (Figs. 26a and 26c). While IG cracking was extensive throughout the entire SCC CGR test period, more secondary cracks developed in the later part of the CGR test, where the stress intensity factors were higher (Fig. 26b vs. Fig. 26d). The SEM image after the CGR test (Fig. 27) indicates elongated dimples and banded fracture morphology in the J-R curve test. Inclusions can be occasionally seen in the elongated dimples.
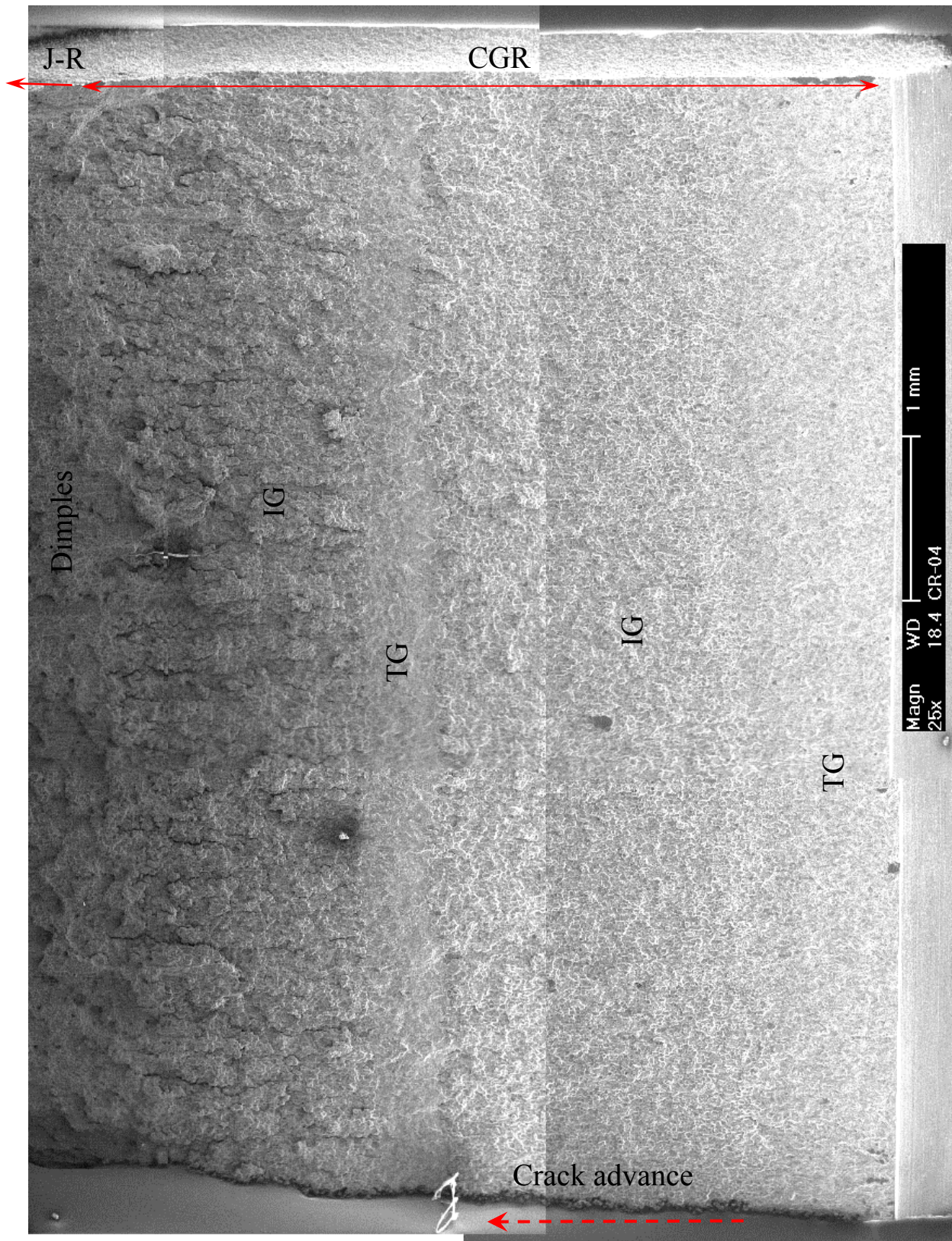
Figure 24. Fracture surface of specimen CR-04 tested in PWR water.
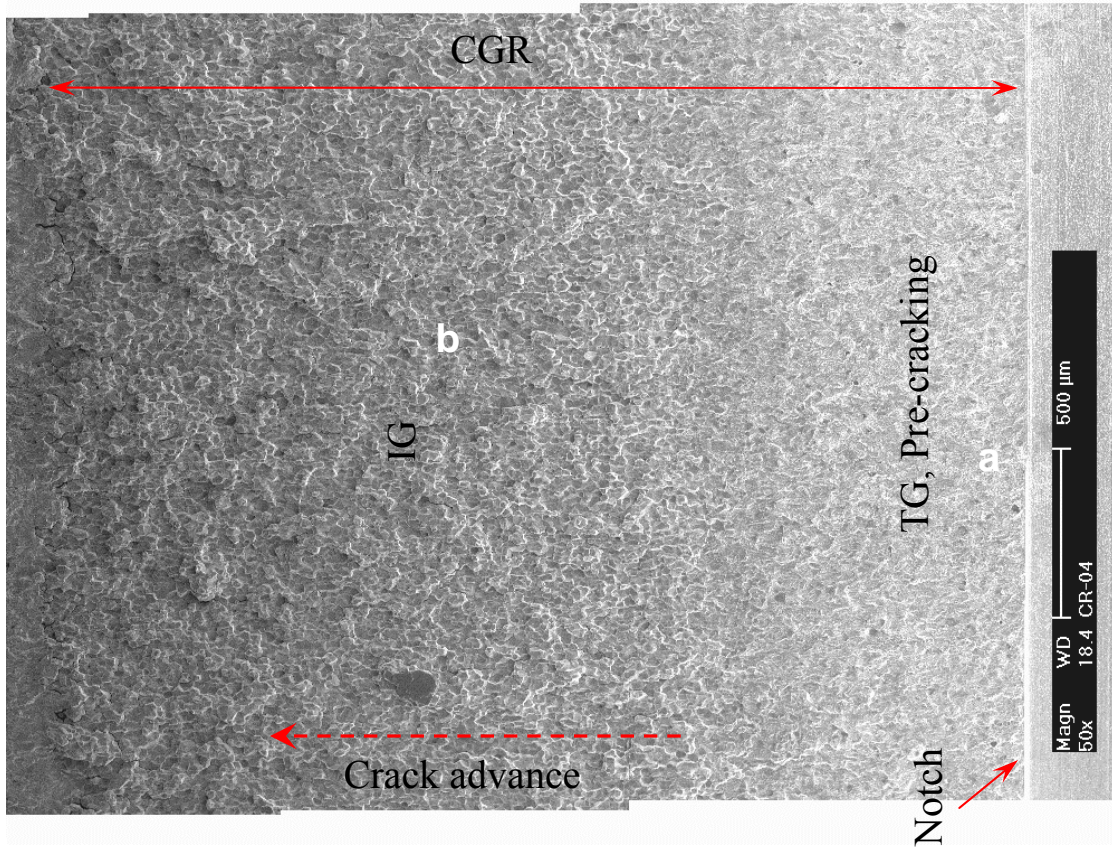
(a) Central line, 1/2
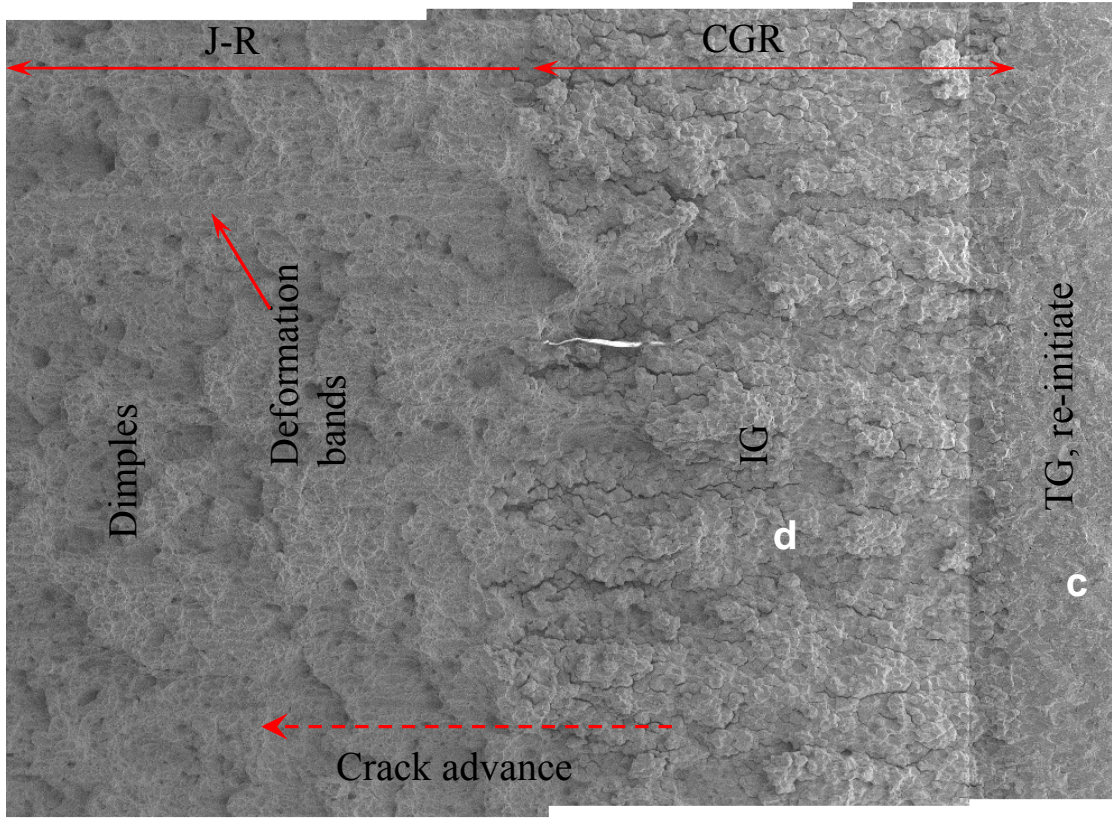
(b) Central line, 2/2

Figure 25. Fracture surface of specimen CR-04 along the sample central line.

53

Figure 26. Cyclic and SCC CGR areas marked in Fig. 25: (a) TG cleavage-like cracking during pre-cracking, (b) IG cracking in the CGR test, (c) TG cracking resulting from cyclic loading to reactivate the crack, and (d) IG with elevated secondary cracking (red arrows) at the end of the CGR test.

Figure 26. (Cont'd)

Figure 27. Elongated dimples (red arrow) during the J-R curve test of specimen CR-04.

3.3 Solution-Annealed 304L SS at ~7 dpa

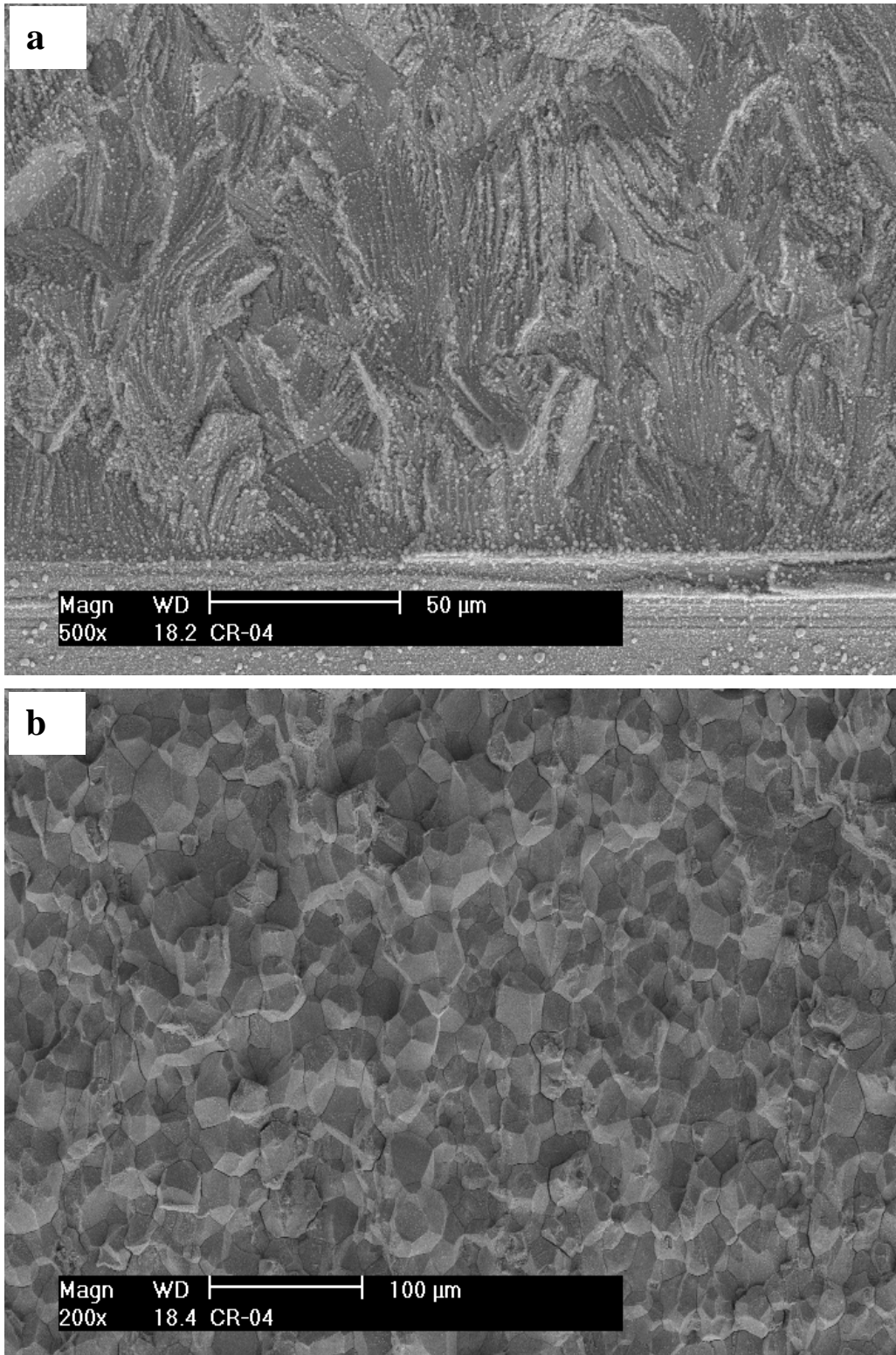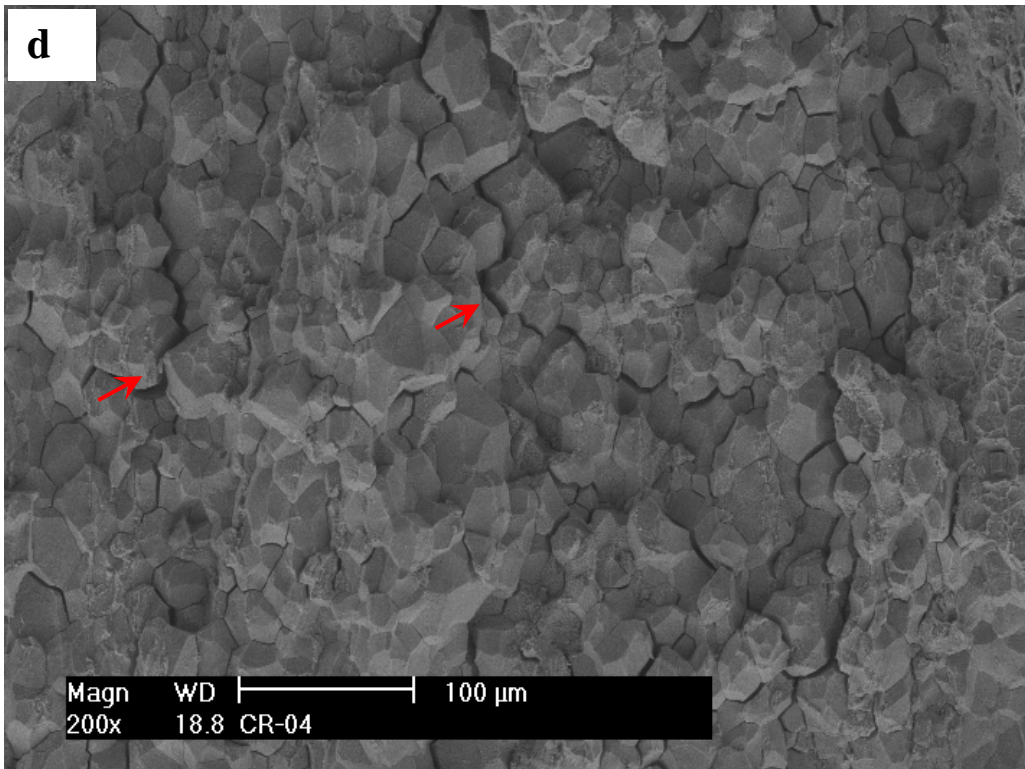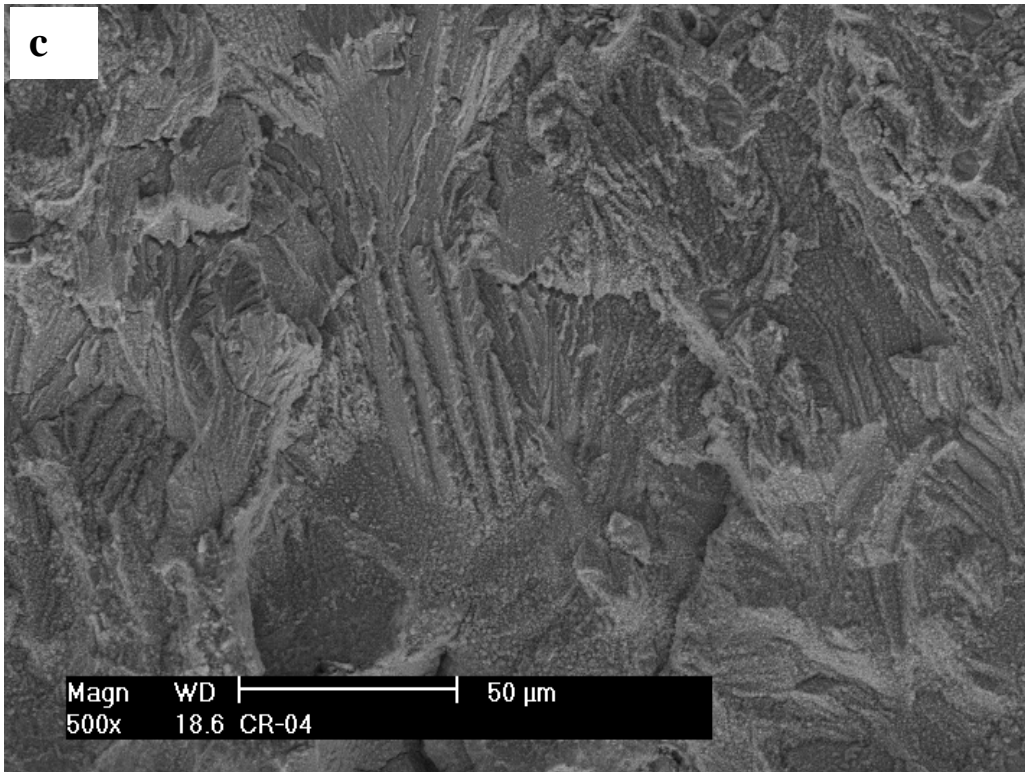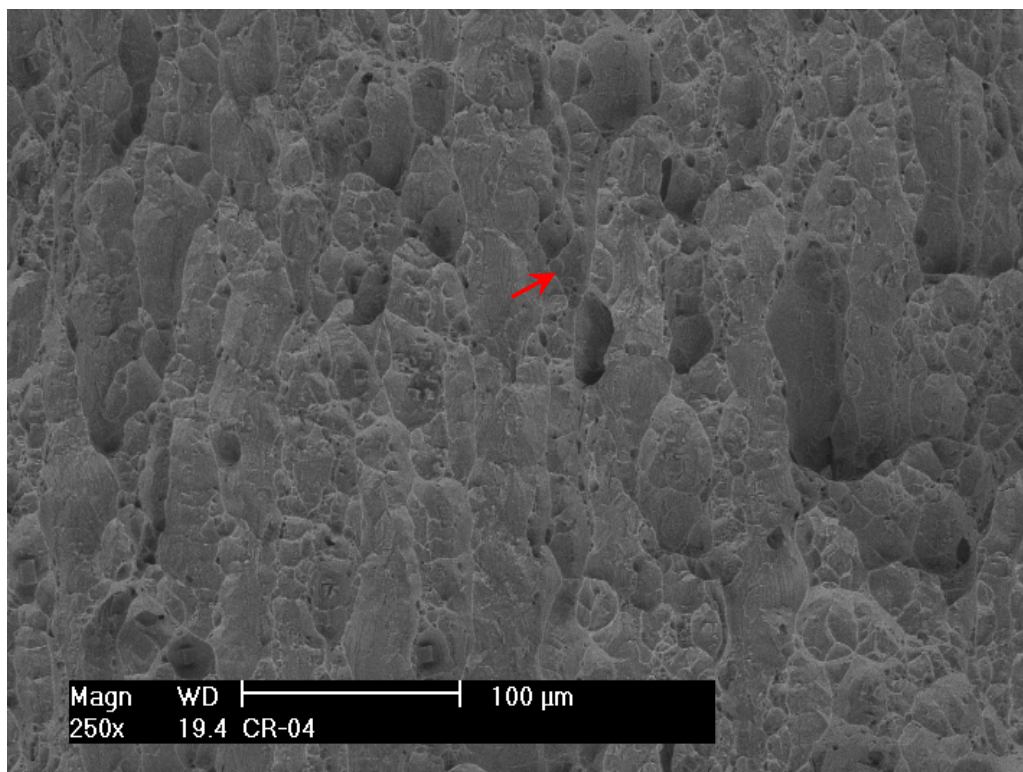*CGR and J-R curve tests*

The CGR test on the ~7-dpa SA 304L SS (specimen SW-01) was performed in PWR water. Prior to the test, the sample was exposed to the PWR water environment for 14 days to stabilize test conditions. Table 6 gives the test conditions and CGR results. The crack-length history plots of this test are shown in Fig. 28.

The test was started with fatigue precracking in the test environment. A triangle waveform at 2 Hz was used with a maximum stress intensity factor of ~15 MPa m$^{1/2}$ and a load ratio of 0.2. The initial crack growth rate was low at the machined notch, but increased rapidly after some 20 hr and 500-µm crack extension (from test period *b* to *e*). With the load ratios between 0.3 and 0.5, the measured CGRs in test periods *b-d* were very close to the fatigue growth rates in air, indicating a known cyclic cracking behavior of SSs. Environmentally enhanced cracking started to appear in test period *f* with a slow/fast sawtooth wave form and a 10-s rise time at 0.55 load ratio. In the subsequent test periods (*g-m*), environmental enhancement became more evident with further increases in rise time and load ratio. By the end of the cyclic CGR test, the crack growth rate in the environment was more than a factor of 60 higher than the fatigue growth rate in air. This strong environmental effect was not common for solution-annealed SSs tested in

56

low-DO or hydrogenated water environments,[27] suggesting an elevated cracking susceptibility at this dose.

Following the cyclic CGR test, the specimen was set to a constant load of ~16.5 MPa m$^{1/2}$ in test period *1a* with periodic partial unloading R=0.7 every 2 hr (Fig. 28d). A CGR of 1.1 x 10^{-10} m/s was recorded over ~60-μm crack extension and 127 hr. After the hold time was reduced to 1 hr in test period *1b*, a slightly higher CGR (1.6 x 10^{-10} m/s) was measured with ~60-μm crack extension. Next, after PPU removal, the test was performed under a constant K (16.6 MPa m$^{1/2}$) by load shedding. Without PPU, a lower CGR of 7.1 x 10^{-11} m/s was measured with 44-μm crack extension. After that, the same loading scheme used in test periods *1a-1c* was repeated at a higher stress intensity factor, ~20 MPa m$^{1/2}$ (Fig. 28d). The PPU was applied every 2 hr and 1 hr in test periods *2a* and *2b*, respectively. Accordingly, the CGR increased from 3.4 x 10^{-10} m/s to 4.3 x 10^{-10} m/s with the decrease of hold time. After the PPU was removed, a lower CGR of 8.6 x 10^{-11} m/s was measured over 40-μm crack extension. The effect of PPU was evident and CGR increased with increased unloading frequency.

Next, the autoclave temperature was lowered to ~290°C to study the effect of temperature on CGR. After about 22 hr, the autoclave temperature was stabilized, and the constant-load test was restarted at ~20 MPa m$^{1/2}$ with PPU every 1 hr (test period *3a*, Fig. 28e). Over 88-μm crack extension, the CGR was ~7.4 x 10^{-10} m/s, about 70% higher than that at 320°C under the same PPU condition. The test was then continued without PPU in test period *3b*. After an initial slow growth stage, a CGR of 3.9 x 10^{-10} m/s was recorded over 130 μm extension. This constant-load CGR was about a factor of 4.6 higher than that at 320°C. To further explore the effect of temperature, the test was continued in test periods in test periods *4*, *5*, *6*, and *7* at temperatures of 270, 250, 230 and 300°C, respectively, and at similar stress intensity factors between 21 and 23 MPa m$^{1/2}$. Figures 28e-f show the crack growth history of these test periods. For each test temperature, the CGR was first measured with PPU and 1-hr hold time, and then, without PPU at a constant K (approximated by load shedding). During the temperature transition periods, the sample was held at a constant load below ~4 MPa m$^{1/2}$ to minimize crack growth. All CGRs measured with PPU were much higher than those without PPU at the same temperature. Also, during test period *4a* and all subsequent test period, the "stair-step" crack growth was observed at each unloading/reloading cycle. For each constant-load test period without PPU, the CGR was measured with 40-130 μm crack extension. Between 230°C and 290°C, the measured CGR without PPU increased with temperature. Above 290°C, inverse temperature dependence was observed, and the CGR decreased rapidly with increasing temperature.

After the autoclave temperature was increased back to ~320°C, the test step before lowering the temperature was repeated at a similar stress intensity factor (~20 MPa m$^{1/2}$). Again, PPU with 1-hr hold time was applied at the beginning of the test and then removed for a constant-load CGR measurement (Fig. 28g, test period *8*). The obtained CGR was fairly close to that previously observed, confirming a consistent cracking behavior at this stress intensity factor. Next, the test was continued at higher stress intensity factors to evaluate the K dependence of crack growth behavior. For each stress intensity factor, the test was conducted with PPU and 1-hr hold time followed by a test period without PPU. When the load was increased from ~24 to ~29 MPa

$m^{1/2}$, an unstable crack advance occurred with a 70-µm jump in crack length. This unstable cracking behavior became more evident in the subsequent load transitions, when the stress intensity factor was increased. The crack length jumped as much as 150 µm when the load was increased from 37 to 46 MPa $m^{1/2}$. This cracking instability is related to the stair-step growth during PPU. Despite this instability, stable crack propagations were obtained during the test periods without PPU. As expected, the measured CGRs increased with stress intensity factor. In the last test period, the crack advanced very rapidly above ~46 MPa $m^{1/2}$. A constant K condition was not maintained adequately with load shedding, leading to a slowly increased K at the end of the test (Fig. 28h).

Table 6. Crack growth rate test on ~7-dpa SA 304L SS (specimen SW-01) in PWR water.

Test Period [1]	Test Time, h	Test Temp., °C	Load Ratio	Rise Time, s	Return Time, s	Hold Time, s	Kmax, MPa $m^{1/2}$	ΔK, MPa $m^{1/2}$	CGR in Env., m/s	CGR in Air, m/s	Crack Length, mm
Start	0.5										7.289
a [2]	3.8	318	0.21	0.23	0.23	0.02	15.3	12.1	5.11E-08	8.39E-08	7.446
b	6.0	318	0.30	0.45	0.45	0.05	14.5	10.1	1.72E-08	2.62E-08	7.507
c	8.8	318	0.30	0.45	0.45	0.05	15.5	10.8	3.61E-08	3.22E-08	7.669
d	13.7	318	0.40	0.88	0.88	0.12	15.7	9.4	1.88E-08	1.16E-08	7.815
e	23.2	318	0.50	4.29	4.29	0.71	15.7	7.8	3.23E-09	1.44E-09	7.868
f	32.3	318	0.55	8.44	4.22	1.56	15.8	7.1	1.9E-09	5.50E-10	7.902
g	47.8	318	0.60	16.6	4.14	3.45	15.9	6.3	1.07E-09	2.02E-10	7.941
h	61.3	318	0.65	24.2	4.04	5.78	15.8	5.5	5.69E-10	9.32E-11	7.961
i	100.3	318	0.70	46.9	9.39	13.1	15.9	4.8	2.95E-10	3.07E-11	7.989
j	144.8	318	0.70	944.0	9.40	26.0	16.0	4.8	2.94E-10	1.59E-11	8.023
k	199.6	318	0.70	234.8	9.39	65.2	16.2	4.8	1.74E-10	6.43E-12	8.048
l	248.9	318	0.70	469.5	9.39	130.4	16.2	4.9	1.26E-10	3.24E-12	8.064
m	311.1	318	0.70	782.3	9.39	217.7	16.3	4.9	1.27E-10	1.97E-12	8.087
1a	438.7	318	0.70	12	12	7200	16.4	4.9	1.11E-10	2.21E-13	8.148
1b	551.5	318	0.70	12	12	3600	16.6	5.0	1.58E-10	4.56E-13	8.214
1c	703.2	318	1.00	-	-	-	16.6	0.1	7.13E-11	-	8.248
2a	767.5	318	0.70	12	12	7200	19.5	5.9	3.39E-10	3.93E-13	8.351
2b	823.8	318	0.70	12	12	3600	19.8	5.9	4.29E-10	8.14E-13	8.441
2c	962	318	1.00	-	-	-	20.0	0.0	8.55E-11	-	8.482
3a	984-1007	290	0.70	12	12	3600	20.2	6.0	7.36E-10	8.17E-13	8.570
3b [2]	1126.8	290	1.00	-	-	-	20.6	-	3.94E-10	-	8.700
4a	1151.4 - 1161.7	270	0.70	12	12	3600	21.1	6.3	2.16E-09	9.17E-13	8.839
4b	1297.5	270	1.00	-	-	-	21.2	-	1.74E-10	-	8.922
5a	1367.2 - 1375.3	249	0.70	12	12	3600	21.7	6.5	2.26E-09	9.66E-13	9.064
5b	1463.6	249	1.00	-	-	-	21.7	-	1.29E-10	-	9.103
6a	1487.1 - 1495.7	228	0.70	12	12	3600	22.3	6.7	2.24E-09	1.01E-12	9.230
6b	1708.9	228	1.00	-	-	-	22.3	-	5.86E-11	-	9.271
7a	1727 – 1731	300	0.70	12	12	3600	22.8	6.9	3.18E-09	1.26E-12	9.398
7b	1767.3	300	1.00	-	-	-	23.0	-	3.56E-10	-	9.445
7c [3]	1799.6	300	1.00	-	-	-	3.8	-	3.65E-11	-	9.457
8a	1823.5-1827.9	318	0.70	12	12	3600	23.5	7.1	3.54E-09	1.45E-12	9.582

Table 6. (Cont'd)

Test Period [1]	Test Time, h	Test Temp., °C	Load Ratio	Rise Time, s	Return Time, s	Hold Time, s	Kmax, MPa m$^{1/2}$	ΔK, MPa m$^{1/2}$	CGR in Env., m/s	CGR in Air m/s	Crack Length, mm
8b	1968	318	1.00	-	-	-	23.7	-	9.35E-11	-	9.634
9a	1972	318	0.70	12	12	3600	28.8	8.6	6.39E-09	2.84E-12	9.796
9b	2088.6	318	1.00	-	-	-	29.1	-	1.68E-10	-	9.871
10a	2091.8	318	0.70	12	12	3600	36.4	10.9	1.07E-08	6.13E-12	10.105
10b	2207.8	318	1.00	-	-	-	37.2	-	3.19E-10	-	10.233
11a	2212	318	0.75	12	12	3600	45.6	11.4	1.24E-08	7.32E-12	10.570
11b-0	2235	318	1.00	-	-	-	47.3	-	8.36E-10	-	10.650
11b-1 [4]	2250	319	1.00	-	-	-	48.4	-	1.99E-09	-	10.750

[1] Cyclic test periods are named in alphabetical order, and constant-load test periods are named in numerical order.

[2] The CGR at the end of the test period is reported.

[3] Lower the load to minimize crack growth prior to changing test conditions.

[4] Inadequate load shed resulting in a rising K condition. The reported CGR is for the later part of the test period.
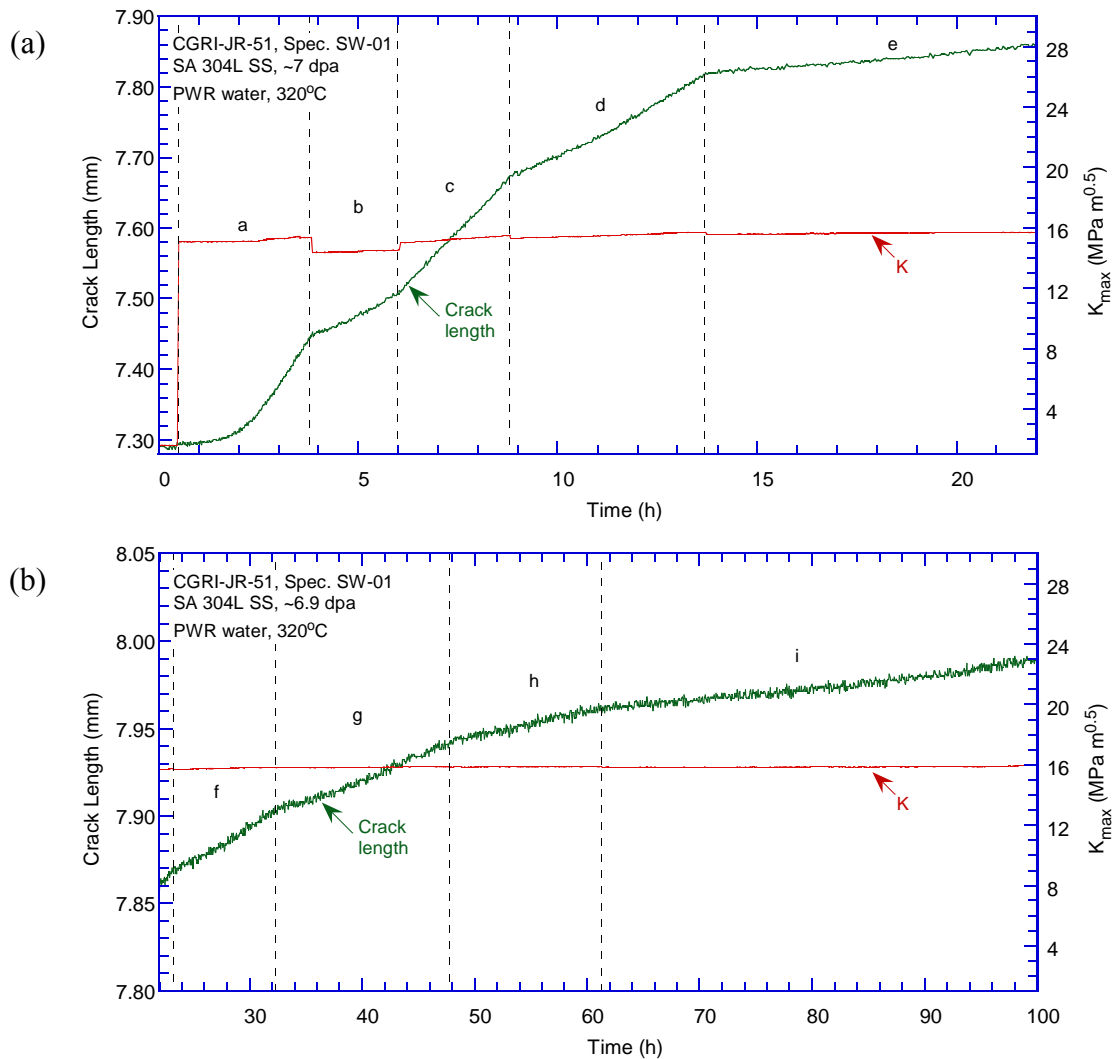

Figure 28. Crack-length-vs.-time plot for specimen SW-01 (~7-dpa CSA 304L SS) tested in PWR environment: test periods (a) a-e, (b) f-i, (c) j-m, (d) 1a-2c, (e) 3a-4b, (f) 5a-7b, (g) 8a-9b, and (h) 10a-11b.
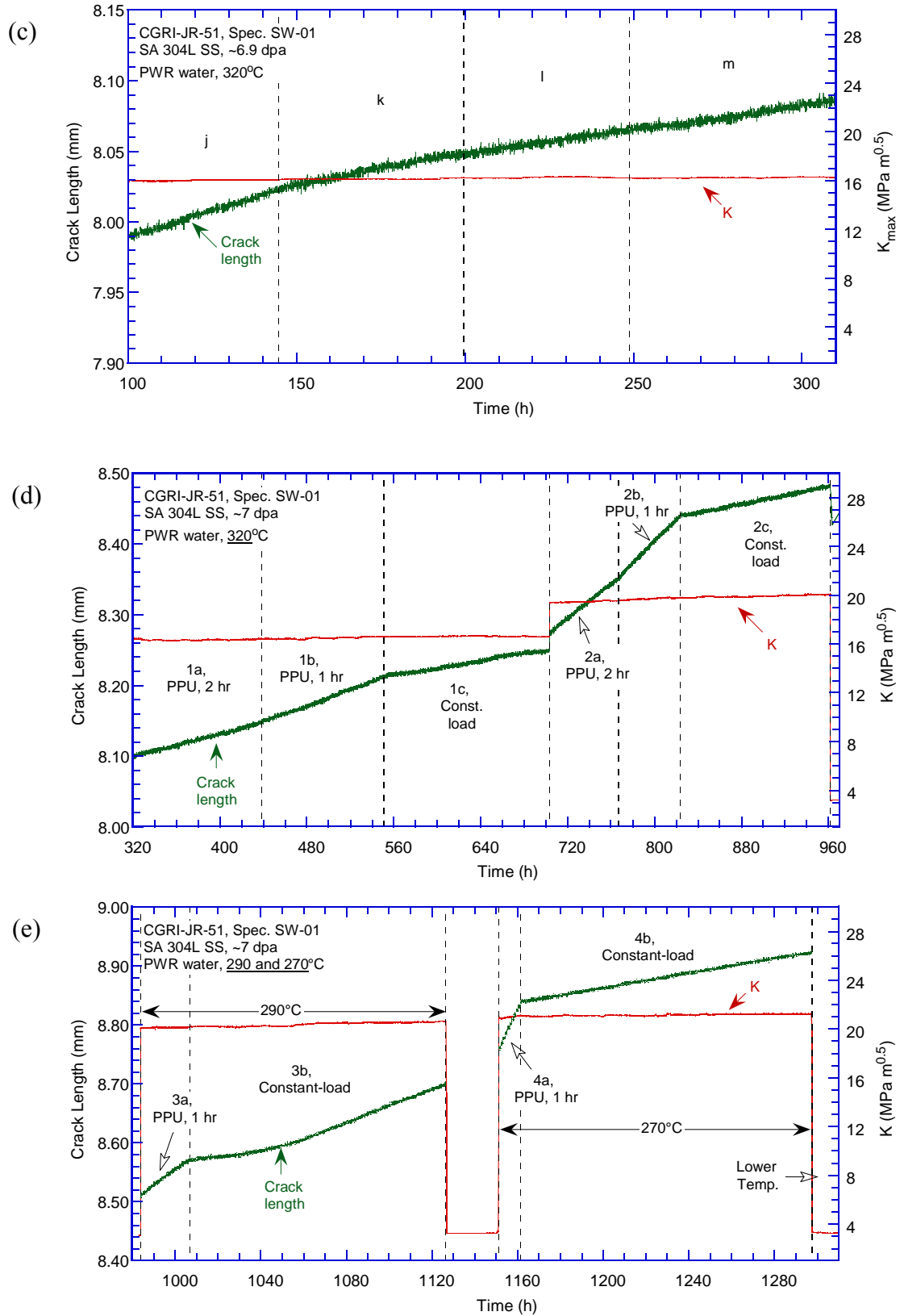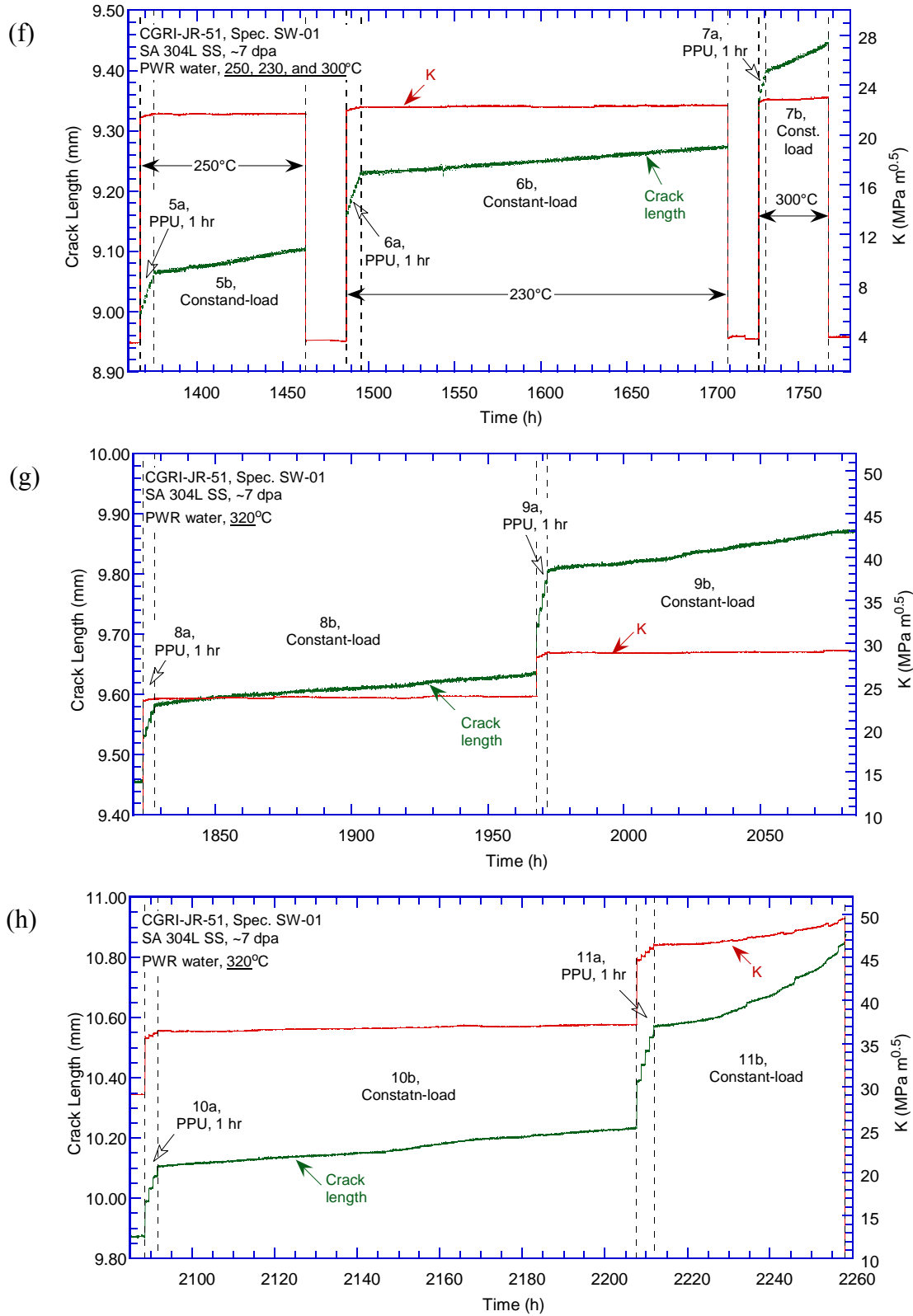
Figure 28. (Cont'd)

(f)

CGRI-JR-51, Spec. SW-01
SA 304L SS, ~7 dpa
PWR water, 250, 230, and 300°C

K

7a,
PPU, 1 hr

7b,
Const.
load

5a,
PPU, 1 hr

6a,
PPU, 1 hr

6b,
Constant-load

Crack
length

5b,
Constand-load

250°C

230°C

300°C

(g)

CGRI-JR-51, Spec. SW-01
SA 304L SS, ~7 dpa
PWR water, 320°C

9a,
PPU, 1 hr

8a,
PPU, 1 hr

8b,
Constant-load

9b,
Constant-load

K

Crack
length

(h)

CGRI-JR-51, Spec. SW-01
SA 304L SS, ~7 dpa
PWR water, 320°C

11a,
PPU, 1 hr

K

10a,
PPU, 1 hr

10b,
Constatn-load

11b,
Constant-load

Crack
length

Figure 28. (Cont'd)

61

All cyclic CGRs obtained from specimen SW-01 are plotted in Fig. 29 as a function of fatigue CGRs in air. The CF curve developed by Shack and Kassner[27] for unirradiated SSs in low-DO high-purity water (0.2 ppm DO) is also included in the figure as a reference. The data points obtained at high rise times and load ratios lay above the reference CF curve, implying an elevated cracking susceptibility.
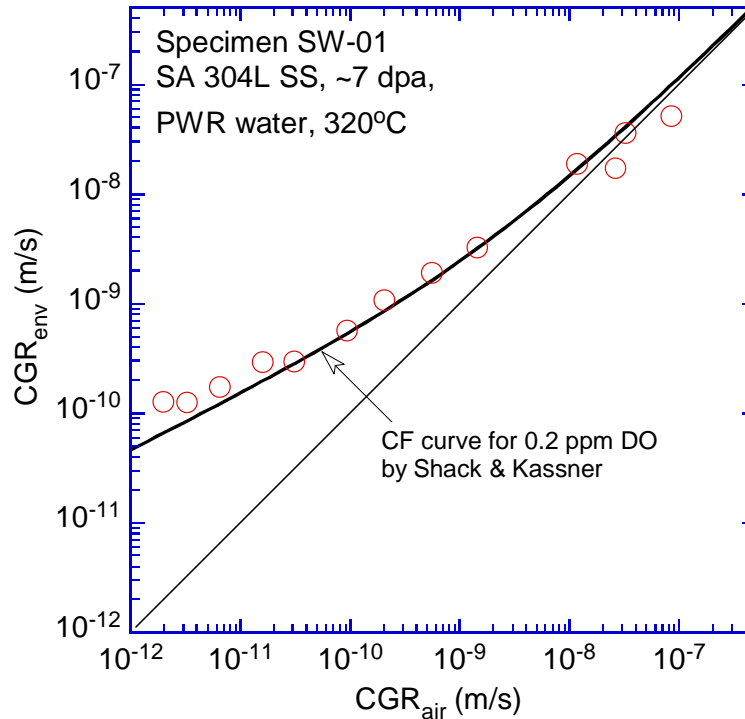

Figure 29. Cyclic CGRs of specimen SW-01, a SA 304L SS irradiated to ~ 7 dpa and tested in PWR water.

Constant-load CGRs at 320°C with and without PPU are shown as a function of stress intensity factor in Fig. 30. The NUREG-0313 curve is also included as a reference. Without PPU, the cracking susceptibility is moderate for the irradiated 304L SS, and the measured CGRs are in the range of 7×10^{-11} and 7×10^{-10} m/s between ~17 and 48 MPa m$^{1/2}$. Note that the maximum K value for a valid train fracture toughness of this DCT sample is about ~33 MPa m$^{1/2}$. Thus, the constraint specified in ASTM E399 to maintain a high level of stress triaxiality was not sustained in the test periods with high stress intensity factors. While the CGRs obtained under static stress intensity factors are consistent with the NUREG-0313 curve, CGRs are much higher with PPU. The effect of PPU is also more evident at high stress intensity factors. Below ~20 MPa m$^{1/2}$, the CGRs with PPU are a factor of 2-5 higher than the CGRs measured under constant K. At 25-35 MPa m$^{1/2}$, the differences of the CGRs with and without PPU can be as much as a factor of 38. In this study, a constant K condition was not maintained adequately above ~38 MPa m$^{1/2}$, and the sample was subject to a slowly rising K in the last test period (see Fig. 28h). The average CGR measured for the later part of this test period (the open diamond symbol in Fig. 30) is about a factor of two higher than the NUREG-0313 curve.
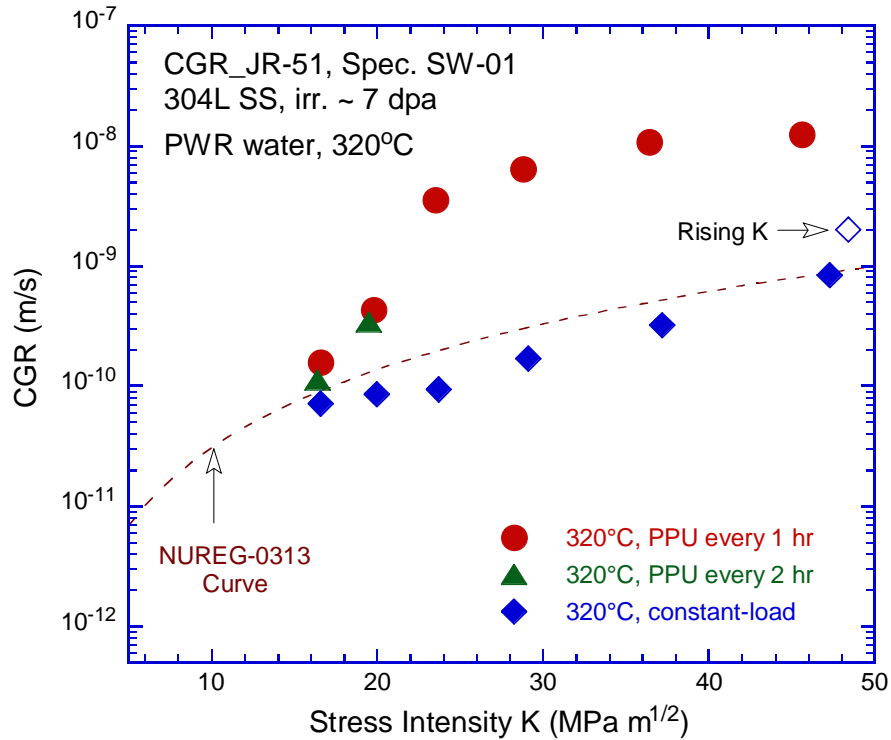
Figure 30. SCC CGRs of specimen SW-01 at ~320°C.

The effect of temperature on crack growth behavior is evaluated between 230 and 320°C in test periods *2* to *8* with and without PPU. The stress intensity factors are similar in these test periods (~20-24 MPa m$^{1/2}$). Due to the stair-step growth, the average CGRs in the test periods with PPU were independent of test temperature. Without PPU, however, the constant-load CGRs displayed different behavior below and above 290°C. Below 290°C, the CGR increased with temperature. Above 290°C, CGR sharply declined with temperature increases to 320°C. Figure 31 shows the temperature dependence of constant-load CGR obtained in this study. The CGR values plotted in the figure are normalized to 20 MPa m$^{1/2}$ with a power exponent of 2.16 to account for their K dependence. An Arrhenius type behavior can be seen below 290°C, and the estimated activation energy is ~61.5 kJ/mol.

Following the CGR test, several gentle fatigue cycles were applied to prepare the sample for a fracture toughness J-R curve test in the PWR environment at 320°C. The test was performed with a constant strain rate of 0.43 μm/s, and the load and sample extension were recorded outside the autoclave. Due to a malfunction of the DCPD system, the readings were unexpectedly low after the first few data points in this test. The system later recovered and the DCPD measurement became normal again. Since we lost the crack extension measurements in the middle of the test, we could only use the good data points at the beginning of the test and some points later in the test for the curve fitting the J-R response. A J value of 95 kJ/m^2 was estimated for the sample at 0.2-mm offset.
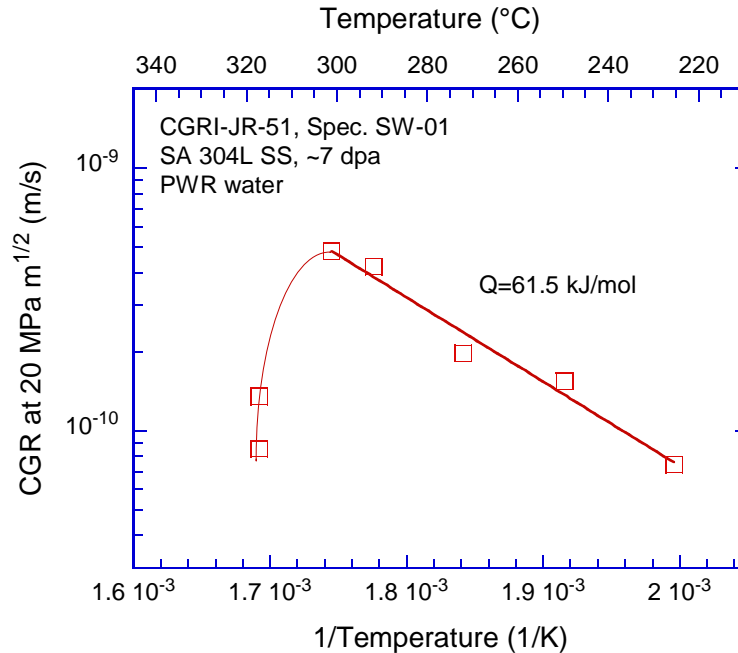
Figure 31. Temperature dependence of constant-load CGR for specimen SW-01.

Fractographic examination

After the test, the sample was broken open under fatigue loading in an air atmosphere at room temperature. Figure 32 shows the entire fracture surface of the specimen. The crack front is straight for the precrack and CGR test, indicating a well-controlled loading condition during the test. The fatigue precrack area is flat, showing predominately TG morphology. A fully IG cracking area follows as the test continued into the CGR test region. The fracture surface becomes increasingly uneven in the region of high stress intensity factor. Finally, the ductile dimple fracture replaces the IG morphology in the J-R curve test region. The final crack length is measured on the SEM image, and all crack extensions reported have been corrected with the SEM measurements.

More details of the fracture morphologies can be seen along the sample central line in Fig. 33. Several areas marked a - d in the figure are also shown in Fig. 34. While the TG cracking was the dominant morphology in the fatigue precrack stage, some IG features can also be identified in the precracking area, as shown in Fig. 34a. In the IG region, more secondary cracks were developed close to the end of the CGR test (Fig. 34c). Also, small ductile tearing areas appear in the later part of the CGR test under high stress intensity factors. After the CGR test, dimples of various sizes are the sole fracture morphology in the J-R test region (Fig. 34d), indicating a ductile fracture by microvoid coalescence.
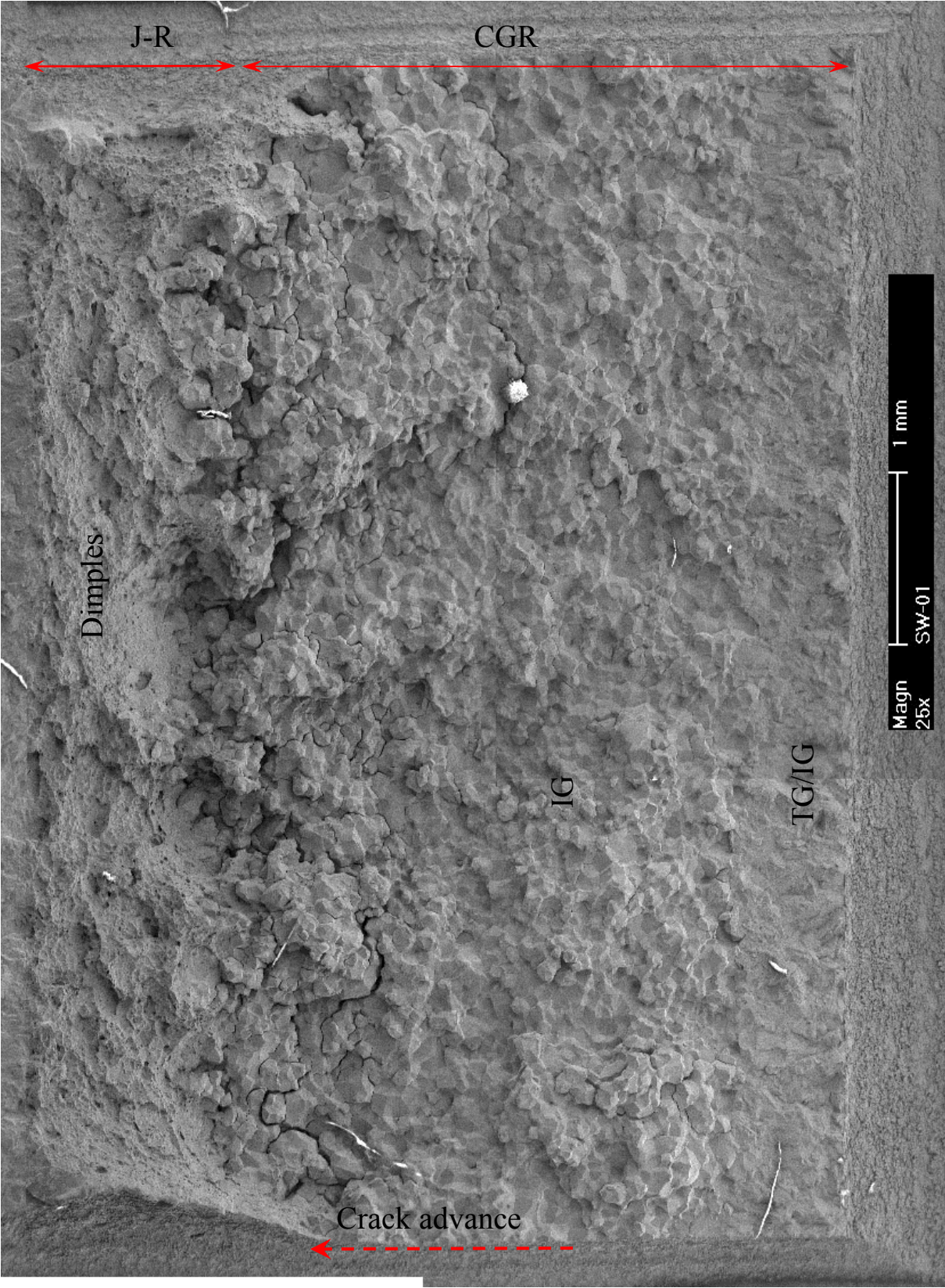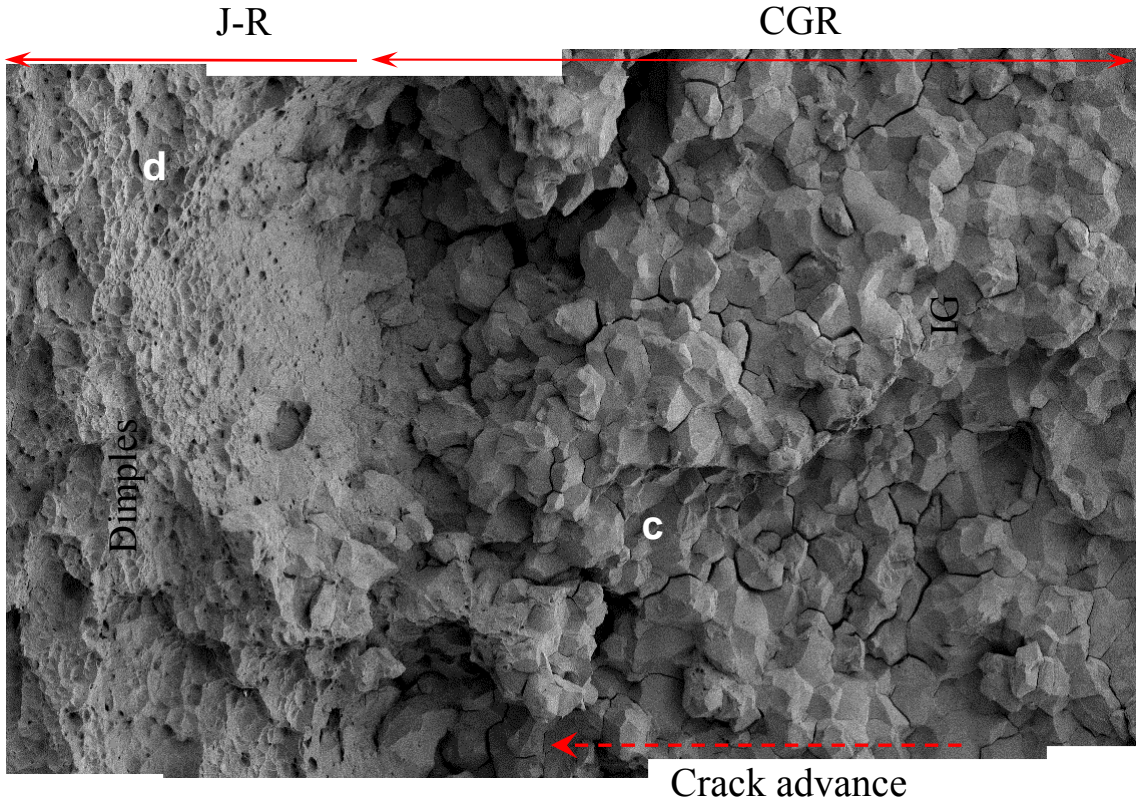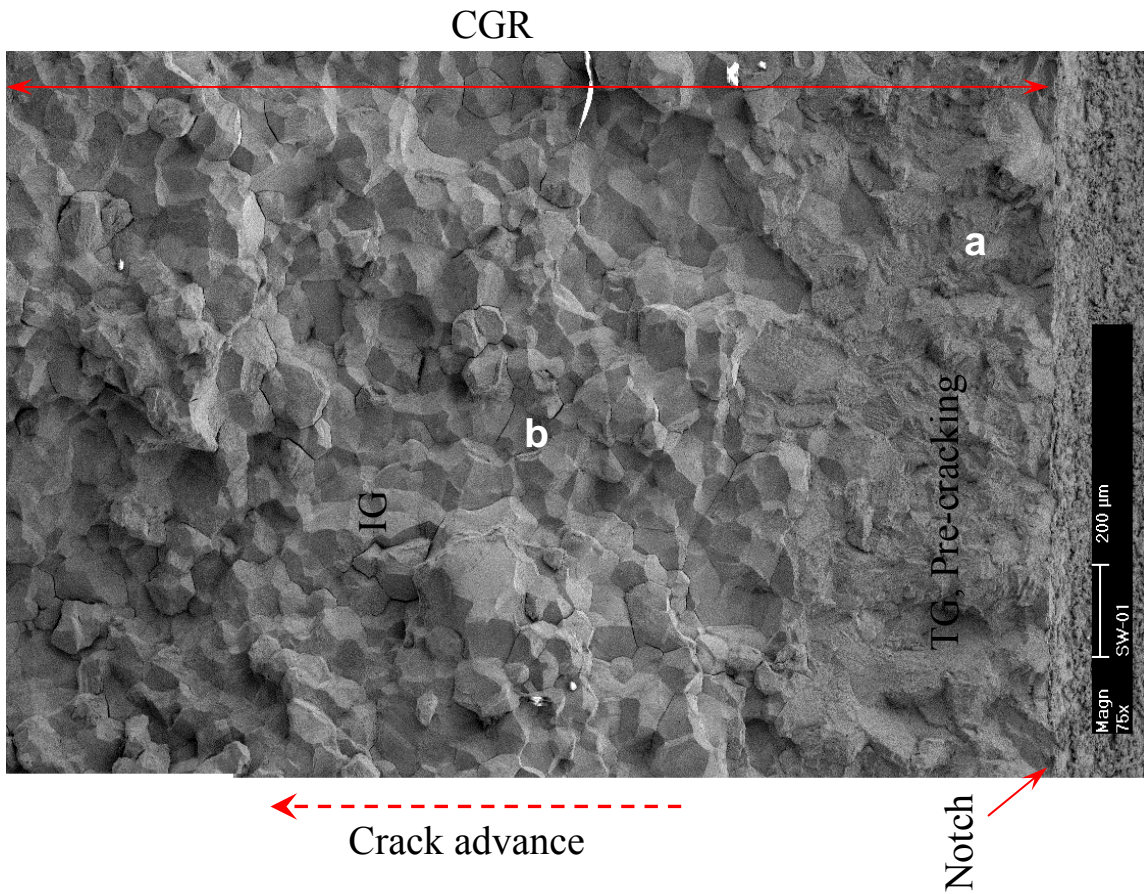
Figure 32. Fracture surface of specimen SW-01 tested in PWR water.

(b) Central line, 2/2

(a) Central line, 1/2

Figure 33. Fracture surface of specimen SW-01 along the sample central line.
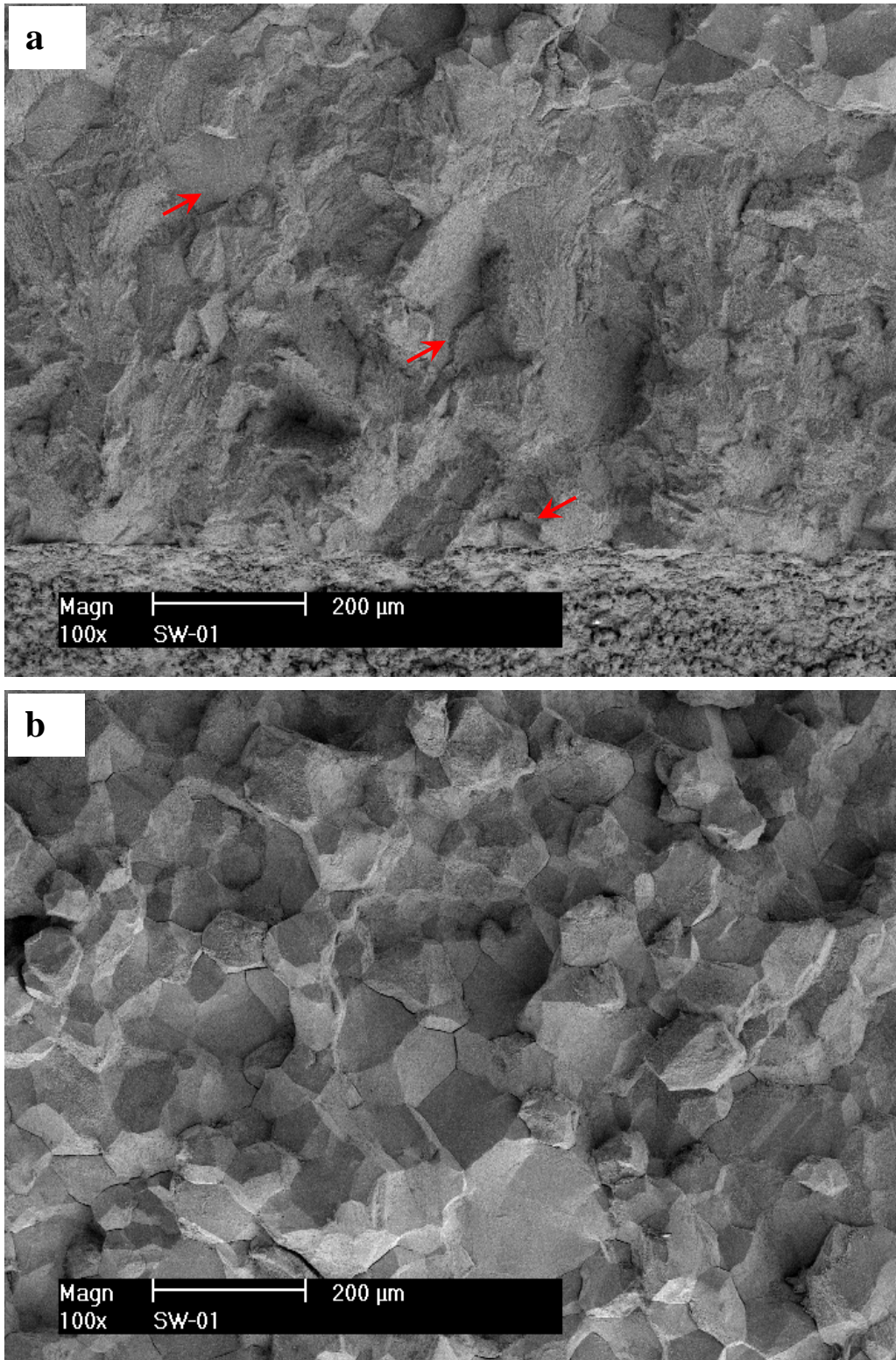
66

Figure 34. The areas marked in Fig. 33: (a) TG pre-cracking area with IG facets (red arrows), (b) IG cracking during CGR test, (c) IG cracking with ductile tearing areas (red arrows) close to the end of CGR test, and (d) ductile dimple fracture during J-R test.
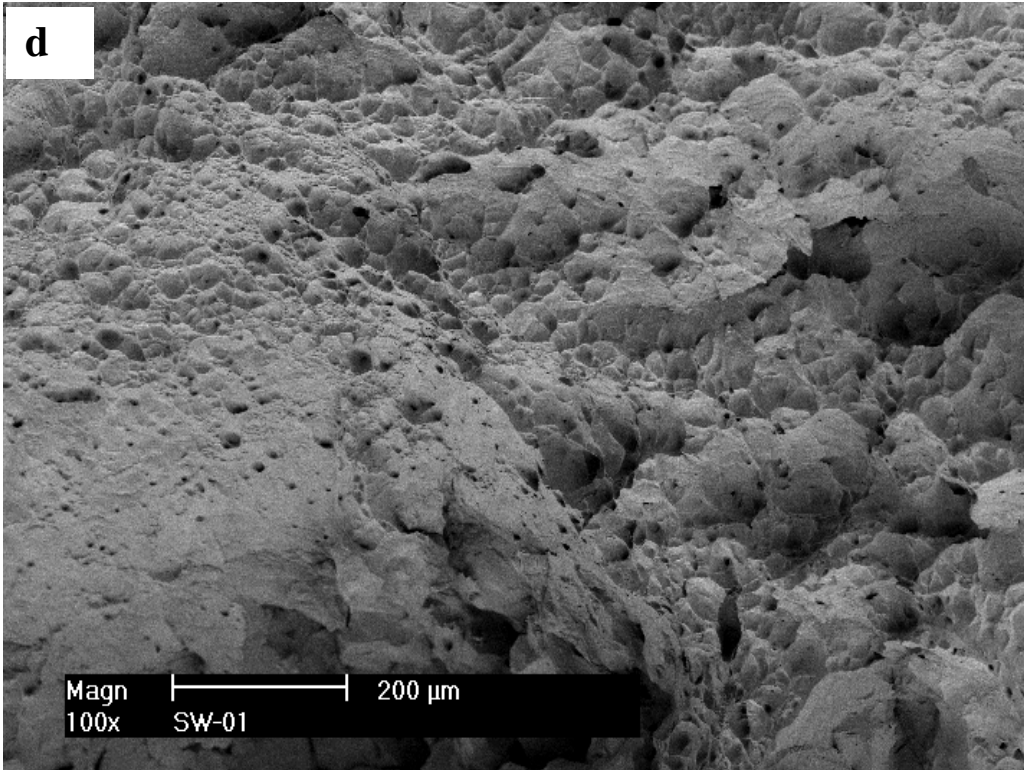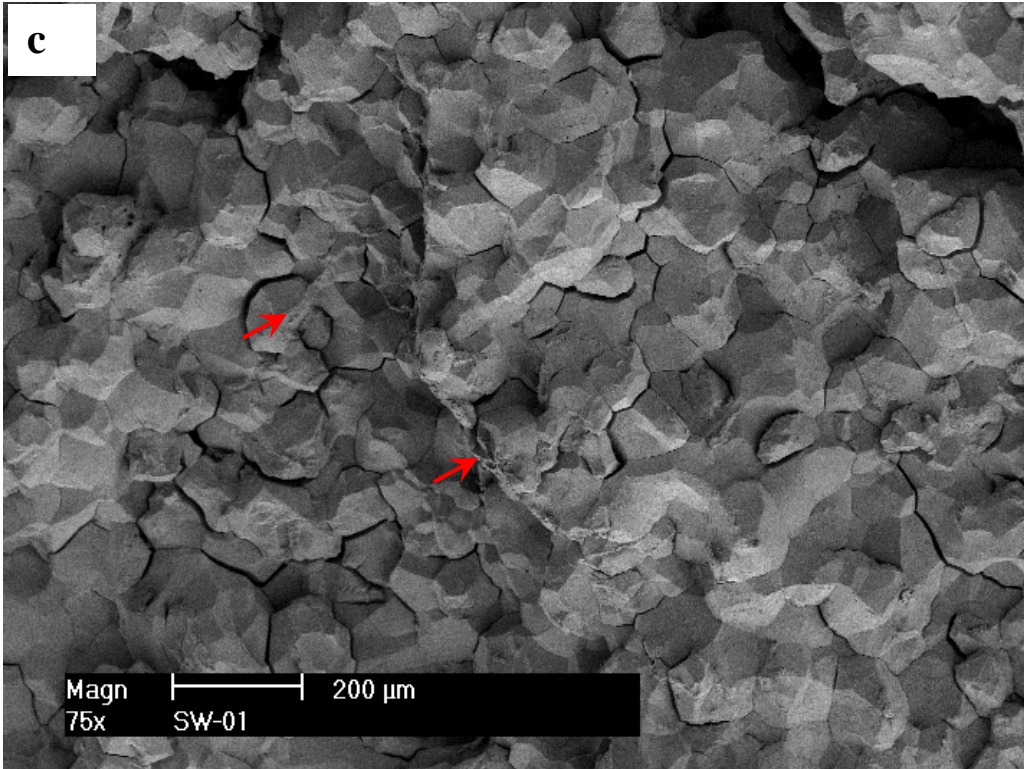
Figure 34. (Cont'd)

4   DISCUSSION

Four DCT specimens irradiated in the BOR-60 reactor were tested in either a low-DO high-purity water or PWR water environment. The materials were CW 316 and SA 304L SSs irradiated to a dose of ~5 to 8 dpa. Crack propagation rates were evaluated under cyclic and constant-load conditions, and fracture toughness J values were estimated at the 0.2-mm offset line. Environmentally enhanced cracking was readily induced during these tests, and SCC CGRs were measured at different stress intensity factors with and without PPU. The effect of test temperature was also assessed with two tests in PWR water and one test in low-DO high-purity water. While TG cracking was the main fracture mode in the precracking regions of all tests, the SCC CGR regions showed predominately an IG morphology. Ductile dimple fracture was the solo fracture mode in the J-R test region.

4.1 Cyclic Crack Growth Rates

Cyclic CGRs obtained in the current study were analyzed with a superposition model previously developed by Shack and Kassner.[27] By assuming that the environmental contribution to cyclic CGR was correlated with fatigue growth rate in air ($CGR_{cf} \propto CGR_{air}^{0.5}$), Shack and Kassner determined the corrosion fatigue curves that bound the cyclic CGRs of unirradiated SSs tested in high-purity water containing 0.2 and 8 ppm DO. To assess the corrosion fatigue performance of irradiated SSs in the low-corrosion-potential environments, each dataset of cyclic CGRs was fitted to the superposition model. The curve fitting results are shown in Fig. 35 along with the corrosion fatigue line of unirradiated SSs for 0.2-ppm DO as a reference. Environmental enhancement was evident for all tests in the low-corrosion-potential environments. While the fitting curves of the ~7-8 dpa specimens lie above the 0.2-DO reference line, the fitting curves of the ~5-dpa specimens are below the reference line. Also shown in Fig. 36, the fitting coefficient "A" (in $CGR_{cf} = A \cdot CGR_{air}^{0.5}$) is at least a factor of two higher at ~7-8 dpa than at ~5 dpa. This contrast in environmental enhancement suggests a significant role of neutron irradiation on cyclic cracking behaviors between ~5 and ~7 dpa in the low-corrosion-potential environments.

Figure 37 shows the fracture surfaces of the cyclic pre-cracking regions of the four CGR tests carried out in the low-corrosion-potential environments. While the dominant fracture mode is TG cracking for all specimens, IG features are easily identified in the ~7-dpa SA 304L SSs, even at the very beginning of the cyclic test. The two CW 316-Ti SS specimens are very similar, showing extensive TG cracking with cleavage-like morphology. The ~5-dpa CW 316 SS contains inclusion stringers lying along the deformation bands, as shown in Fig. 37a. The presence of stringers does not seem to elevate environmental effect considerably.
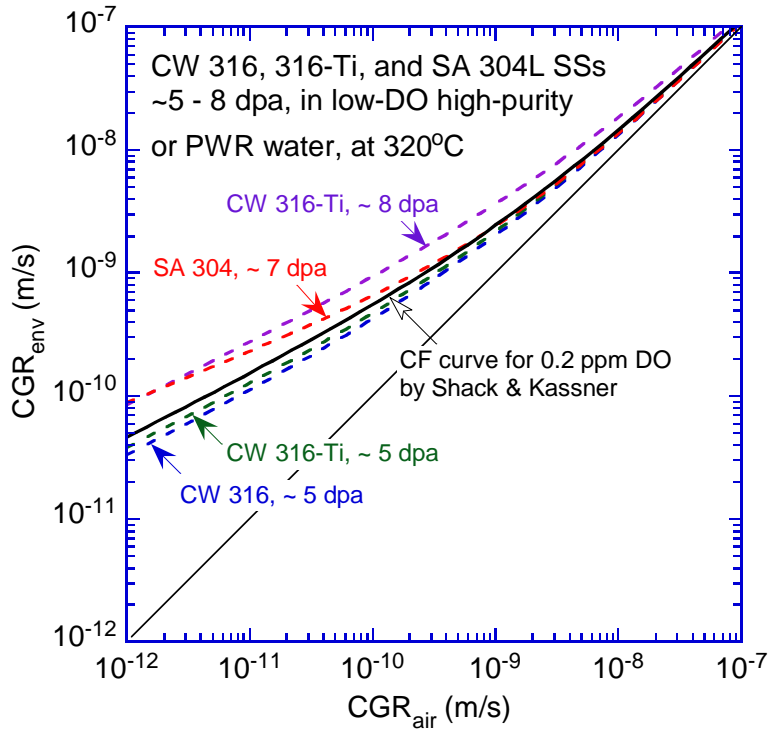
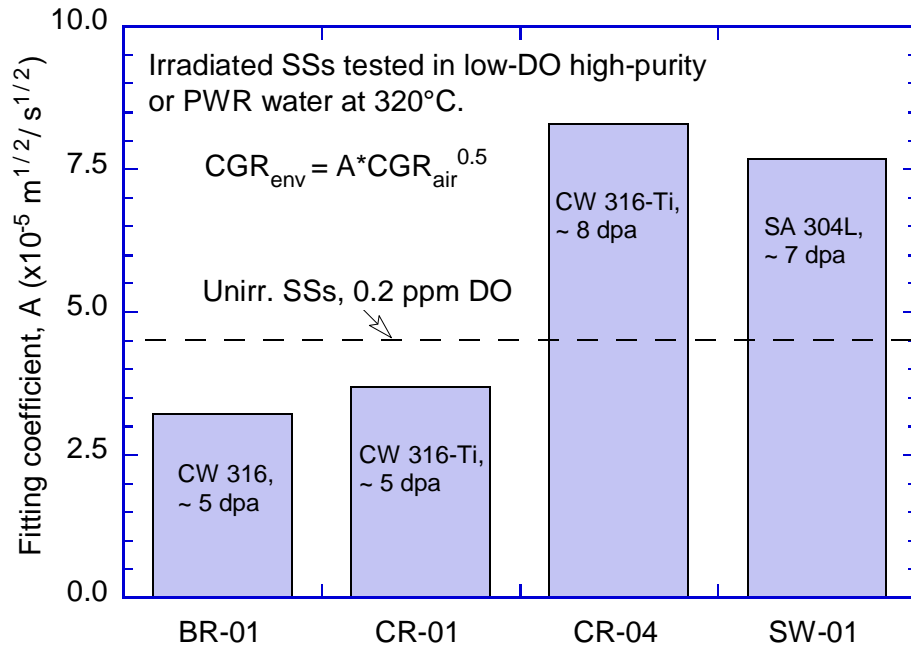Figure 35. Best-fit curves of the cyclic CGR data from this study.

Figure 36. Corrosion-fatigue behaviors of the four specimens tested in this study.
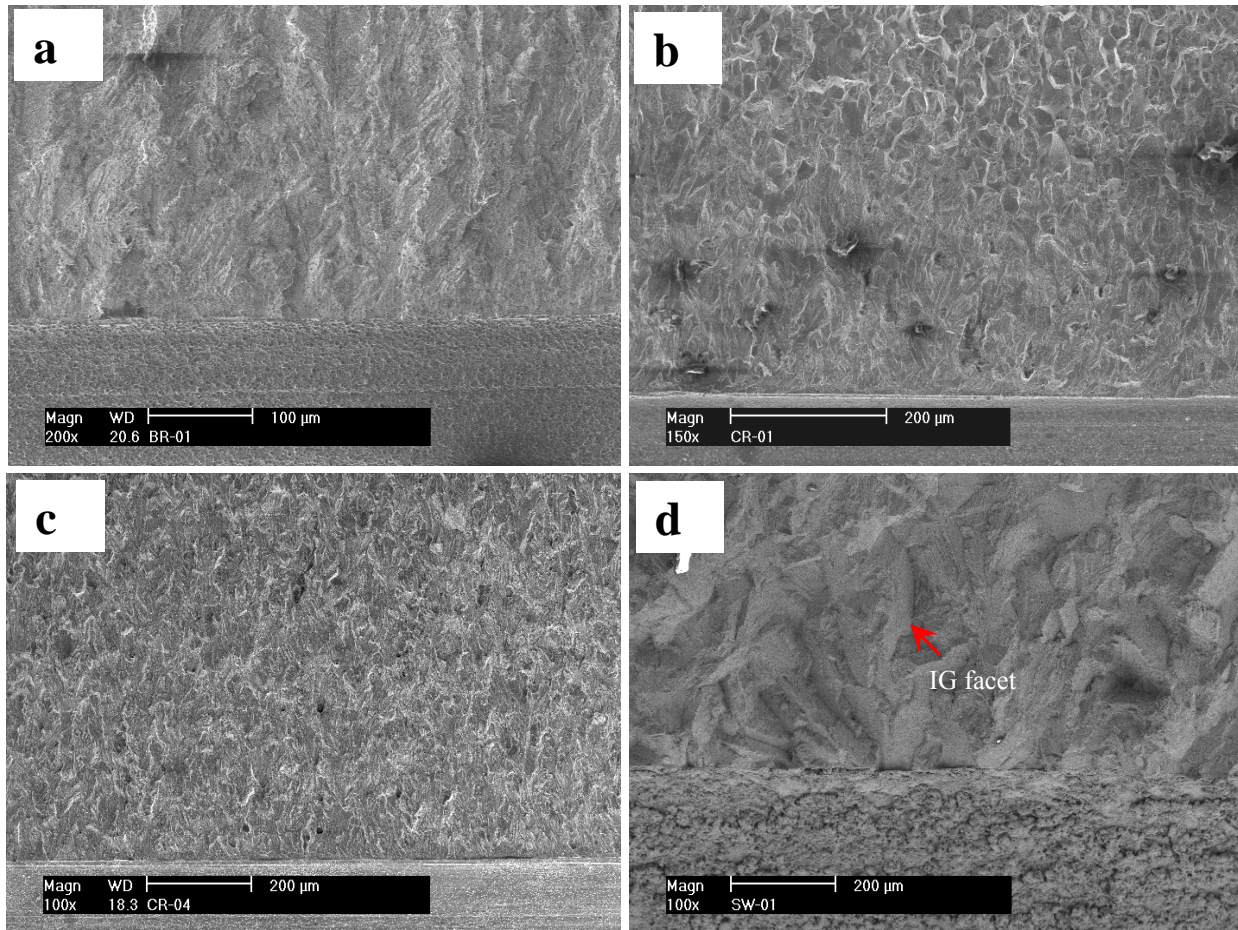
Figure 37. Cyclic pre-cracking regions of (a) ~5-dpa CW 316, (b) ~5 dpa CW 316-Ti, (c), ~8-dpa CW 316-Ti, and (d) ~7-dpa SA 304L SSs (crack advanced from bottom to top).

4.2 SCC Crack Growth Rates

Table 7 summarizes the test conditions and the obtained SCC CGRs under constant load without PPU. Only the test periods in an increasing order of stress intensity factor are included in the table. These data are plotted in Fig. 38 along with the NUREG-0313 curve as a reference. The ~5-dpa CW 316 SS shows the lowest susceptibility to SCC among these samples, and the obtained CGRs are one order of magnitude lower than the NUREG-0313 line. The two CW 316-Ti SS samples at ~5 and ~8 dpa have the highest CGRs, especially in the regime of high stress intensity factor. The SA 304L SS shows a moderate cracking susceptibility at ~7 dpa and its CGRs are just below the NUREG-0313 line. Each of the four datasets is fitted to a power correlation with stress intensity factor, and the obtained exponents are shown in Fig. 38. Three of the four exponents are between 2.0 and 2.7. The ~5-dpa CW 316-Ti SS, however, shows a much higher K exponent of 4.6 between ~15 and ~38 MPa m$^{1/2}$. The goodness of fit for this sample is also the worst of the tested samples, as shown in Fig. 38, indicating poor data consistency. This dataset can also be viewed as two regions of similar K dependence with a sharp transition between ~26 and ~30 MPa m$^{1/2}$. It is not clear at present if the K-dependency is

71

different at different stress intensity factors. Additional test is needed to clarify the crack growth response to the applied stress for this sample in the intermediate stress level. Except for this anomaly of the ~5-dpa CW 316-Ti SS, all other tests under constant loads without PPU show a K dependence similar to that of the NUREG-0313 curve for a wide range of stress intensity factors.

Table 7. Constant-load CGRs for increasing stress intensity factor without PPU at 320°C.

Sample ID	Material	Dose (dpa)	Environment	K (MPa m$^{1/2}$)	SCC CGR, w/o PPU (m/s)	Test Period [1]
BR-01	CW 316	~5	Low-DO, high-purity	16.3	5.43E-12	1b
				20.0	1.03E-11	2b
				20.1	1.41E-11	2d
				25.7	1.75E-11	3b
				32.8	2.84E-11	4d
				38.7	3.62E-11	5c
CR-01	CW 316-Ti	~5	Low-DO, high-purity	14.7	9.00E-11	1c
				19.3	1.50E-10	2a
				25.3	2.70E-10	3c
				31.6	2.98E-09	4b
				32.5	2.21E-09	4d
				37.7	5.32E-09	9
CR-04	CW 316-Ti	~8	PWR	12.3	1.64E-10	1a
				17.1	1.07E-09	2a
				17.9	1.18E-09	2g
				37.7	4.88E-09	8b
				46.2	1.03E-08	9
SW-01	SA 304L	~7	PWR	16.6	7.13E-11	1c
				20.0	8.55E-11	2c
				23.7	9.35E-11	8b
				29.1	1.68E-10	9b
				37.2	3.19E-10	10b
				47.3	8.36E-10	11b

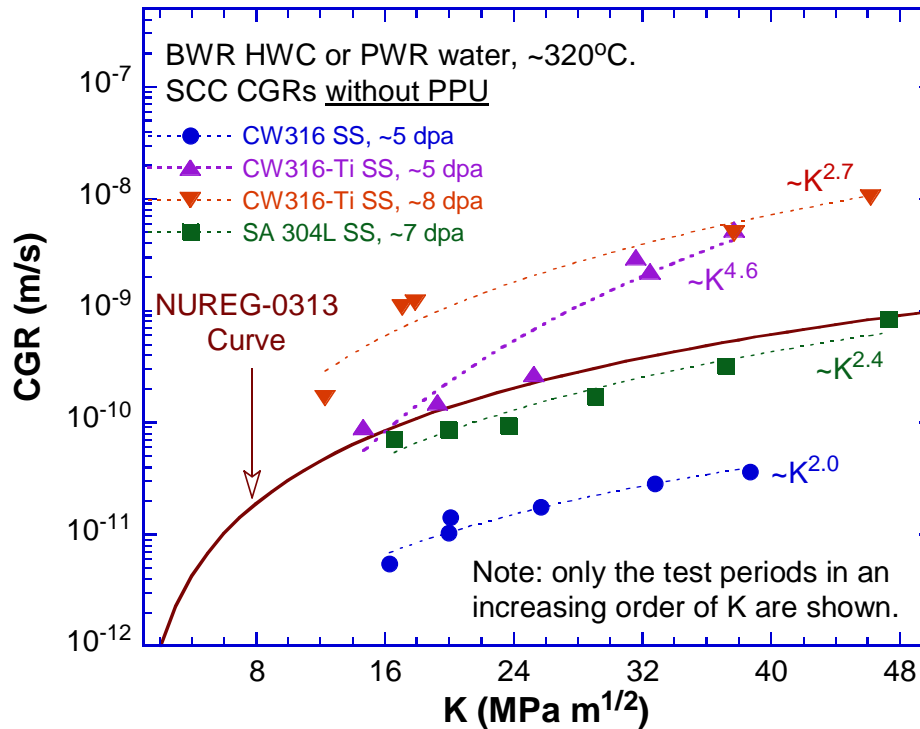[1] The test periods with a decreasing order of K are excluded.

Figure 38. Constant-load CGRs without PPU at 320°C in this study.

4.2.1 Effect of PPU

Periodic partial unloading has a significant effect on the cracking behavior of irradiated SSs. For all tests carried out in this study, the measured CGRs in the test periods with PPU were much higher than those without PPU (approximately static K by load shedding) at the same stress intensity factors. Figure 39 shows several test periods with and without PPU for the ~7-dpa SA 304L SS, and the influence of PPU on the cracking behavior is evident. This strong effect of PPU was different from that observed at lower doses and in BWR NWC (a high-corrosion-potential environment).[15] Periodic partial unloading seemed not to have a substantial effect on the measured CGRs in high-purity water with 700-800 ppb DO for irradiated SSs.[15] The different sensitivity to partial unloading suggests a combined effect of SCC and low-cycle fatigue on the crack growth response of irradiated SSs in the low-corrosion-potential environments.
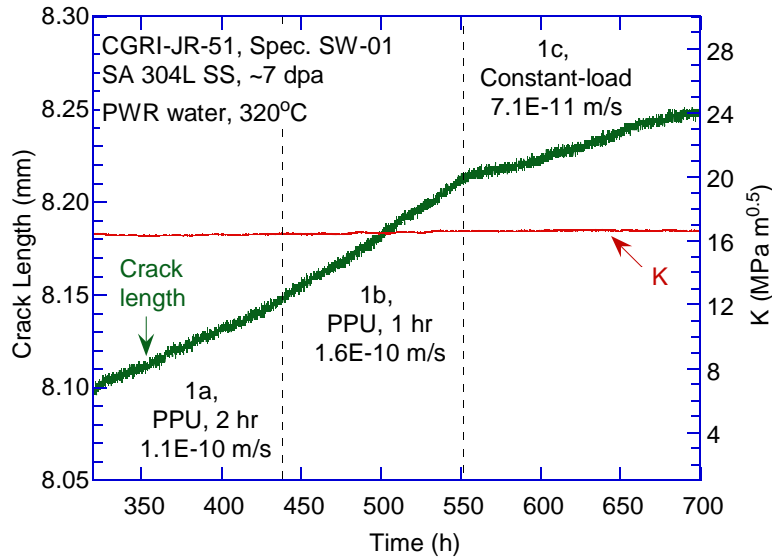
Figure 39. Effect of PPU without stair-step growth.

In addition to elevated CGRs, "stair-step" cracking was also often observed with PPU, as shown in Fig. 40. With the stair-step crack growth, an unstable crack extension occurred at each unloading and re-loading cycle. Since the crack advance was so large for each PPU, unbroken ligaments were unlikely to be responsible for the repeated stair-step crack growth. A dynamic straining condition created by PPU may contribute to the unstable crack extension, and a plastic instability resulting from irradiation damage may further facilitate this cracking behavior. With the stepped cracking, the height of the stair steps dominated the measured CGRs, and the crack extension during the hold time was negligible. Thus, in addition to the applied stress intensity factor, the magnitude and frequency of unloading became important factors for the CGRs measured in the test periods with PPU.

While the stair-step cracking can be seen at all stages of the CGR tests, it was observed more frequently at the high stress intensity factors and in the later stage of the CGR tests. The stepped crack extension can even occur during the load transitions between different test periods (e.g., Figs. 4k-l, 11m-n, 19k-l, and 28f-h) or under a condition of slowly rising K (e.g., Figs. 19l and 28h), where dynamic straining is also present. Because of the significant contributions of the stair steps to the overall crack extensions, whether or not a stepped cracking behavior prevails could have a profound impact on the measured CGRs. Figures 41a and 41b show two test periods with continuous and stepped cracking behaviors, respectively. For comparison, the spans of the time and crack length axes are set to be the same in both plots. With the slightly different stress intensity factors, the two test periods were performed under an identical PPU condition (i.e., R=0.7 and 1-hr hold time). Despite the similar loading condition, the two average CGRs differed by a factor of eight. It is clear that stair-step growth plays a key role in the cracking of irradiated SSs in the low-corrosion-potential environments.
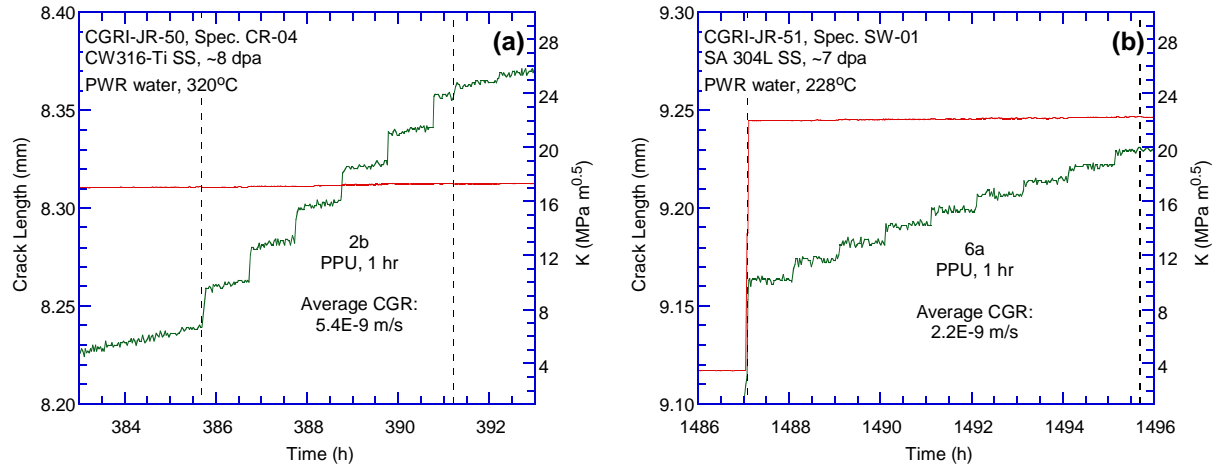
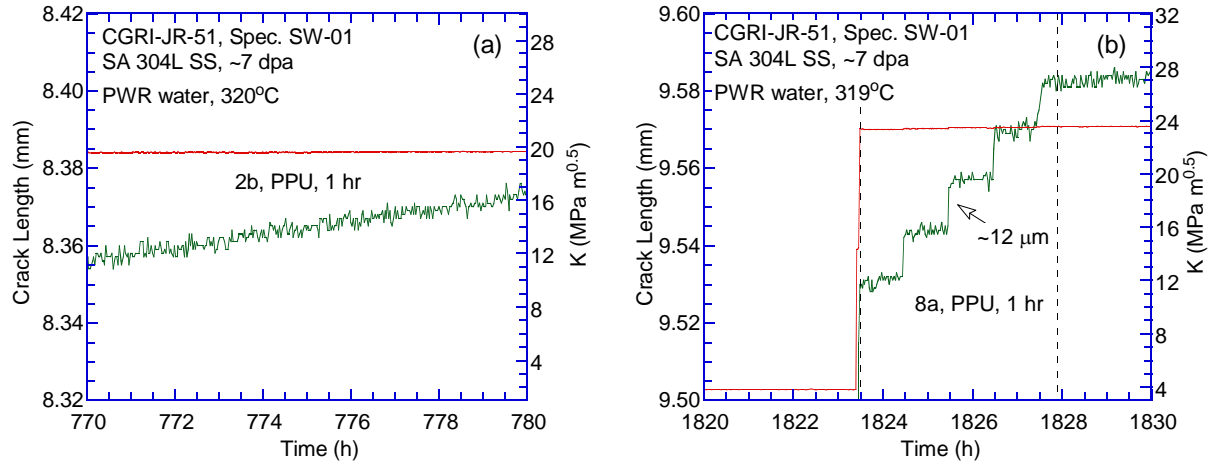Figure 40. Typical stair-step crack growth behavior with PPU: (a) ~8-dpa CW 316-Ti, and (b) ~7-dpa SA 304L SS.

Figure 41. Different CGRs with a similar loading condition (PPU, R=0.7, 1-hr hold time): (a) no stair-step growth at ~20 MPa m$^{1/2}$ and (b) stair-step growth at ~23 MPa m$^{1/2}$.

Furthermore, the K dependence of the CGR was found to differ with and without PPU. Figure 42 shows the measured CGRs with PPU and 2-hr hold time in this study. Each dataset was fitted to a power law correlation, and the obtained exponents are shown in the figure. Compared with Fig. 38, not only are the CGRs with PPU much higher than those measured under static K, but also the CGRs with PPU seem more sensitive to the changes of stress intensity factor. The exponents of CGRs with PPU are between 3.7 and 6.4, significantly higher than those of most of the exponents under constant load without PPU (i.e., 2.0-2.7). The only anomaly is the test on the ~5-dpa CW 316-Ti SS, where the exponents with and without PPU are quite similar, i.e., 4.6 for the CGRs without PPU and 5.1 for the CGRs with PPU. A careful analysis of the test periods without PPU giving rise to the high exponent revealed a possible slowly rising K condition. It appears that the K dependence is also related to the dynamic straining conditions, which are present with PPU or with any load transients. The possible linkage between the K dependence and dynamic loading suggests that irradiation-induced plastic instability must be critical for the cracking behavior of SSs. It is clear that dynamic loading

conditions have a significant effect on the cracking susceptibility of SSs in the low-corrosion-potential environments. This result implies that any load transient imposed by reactor shutdown/startup cycles and power fluctuations could be important factors for the cracking of reactor internal components.
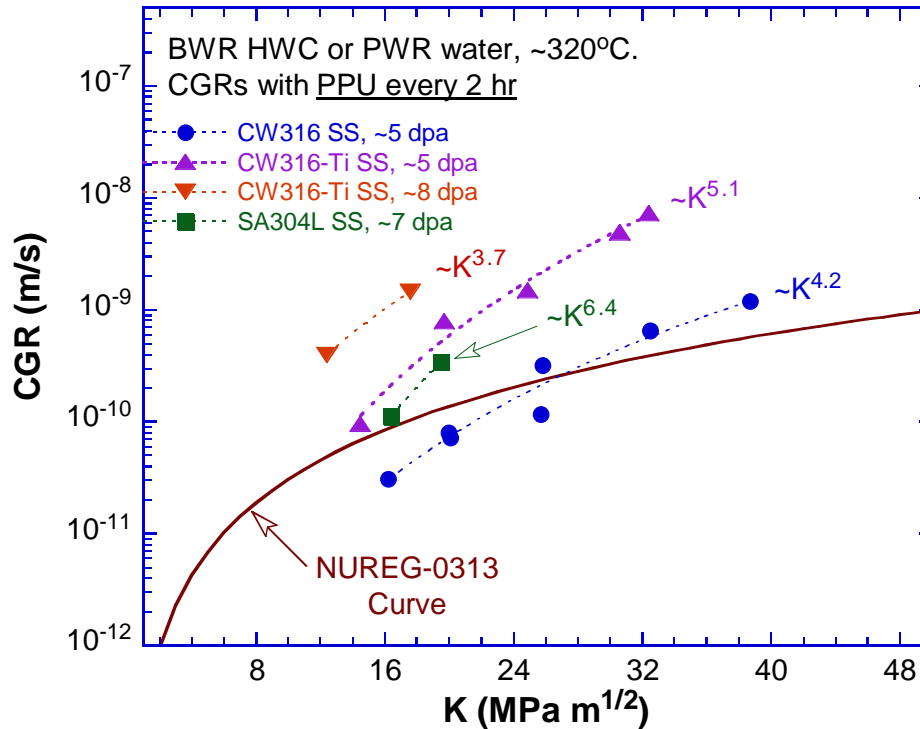

Figure 42. Constant-load CGRs with PPU and 2-hr hold time at ~320°C.

4.2.2 Effect of titanium

The effect of Ti addition was investigated with the CW 316 SS and CW 316-Ti SS at ~ 5 dpa in low-DO high-purity water. As shown in Figs. 35 and 36, the cyclic CGRs of CW 316 and CW 316-Ti SSs are similar. The environmental effect was not particularly strong at this dose in the low-corrosion-potential environment. However, when the tests were transitioned to the SCC CGR tests, a significant difference was observed between the CW 316 and CW 316-Ti SSs. The measured CGRs of the Ti-stabilized CW 316 SS were at least one order of magnitude higher than those of the CW 316 SS (see Figs. 38 and 42). This difference in SCC CGR was consistently observed in all test periods with and without PPU, and was more evident in the regime of high stress intensity factor. The higher cracking susceptibility of the CW 316-Ti SS can also be seen from their fracture surfaces. While the IG cracking was the sole fracture morphology during the SCC CGR test of the CW 316-Ti specimen (Fig. 16), some areas of mixed mode fracture of IG with isolated ductile features were observed along with IG cracking in the CW 316 SS (Fig. 8). Obviously, IG cracking was more difficult to develop in the CW 316 SS than in the CW 316-Ti SS. This result suggests a detrimental effect of Ti in cracking susceptibility of the cold-worked SSs in the low-corrosion-potential environment.

4.2.3 Effect of dose

The CW 316-Ti SS was tested at two doses. Both cyclic CGR and constant-load CGR increased with dose between ~5 and 8 dpa. As shown in Fig. 36, the fitting coefficient of the CW 316-Ti SS was more than a factor of two higher at ~8 dpa than at ~5 dpa. The constant-load CGR (without PPU) also increased substantially, from ~5 to 8 dpa in the low stress regime (below 25-30 MPa m$^{1/2}$), as shown in Fig. 38. The effect of dose became less evident above 30 MPa m$^{1/2}$. The different responses to irradiation dose at low and high stress regimes were caused by the different K dependence exhibited by the two tests.

The effect of dose was evaluated further by combining the current results with the previous data reported by Jenssen et al.[17, 29] The same heats (i.e., BR, CR, and SW) were used in both studies, but the previous tests were performed in both BWR and PWR water and at higher doses. Only the data in the low-corrosion-potential environments and in constant-K or near-constant-K test periods were included in the analysis. Each dataset was fitted to a power law correlation, and the obtained fitting curves are shown in Fig. 43. (Note that data points of the current tests were included in the figure.) An increasing trend of CGR can be seen with dose for all heats with a few exceptions. For the CW 316 SS (heat BR, Fig. 43a), the 11.3-dpa specimen showed unusually high CGRs at both 288 and 320°C. A few data points with "retarded" crack growth, however, were in the scatter band of the 7.8- and 25-dpa tests. No elevated CGR was observed in the ~5-dpa test. For the CW 316-Ti SS (heat CR, Fig. 43b), the fitting curve of 25-dpa data was much higher than that of the ~5- and 8-dpa tests, showing a continuous increase with dose between ~5 and 25 dpa. For the SA 304L SS (heat SW, Fig. 43c), only two fitting curves were available for comparison. The test on the 7.7-dpa sample yielded only one data point at the relevant environment and temperature, and its value was close to that of the 11.2-dpa specimen.

Figure 44 shows the dose dependence of SCC CGR obtained under constant-K or constant-load conditions. To single out the effect of dose, the data were compared at 20 MPa m$^{1/2}$ and 320°C. The normalized CGR was obtained with its own power correlation for each dataset. An increasing trend of CGR with dose can be seen for all heats. It seems the cracking susceptibility is not saturated up to 25 dpa in low-corrosion-potential environments.
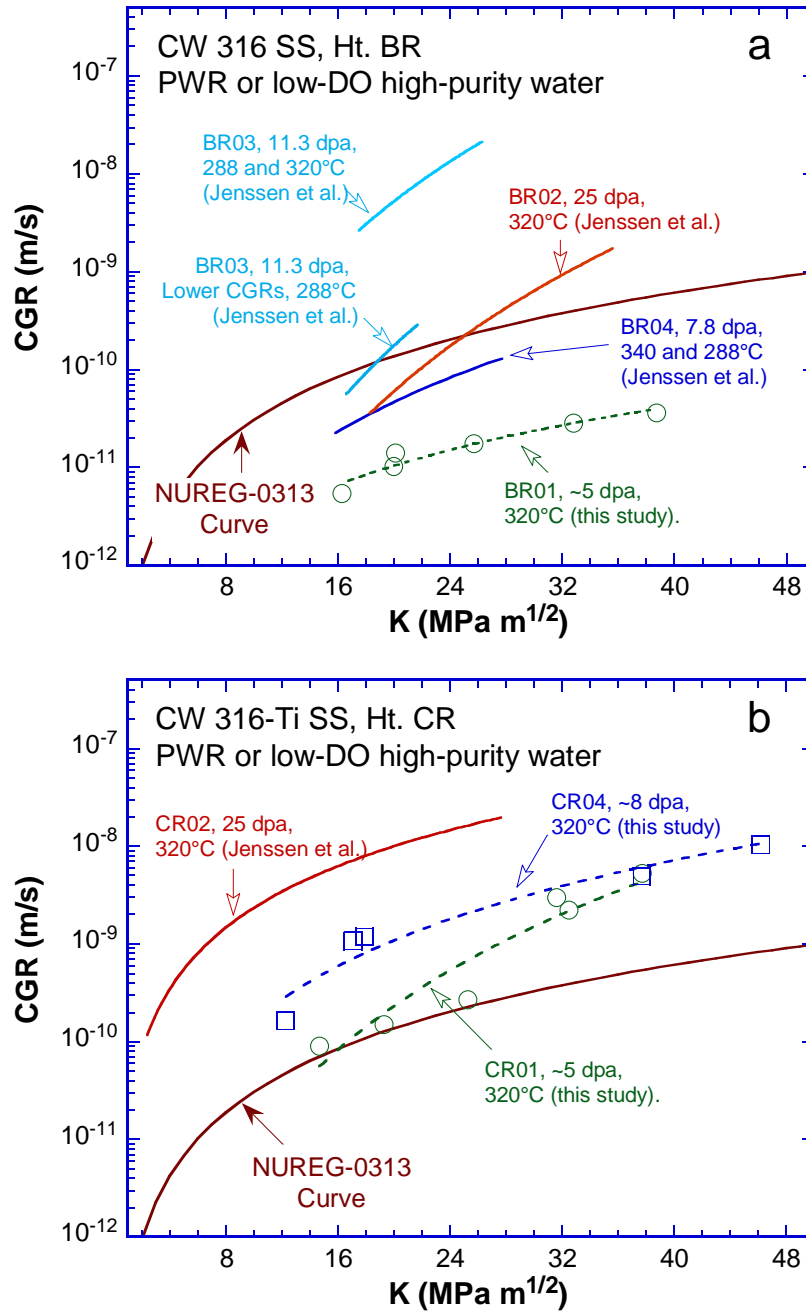
Figure 43. Crack growth rates at constant load or constant stress intensity factor for (a) CW 316
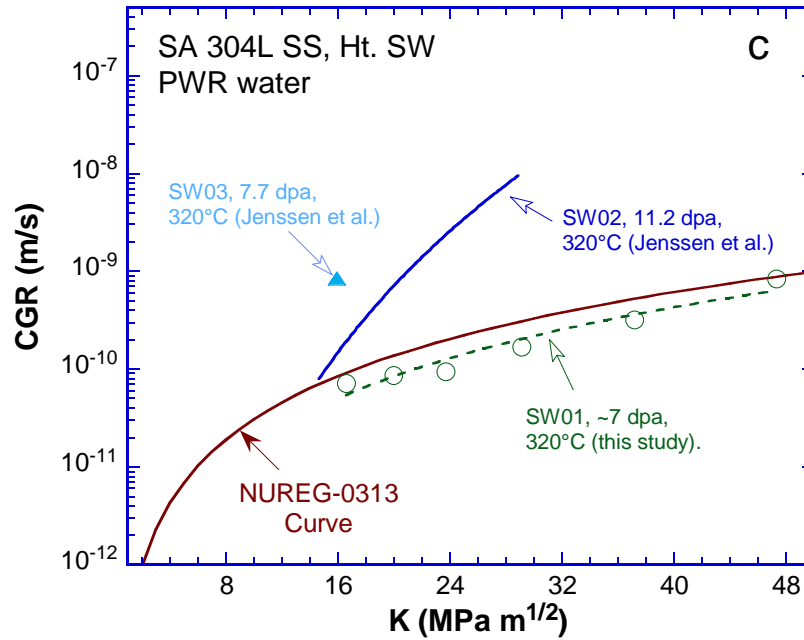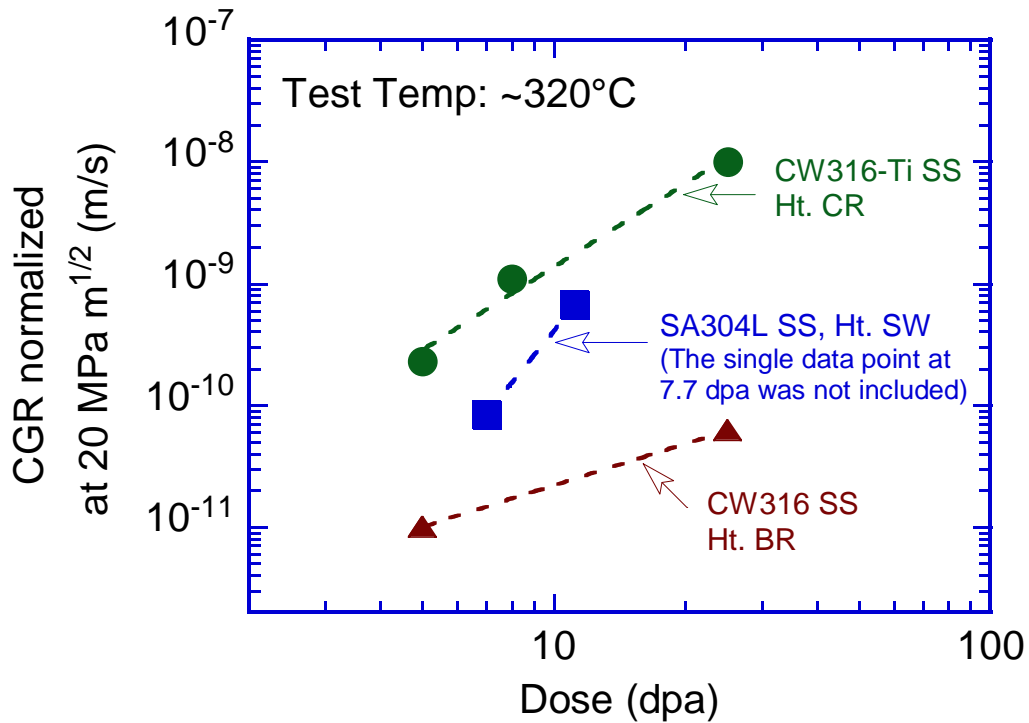SS, (b) CW 316-Ti SS, and (c) SA 304L SS.

Figure 43. (Cont'd)

Figure 44. Dose dependence of SCC CGR under constant load or constant stress intensity factor.

4.2.4 Effect of temperature

The effect of temperature on SCC CGR was evaluated in three specimens: CW 316 SS at ~5 dpa, CW 316-Ti SS at ~8 dpa, and SA 304L SS at ~7 dpa. Figure 45 shows all temperature dependences obtained in this study. Only constant-load CGRs without PPU are included in the figure. The two CW 316 SSs (with and without Ti) exhibited similar behavior, and CGR increased monotonically with temperature between ~270 and 320°C. The apparent activation energy is somewhat lower in the Ti-stabilized CW 316 SS. The CGR of SA 304L SS peaks around 290°C, then sharply declines between 290 and 320°C. Below 290°C, the Arrhenius slope of the SA 304L is also much shallower, resulting in an activation energy of 62 kJ/mol. The peak temperature for this sample suggests that more than one underlying process with opposite temperature dependences may operate during crack growth. The peak CGR is a result of the changes of these competing mechanisms with temperature.
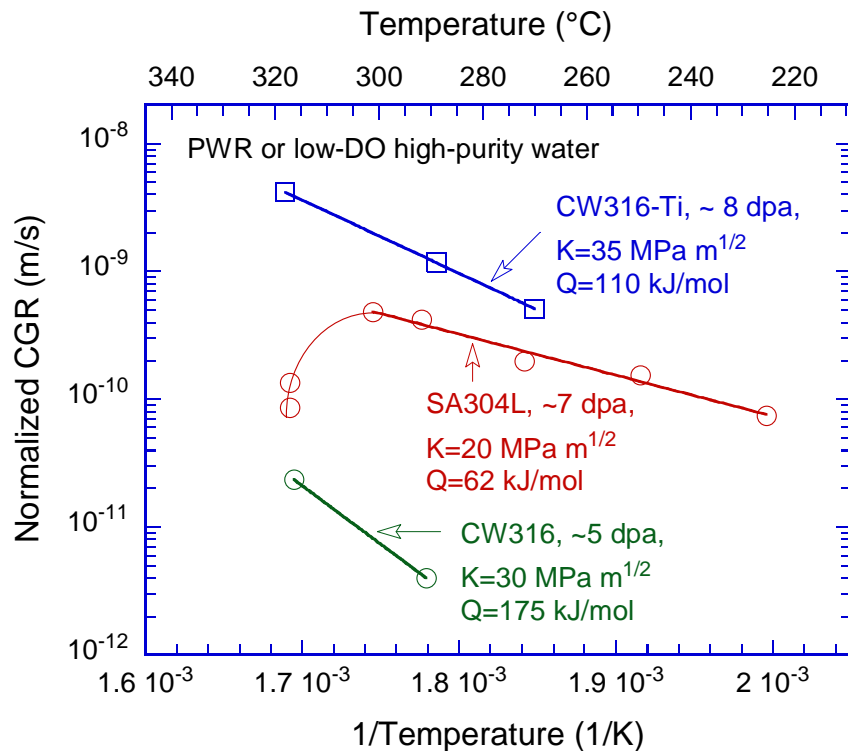

Figure 45. Temperature dependence of CGRs for three specimens.

4.3 Irradiation Embrittlement

Fracture toughness J-R tests were performed on the samples in the test environments after the CGR tests. All specimens underwent significant irradiation embrittlement at these doses (~5-8 dpa). Figure 46 shows the estimated fracture toughness values obtained in this study along with the unirradiated fracture toughness values of 304 and 316 SSs reported by Mills [30,31] and some previous results from Halden-I and -II irradiated specimens. [15, 26] Despite a difference in test temperature, a decreasing trend can be seen with increasing dose for this group of data. Among

the samples tested in the current study, SA 304L shows the best fracture resistance, and the measured J at 0.2-mm offset line was about 95 kJ/m^2. This toughness is much lower than the typical values for unirradiated SSs. The J values measured on the CW 316-Ti SS are nearly identical at ~5 and ~8 dpa (approximately 25 kJ/ m2), suggesting a saturation behavior of irradiation embrittlement for this heat. Additional results on the same material at higher doses would be helpful to confirm this observation. Despite good IASCC resistance, brittle fracture occurred in the J-R curve test of the CW 316 SS. This condition gave rise to the lowest toughness among all three materials tested, and the estimated K was about 46 MPa m$^{1/2}$. This value is fairly close to a lower bound of toughness for SSs observed previously. Additional work is needed to further explore the high dose regime for the embrittlement of SSs under neutron irradiation.
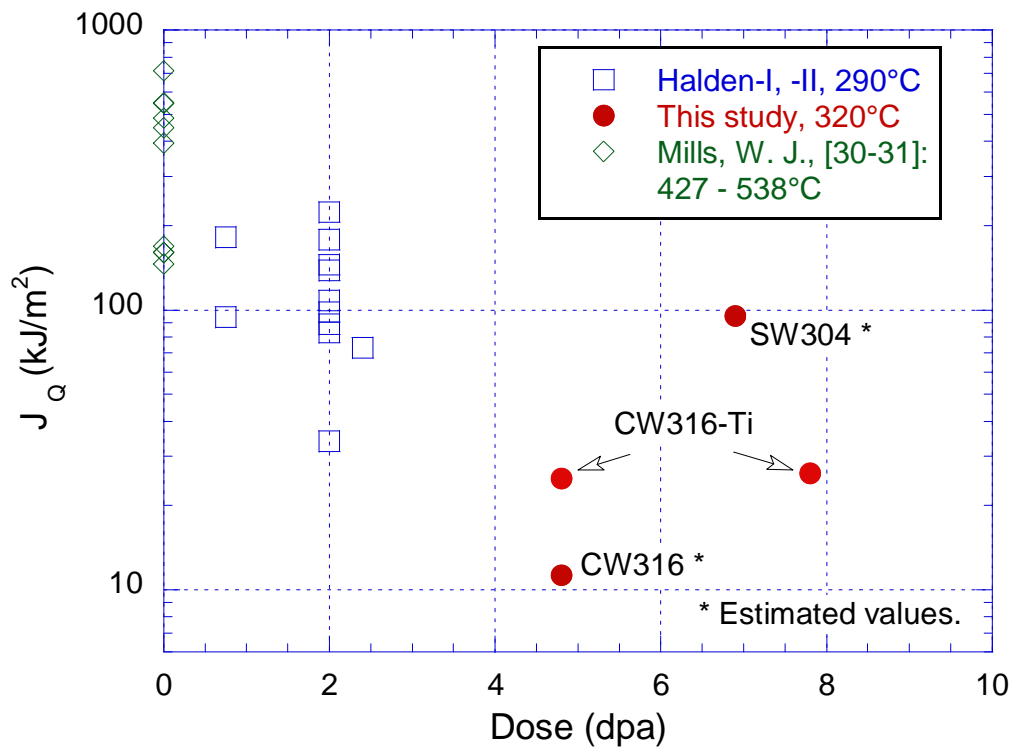

Figure 46. Fracture toughness J$_{0.2}$ values of SSs obtained in current and previous studies.

This page is intentionally left blank.

5   SUMMARY

Four DCT samples irradiated in the BOR-60 reactor were tested in either low-DO high-purity or PWR water. The specimens were CW 316 and SA 304L SSs commonly used in PWR core internals. Cyclic and constant-load CGR tests with and without PPU were performed on these samples to evaluate their IASCC susceptibility under PWR-relevant conditions. The temperature dependence of the CGR response was also evaluated in the tests. After the CGR tests, fracture toughness J-R curve tests were carried out at 320°C in the test environments. All fracture surfaces of the tested samples were examined with SEM, from which fracture morphologies were identified. The final crack extensions measured by DCPD were also corrected with the SEM measurements.

Environmentally enhanced cracking was readily induced in these irradiated specimens. A significant effect of irradiation dose on the corrosion fatigue response can be seen between ~5 and ~8 dpa. While TG cracking was the dominant fracture mode in the cyclic CGR test regions, small areas of IG facets could also be seen in the SA 304L SS. In the SCC CGR tests, PPU had a significant effect on the measured CGRs for all irradiated specimens. The CGRs with PPU can be more than one order of magnitude higher than those without PPU. Also, "stair-step" crack growth was often observed with load transients, and the K dependence of CGR was much higher with than without PPU. Irradiation-induced plastic instability seems to play a significant role in the IASCC behavior of SSs in low-corrosion-potential environments.

Intergranular cracking was the dominant fracture morphology for the constant-load CGR tests. The two CW 316-Ti SS specimens were the most susceptible heat in this study, and the CW 316 SS showed good resistance to IASCC. A detrimental effect of Ti could be seen at ~5 dpa. An increasing trend of CGR with dose could also be seen among these samples up to 25 dpa. The temperature dependence of CGR showed a peak around 290°C for the SA 304L SS, suggesting more than one cracking mechanism with opposite temperature dependences operating to propagate the crack.

A decreasing trend of fracture toughness could be seen with increasing dose. Between ~5 and 8 dpa, the J values of the two CW 316-Ti SS specimens were nearly identical, suggesting a saturation behavior of this material. Additional tests at higher doses are needed to confirm this observation.

This page is intentionally left blank.

References

1. U.S. NRC, "Expert Panel Report on Proactive Materials Degradation Assessment," NUREG/CR-6923, 2006.

2. U.S. NRC, "Generic Aging Lessons Learned (GALL) Report," NUREG-1801, Rev. 2, 2010.

3. Cheng, C. F., "Intergranular Stress-Assisted Corrosion Cracking of Austenitic Alloys in Water-Cooled Nuclear Reactors," J. Nucl. Mater., **56** (1975): 11–33.

4. Garzarolli, F., H. Rubel, and E. Steinberg, "Behavior of Water Reactor Core Materials with Respect to Corrosion Attack," Proc. Intl. Symp. on Environmental Degradation of Materials in Nuclear Power Systems - Water Reactors, NACE, Houston, TX, pp. 1–24, 1984.

5. Garzarolli, F., D. Alter, and P. Dewes, "Deformability of Austenitic Stainless Steels and Nickel-Base Alloys in the Core of a Boiling and a Pressurized Water Reactor," Proc. Intl. Symp. on Environmental Degradation of Materials in Nuclear Power Systems - Water Reactors, American Nuclear Society, La Grange Park, IL, pp. 131–138, 1986.

6. Berge, Ph., and F. de Keroulas, "The Present Situation Regarding Environmental Degradation of Components in Pressurized Water Reactors," Proc. 4th Int. Symp. on Environmental Degradation of Materials in Nuclear Power Systems - Water Reactors, NACE, Houston, TX, pp. 1-11, 1990.

7. Andresen, P. L., F. P. Ford, S. M. Murphy, and J. M. Perks, "State of Knowledge of Radiation Effects on Environmental Cracking in Light Water Reactor Core Materials," Proc. 4th Intl. Symp. on Environmental Degradation of Materials in Nuclear Power Systems - Water Reactors, NACE, Houston, TX, pp. 1.83-1.121, 1990.

8. Nelson, J., and P. Andresen, "Review of Current Research and Understanding of Irradiation-Assisted Stress Corrosion Cracking," Proc. 5th Int. Symp. Environmental Degradation of Nuclear Power Systems, ANS-NACE-AIME, 1992.

9. Scott, P., "A Review of Irradiation Assisted Stress Corrosion Cracking," J. Nucl. Mater., **211** (1994): 101-122.

10. Bruemmer, S. M., and G. S. Was, "Microstructural and Microchemical Mechanisms Controlling Intergranular Stress Corrosion Cracking in Light-Water-Reactor Systems," J. Nucl. Mater., **216** (1994): 348-363.

11. Was, G. S., and P. L. Andresen, "Stress Corrosion Cracking Behavior of Alloys in Aggressive Nuclear Reactor Core Environments," Corrosion, **63**(1), (2007): 19.

12. Was, G. S., *Fundamentals of Radiation Materials Science – Metals and Alloys*, Springer, Berlin Heidelberg New York, 2007.

13. Hettlarachchi, S., "BWR SCC Mitigation Strategies and Their Effectiveness," Proc. 11th Intl. Symp. on Environmental Degradation of Materials in Nuclear Power Systems, NACE, Stevenson, WA, 2003.

14. Castano, M. L., M. Nacas, D. Gomez-Briceno, T. Onchi, and K. Hide, "IASCC Response of Sensitized 304 Stainless Steels to the Hydrogen Injection in BWR," Proc. 10th Intl. Symp. on Environmental Degradation of Materials in Nuclear Power Systems - Water Reactors, NACE, Lake Tahoe, NV, 2001.

15. Chopra, O. K., and W. J. Shack, "Crack Growth Rates and Fracture Toughness of Irradiated Austenitic Stainless Steels in BWR Environments," NUREG/CR-6960, ANL-06/58, 2008.

16. Chen, Y., W. J. Shack, B. Alexandreanu, E. E. Gruber, and A. S. Rao, "Cracking Behavior of Irradiated Heat-Affected Zone Specimens of Type 304 and 304L Stainless Steel Welds in High-Purity Water," Proc. 14th Int. Conf. on Environmental Degradation of Materials in Nuclear Power Systems, Virginia Beach, VA, August 23-27, 2009.

17. Jenssen, A., J. Stjärnsäter, and R. Pathania, "Crack Growth Rate Testing of Fast Reactor Irradiated Type 304L and 316 SS in BWR and PWR Environments," Proc. 14th Int. Conf. on Environmental Degradation of Materials in Nuclear Power Systems, Virginia Beach, VA, August 23-27, 2009.

18. Jenssen, A., P. Efsing, K. Gott, P. O. Andersson, "Crack Growth Behavior of Irradiated Type 304L Stainless Steel in Simulated BWR Environment," Proc. 11th Intl. Symp. on Environmental Degradation of Materials in Nuclear Power Systems--Water Reactors, NACE, (2003)

19. Chopra, O. K., B. Alexandreanu, E. E. Gruber, W. J. Shack, "Crack Growth Behavior of Irradiated Austenitic Stainless Steel Weld Heat Affected Zone Material in High-Purity Water at 289°C," Proc. 12th Int. Symp. on Environmental Degradation of Materials in Nuclear Power Systems--Water Reactors, TMS, p.289 (2005).

20. Karlsen, T. M., P. Bennett, N.W. Hoegberg, "In-Core Crack Growth Rate Studies on Irradiated Austenitic Stainless Steels in BWR and PWR Conditions in the Halden Reactor," Proc. 12th Intl. Conf. on Environmental Degradation of Materials in Nuclear Power System – Water Reactors, 2005.

21. Electric Power Research Institute, "CIR II Program: Description of the Boris 6 and 7 Experiments in the BOR-60 Fast Breeder Reactor," Report No. 1011787, Palo Alto, CA, 2005.

22. ASTM International, "Standard Test Method for Measurement of Fracture Toughness," E1802-08a, Annual Book of ASTM Standards, 2008.

23. Mills, W. J., "Fracture Toughness of Type 304 and 316 Stainless Steels and Their Welds," Int. Mater. Rev., **4**(2), (1997): 45.

24. Chen, Y., O. K. Chopra, W. K. Soppet, W. J. Shack, Y. Yang, and T. Allen, "Cracking Behavior and Microstructure of Austenitic Stainless Steels and Alloy 690 Irradiated in BOR-60 Reactor, Phase I," ANL/09-32, 2007.

25. Chen, Y., W. Soppet, B. Alexandreanu, and K. Natesan, "Technical Letter Report on Slow Strain Rate Tensile Tests of Irradiated Stainless Steels in PWR Environment," ANL-12/33, 2012.

26. Chen, Y., O. K. Chopra, E. E. Gruber, and W. J. Shack, "Irradiation-Assisted Stress Corrosion Cracking of Austenitic Stainless Steels in BWR Environments," NUREG/CR-7018, ANL-09/17, 2010.

27. Shack, W. J., and T. F. Kassner, "Review of Environmental Effects on Fatigue Crack Growth of Austenitic Stainless Steels," NUREG/CR-6176, 1994.

28. Hazelton, W. S., and W. H. Koo, "Technical Report on Material Selection and Processing Guidelines for BWR Coolant Pressure Boundary Piping, Final Report," NUREG-0313, Rev. 2, 1988.

29. Jenssen, A., J. Stjärnsäter, and R. Pathania, "Crack Growth Rates of Irradiated Commercial Stainless Steels in BWR and PWR Environments," 15th Int. Conf. on Environmental Degradation of Materials in Nuclear Power Systems, eds., J. T. Busby, G. Ilevbare, and P. L. Andresen, TEM, 2011.

30. Mills, W. J., "Fracture Toughness of Aged Stainless Steel Primary Piping and Roactor Vessel Materials," Journal of Pressure Vessel Technology, Transactions of the ASME, **109** (1987): 440.

31. Mills, W. J., "Fracture toughness of Irradiated Stainless Steel Alloys," Westinghouse Harford Company, HEDL-SA-3471, Hanford Engineering Laboratory Report, Richland, WA, 1986.

Nuclear Engineering Division
Argonne National Laboratory
9700 South Case Avenue
Argonne, IL 60439

www.anl.gov